Characterizing Metal/Oxygen Batteries with Multiphase Continuum-Scale Models

by

Jing Liu

A dissertation submitted in partial fulfillment
of the requirements for the degree of
Doctor of Philosophy
(Chemical Engineering)
in The University of Michigan
2015

Doctoral Committee:

Assistant Professor Charles W. Monroe, Chair
Professor Ronald G. Larson
Professor Phillip E. Savage
Assistant Professor Donald J. Siegel

ACKNOWLEDGEMENTS

First, I would like to gratefully and sincerely thank Professor Charles Monroe. He is always available and willing to discuss and work out problems with me, whenever I have the need. He is very knowledgeable in electrochemistry and mathematical analysis. Without his guidance and help, I could have spent a lot of time on the wrong research paths and achieved much less in these five years. His work ethic and research attitude also sets him a good example for me to follow.

I must also thank my family, especially my mother Shuyuan and my husband Yu. My mother was my first teacher, teaching me basic English and natural science. More importantly, I learned persistence from her, which has been and will continue influencing my life. She was also the first to encourage me to pursue an advanced degree. This dissertation may not exist without her initial encouragement. I and Yu, both Ph.D students at University of Michigan, have been supporting each other throughout these year at the university. Mutual understanding and care makes our 'Ph.D lives' fully of confort and joy.

Finally, I would like to express my gratitude to the Monroe research group, especially the following people: Sun Ung Kim taught me coding with Fortran; Lucas Griffith has been on the same project as me, and we discuss problems all the time; James Saraidaridis and Priyamvada Goyal have done a lot of proof readings for me.

TABLE OF CONTENTS

LIST OF FIGURES

Figure

LIST OF TABLES

Table

LIST OF APPENDICES

Appendix

ABSTRACT

Characterizing Metal/Oxygen Batteries with Multiphase Continuum-Scale Models

by

Jing Liu

Chair: Charles W. Monroe

This dissertation focuses on the development of theory and continuum-scale models to characterize transport and kinetics in metal/oxygen batteries.

Newman's concentrated-solution theory is extended to elucidate two transport mechanisms associated with the volumes dissolved electrolytes occupy: the 'excluded-volume effect', which arises when concentration polarization induces solution-density gradients that drive volume redistribution; and 'Faradaic convection', which occurs when interfacial electrochemical reactions induce bulk flow. The excluded-volume effect can be accounted for in concentrated-solution theory by incorporating a thermodynamic state equation that describes the solution's local molar volume. Faradaic convection is introduced through boundary conditions that include volume-average velocity, which is distributed throughout a solution by a volume-balance governing equation. Two dimensionless parameters quantify the importances of these phenomena, which prove relevant when modeling nonaqueous electrolytes. Analytical formulas are derived to describe concentration polarization and diffusion potentials in parallel-electrode cells undergoing symmetric ion-deposition/stripping half-reactions.

In moderately concentrated nonaqueous electrolytes, both solute-volume effects are found to be significant: Faradaic convection elevates limiting currents by as much as 10% above those predicted by a theory neglecting it; the excluded-volume effect similarly impacts diffusion potentials.

Accurately measured material properties are of great significance in the modeling of battery systems. An analysis of binary electrolytic solutions in planar electrochemical cells that support symmetric electrode reactions is performed to serve as a foundation for experimental measurements of diffusivities and transference numbers. Prior theory is extended to include a nonlinear relationship between concentration polarization and cell voltage, as well as accounting for solute-volume effects. The extended theory provides significant corrections when concentration polarization is very large or when electrolytes are very concentrated, rationalizing unexpected voltage responses that have been observed during prior transport-property measurements. Several graphs are presented to guide design of galvanostatic-polarization experiments, and complete sets of properties are provided for two non-aqueous lithium battery electrolytes: $LiPF_6$ in propylene carbonate and $LiPF_6$ in a carbonate mixture.

The modified concentrated-solution theory is next incorporated into a porous-electrode theory, which is used to model the positive electrodes in metal/oxygen batteries. Continuum simulations of a discharging lithium/oxygen cell are implemented and compared with experimental data to examine how cell capacity is controlled by macroscopic mass transfer, interfacial kinetics, and electronic conduction through the Li_2O_2 discharge product. The model accounts for the three-phase nature of the positive electrode, including an explicit discharge-product layer whose volume distribution depends on the local depth of discharge. Three hypothetical deposition mechanisms involving different product morphologies and electron-transfer sites are studied. To match experimental discharge-voltage *vs.* capacity and capacity *vs.* discharge-current data qualitatively, the discharge-product layer must be assumed to have electronic

resistivity lower than 10^8 Ω cm – several orders of magnitude lower than typical insulators. This supports the notion that the presence of Li_2O_2, whose bulk resistivity is measured/calculated to be above 10^{10} Ω cm, does not wholly prevent electrons from reaching dissolved reactants. The discharge product also appears to allow electron transport over length scales longer than tunneling permits. 'Sudden death' of voltage in Li/O_2 cells is explained by macroscopic oxygen-diffusion limitations in the positive electrode, which are exacerbated by pore clogging as the discharge product forms.

Finally, the multicomponent, multiphase continuum model is applied to simulate the first discharge/charge cycle of a sodium/oxygen battery. Simulated discharge/recharge curves are compared with experiments. Unlike the lithium/oxygen cell, the sodium/oxygen system exhibits low total overpotential for both discharge and charge. The discharge and charge overvoltages are comparable, suggesting that the positive-electrode reaction mechanism may follow a reversible pathway. An overpotential-breakdown analysis indicates that positive-electrode kinetics accounts for about 90% of the potential loss during both discharge and charge. The 'sudden death' of voltage at end-of-discharge owes to transport limitations in the porous positive electrode; the voltage spike at end-of-charge owes to the limited availability of discharge product.

CHAPTER I

Introduction

Transportation accounts for about 28% of total US energy usage. Over 90% of this transportation energy comes from petroleum, a non-renewable energy source. According to US Energy Information Administration, the transportation technologies operate at 21% energy efficiency, resulting in a large amount of wasted fuel energy [1]. Increasing transportation energy efficiency and decreasing the dependence on petroleum to power vehicles are two promising ways of reducing the waste, both of which require the exploration of novel energy resources and innovative energy storage and conversion systems.

Some renewable energy sources, such as solar energy, are intermittent in time and variable in space, while others, like geothermal energy, are highly dependent on location [1]. Additionally, energy carriers need to be conveniently delivered to consumers, so that they can be used to power vehicles. Chemicals are a convenient way to store energy, and electrochemical batteries are one strategy to harness chemical energy to power vehicles.

A number of different types of batteries have served as the energy storage systems in electric vehicles (EVs). Lead-acid batteries were adopted to power some of the earliest and pioneering EVs such as the first generations of Toyota RAV4 EV and General Motors EV1. Nickel-metal hydride batteries are successful in powering vari-

ous EVs nowadays, like Ford Ranger EV, Chevrolet Malibu Hybrid, *etc.* Lithium-ion batteries (LIB), with relatively high power-to-weight ratio and energy efficiency, are most commonly used in today's EVs, one example of which is the Tesla Roadster.

Despite the merits of these battery, their performance lacks in some regards when compared to the internal combustion engine (ICE), as shown by the Ragone plot in Figure 1.1 [2]. The specific energy of ICE is far higher than all the electrochemical energy storage systems on the plot (*i.e.*, a given amount of gasoline can power a vehicle to run farther than the same amount of battery active species.) The chemistry of alkali-metal/oxygen (M/O_2) batteries, however, delivers batteries with theoretical specific energy comparable or even higher than ICE. For example, the theoretical specific energy of a lithium/oxygen (Li/O_2) battery is about 3500 Wh/kg of lithium peroxide (Li_2O_2, the main discharge product), and that of a sodium/oxygen (Na/O_2) battery is about 1100 Wh/kg of sodium superoxide (NaO_2, the main discharge product) [3–5]. The high theoretical specific energies of M/O_2 batteries suggest that they are quite promising in matching and surpassing the performance of ICE for powering vehicles.

Before the commercialization and the massive usage of M/O_2 batteries in EVs, we need to have a good understanding and a feasible design. Numerous research efforts have pursued high practical energy capacity, high power efficiency, and understanding of the positive-electrode kinetics, *etc.*[6]. This dissertation is dedicated to applying multiphase continuum-scale models to simulate transport and kinetics in M/O_2 batteries. In Chapter II, the concentrated-solution theory is improved to simulate transport in the electrolyte phase, which occupies the battery separator and pores in the positive electrode. The model accounts for solute-volume effects, which are intrinsic in all electrochemical transport processes, and are of great importance in (even moderately) concentrated non-aqueous electrolytic solutions. In Chapter III, the modified concentrated-solution theory is applied in the measurements of elec-

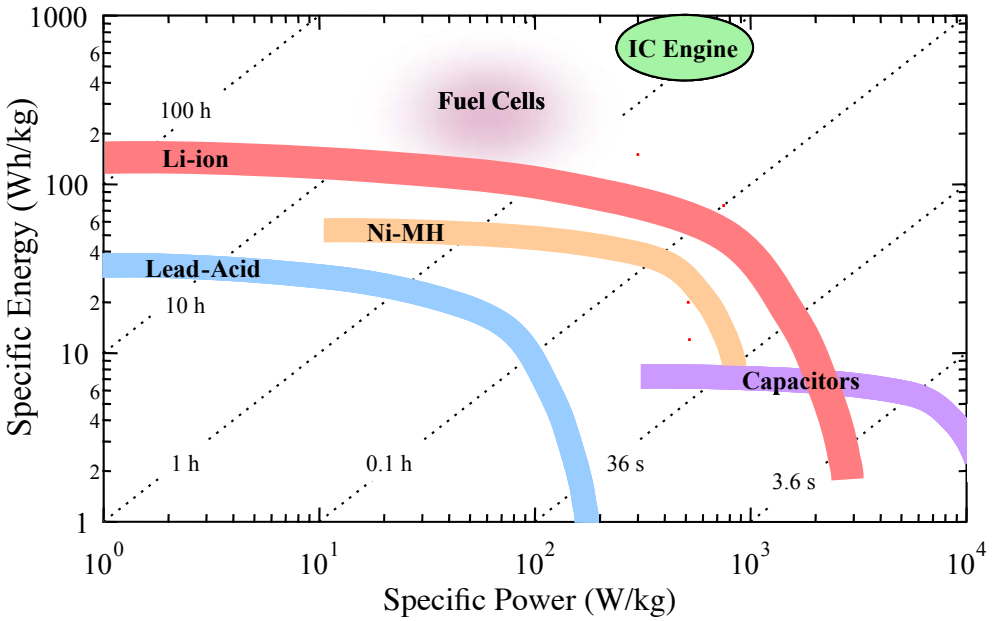

Figure 1.1: Ragone plot showing the specific energy and the specific power of various energy storage and conversion systems. The dashed lines indicate the discharge times.

trolyte properties, which are essential inputs in transport models. In Chapter IV, the modified concentrated-solution model is incorporated into the porous-electrode theory to model the first discharge process of a Li/O_2 battery. Positive-electrode kinetics and capacity-limiting factors of the battery system are studied. In Chapter V, the recharge process and kinetics of a Na/O_2 battery are studied with the same model developed in Chapter IV.

CHAPTER II

Transport in Electrolyte

2.1 Introduction

Concentrated-solution theory is widely applied when simulating dynamic electrochemical systems, and is useful for rationalizing or predicting how material properties determine microscopic distributions of concentration and potential, as well as macroscopic current/voltage relationships [7–20]. Models based on this theory are also employed to characterize battery electrolytes [21–27].

Newman and colleagues [28–32] were among the first to apply the Onsager-Stefan-Maxwell formalism [33, 34] to electrolyte transport. Extended Stefan-Maxwell constitutive laws are force-explicit, and therefore harder to incorporate into material balances than typical flux-explicit laws. Within the concentrated-solution theory, the independent Stefan-Maxwell equations are inverted—a process that involves the selection of a convective velocity [28–30].

If one chooses the solvent velocity, $\vec{v}_0$, as the reference for convection, the material balance for a binary electrolyte (comprising one anion and one cation) in a locally electroneutral binary solution (comprising one electrolyte and one neutral solvent) becomes [31, 32]

$$\frac{\partial c}{\partial t} + \vec{\nabla} \cdot (c\vec{v}_0) = \vec{\nabla} \cdot \left\{ D \left[1 - \left(\frac{d \ln c_0}{d \ln c} \right)_{T,p} \right] \vec{\nabla} c \right\} - \frac{\vec{i} \cdot \vec{\nabla} t_+^0}{z_+ \nu_+ F}, \tag{2.1}$$

where c is the molar electrolyte concentration, $\vec{i}$ is the current density, and F is Faraday's constant; z_+ and ν_+ respectively represent the cation's equivalent charge and its stoichiometry in an electrolyte formula unit. Two transport properties appear: t_+^0, the cation transference number relative to the solvent velocity, and D, the Fickian diffusivity. A thermodynamic derivative of the solvent concentration c_0 serves to convert the molarity-gradient driving force in equation 2.1 into the molal-concentration-gradient force classically used to define (and measure) D [31, 32].

Almost all contemporary lithium-ion battery models that include liquid-phase transport use balances referred to the solvent velocity [35–47]. Since heterogeneous reactions involving solvent are (ideally) minimal, $\vec{v}_0$ can be taken to vanish uniformly. This makes equation 2.1 simpler from the viewpoint of convection, but requires consideration of the excluded-volume factor $[1 - (d\ln c_0/d\ln c)_{T,p}]$.

In their development of the popular 'Dualfoil' model, Doyle *et al.* assumed explicitly that $(d\ln c_0/d\ln c)_{T,p} \approx 0$, stating that the solvent concentration depended weakly on the electrolyte concentration in the system they considered [35, 36]. Modeling groups that followed this initial work have almost uniformly applied the same approximation without considering its validity in different circumstances [41–60]. Concentration gradients could cause significant local variation in the excluded-volume factor, leading to an apparent driving force for bulk diffusion—a phenomenon we call the 'excluded-volume effect'.[1]

Electrolyte volume can impact concentrated-solution transport by another mechanism, which we call 'Faradaic convection'. This occurs when bulk flow is induced by interfacial reactions that consume or produce constituents of the solution phase. When analyzing interfacial instability during electrodeposition, Sundstrøm and Bark [61] described Faradaic convection in a liquid, probably making them the first to de-

[1]For a binary electrolytic solution, equations 2.4 and 2.6 combine to show that $[1 - (d\ln c_0/d\ln c)_{T,p}]$ equals $(c_0\overline{V}_0)^{-1}$—the inverse of the local solvent volume fraction. Thus the excluded-volume effect is likely significant if the electrolyte volume fraction is large.

scribe the effect formally. But ultimately the phenomenon was eliminated from their model by a dilute-solution approximation.

Nyman *et al.* have provided the most detailed accounting for both the excluded-volume effect and Faradaic convection in simulations, and have created models that improve the agreement between theoretical and experimental transference-number measurements [62–65]. Although that group has implemented sophisticated numerical analyses, the contributions that solute-volume effects make to their high-quality results have not been quantified.

This chapter illustrates how the excluded-volume effect and Faradaic convection can impact transport simulations. Rather than using equation 2.1, the analysis follows an alternative approach suggested by Newman and Chapman, who employed the volume-average velocity as the reference for convection [30]. This reference velocity simplifies the material balance by eliminating the excluded-volume factor, but it necessitates a local volume balance [62–67]. Models accounting for volume flow in multicomponent and binary electrolytic solutions are developed in section 2.2, which also addresses model closure.

The importance of solute-volume effects is measured in section 2.3 by dimensional analysis of governing equations based on the volume-average velocity and boundary conditions that account for reaction-induced volume flow. Two key dimensionless parameters quantify solute-volume effects in binary solutions; their values are provided for a number of electrolytes. Solute-volume effects prove to be particularly significant in non-aqueous electrolytes.

Under the assumptions that solution density varies linearly with electrolyte concentration, and that the Fickian diffusivity and transference number are relatively constant, analytical solutions of the transport equations are provided in section 2.4 to describe parallel-electrode cells undergoing symmetric deposition/stripping half reactions at both electrodes. Both the limiting current and the overpotential asso-

ciated with concentration polarization in these cells are noticeably affected by finite electrolyte volume.

2.2 Governing equations with solute volume

2.2.1 Excluded-volume effect: definition

In a phase comprising n constituents at constant absolute temperature T and pressure p, the Gibbs phase rule mandates that there are only $n-1$ independent composition variables. More concretely, in an n-ary phase described by the Gibbs free energy, the extensivity of volume V implies that it can be expressed in the functional form

$$V\left(T,p,\{n_k\}_n\right) = \sum_{k=1}^{n} \overline{V}_k n_k, \tag{2.2}$$

where n_k is the molar content of species k, and $\overline{V}_k = (\partial V/\partial n_k)_{T,p,n_{j\neq k}}$ the partial molar volume, which also depends on T, p, and composition. Division of both sides of equation 2.2 by V and the total molar concentration c_T, defined as

$$c_\mathrm{T} = \sum_{k=1}^{n} \frac{n_k}{V}, \tag{2.3}$$

yields a thermodynamic relation governing the total molar volume (inverse total concentration),

$$\frac{1}{c_\mathrm{T}} = \sum_{k=1}^{n} \overline{V}_k y_k. \tag{2.4}$$

This equation of state introduces the particle fraction of species k, y_k, which relates to the molar species concentration c_k through $c_k = y_k c_\mathrm{T}$. Particle fractions are a convenient composition basis because they are independent of T and p, and their sum always satisfies

$$\sum_{k=1}^{n} y_k = 1, \tag{2.5}$$

showing clearly that any one of the composition variables depends on the others. The key observation underpinning analysis of the excluded-volume effect is that equations 2.4 and 2.5 should hold true locally (pointwise throughout a phase), as well as globally (for the phase as a whole).

By using the isothermal, isobaric Gibbs-Duhem equation on $V(T, p, \{n_k\}_n)$, which can be expressed as

$$\sum_{k=1}^{n} y_k d\overline{V}_k = 0, \tag{2.6}$$

it can be shown that if all the species in a multicomponent solution have positive partial molar volumes—which, to the best of our knowledge, is true in all cases—then inducing a gradient in the molar concentration of one species will always induce an opposing gradient in the molar concentration of another, if all remaining species contents are fixed. For a given species, this observation defines formally the 'excluded-volume effect' within the solution as a whole.

2.2.2 Volume flow

Given c_{T} as an intensive variable that quantifies local solution volume, it remains to develop a variable that conveniently measures local volume flux. Within an n-ary phase at constant T and p, the increment of total volume dV carried through a surface element $d\vec{S}$ in an instant dt can be expressed in terms of the volumes species carry as

$$dV = \sum_{k=1}^{n} \overline{V}_k dn_k = \sum_{k=1}^{n} \overline{V}_k \vec{N}_k \cdot d\vec{S} dt = \vec{v}^{\square} \cdot d\vec{S} dt, \tag{2.7}$$

where $\vec{N}_k$ is the molar flux of species k relative to a stationary coordinate frame. This equation introduces the volume-average velocity $\vec{v}^{\square}$, defined as

$$\vec{v}^{\square} = \sum_{k=1}^{n} \overline{V}_k \vec{N}_k. \tag{2.8}$$

Through equation 2.7, it is seen that individual species fluxes can lead to bulk volume flow, which is quantified by the volume-average velocity field.

Although it is well known that convective mass transfer can be represented equally well by any reference velocity [68], such as the mass-average velocity [69], the mole-average velocity [70], the velocity of a particular species [32], *etc.*, the volume-average velocity $\vec{v}^{\square}$ is a particularly useful choice for multicomponent transport analysis [30]. To show why, consider the molar material balances, which can be written for each species k as

$$\frac{\partial(c_{\mathrm{T}} y_k)}{\partial t} = -\vec{\nabla} \cdot \vec{N}_k. \tag{2.9}$$

Multiply each of equations 2.9 by $\overline{V}_k$, then sum over all species, use the scalar product rule $d(AB) = AdB + BdA$ and the scalar/vector product rule $\vec{\nabla} \cdot (s\vec{v}) = s\vec{\nabla} \cdot \vec{v} + \vec{v} \cdot \vec{\nabla} s$, apply volume Gibbs-Duhem equation 2.6, insert the definition of volume-average velocity from equation 2.8, and simplify using equation of state 2.4 to show that

$$\vec{\nabla} \cdot \vec{v}^{\square} = \sum_{k=1}^{n} \vec{N}_k \cdot \vec{\nabla} \overline{V}_k. \tag{2.10}$$

This volume-continuity equation depends linearly on the n independent material balances 2.9, and can replace any one of them; it has the advantage that no accumulation term appears. Introduction of equation 2.8 and replacement of one of equations 2.9 with equation 2.10 eliminates an apparent coupling among the balances through time derivatives.

2.2.3 Charge flow

Multicomponent-electrolyte dynamics involves several electrical state variables. Some standard equations will be restated here because they are needed to assess model closure. The forms given also help to emphasize the use of y_k as a basis for composition and $\vec{N}_k$ as a basis for flux.

Faraday's law relates the local current density to the species fluxes,

$$\vec{i} = F \sum_{k=1}^{n} z_k \vec{N}_k, \tag{2.11}$$

in which z_k represents the equivalent charge of species k. Sufficiently far from interfaces [71, 72], and within volume elements whose characteristic sizes are much larger than the Debye length [73], local electroneutrality holds,

$$\sum_{k=1}^{n} z_k y_k \approx 0. \tag{2.12}$$

Although it is algebraic, equation 2.12 can be seen to arise from the differential form of Gauss's law: on the length scales of typical electrochemical cells, the electric-field gradients associated with ionic currents induce relatively small local excess charge densities, which, due to the large value of Faraday's constant and the small values of typical permittivities, suggest that local stoichiometric imbalances of ion concentrations are negligible [32].

Last a thermodynamic basis for the potential is needed. The electrochemical potential of species k, μ_k, can be defined generally as

$$\mu_k = \mu_k^{\ominus} + RT \ln\left(\lambda_k y_k\right) + z_k F \Phi, \tag{2.13}$$

where $\mu_k^{\ominus}$ is the electrochemical potential of k in a secondary reference state [74], λ_k its activity coefficient on a particle-fraction basis, and Φ an electrical potential. Electrochemical potentials must satisfy the isothermal, isobaric Gibbs-Duhem equation on internal energy,

$$\sum_{k=1}^{n} y_k d\mu_k = 0, \tag{2.14}$$

a constraint that must be used to ensure thermodynamic consistency of the activity coefficients. The particle-fraction basis is particularly convenient for expressing

activity in μ_k because equation 2.14 is satisfied by the case of an 'ideal electrolytic solution', in which $\lambda_k = 1$ for every species.

It is customary to replace one of the material fluxes with the electric current, which is more readily measured or controlled and can be viewed as a driving force for migration that does not require explicit consideration of the electrical potential [75]. Multiplying each of equations 2.9 by Fz_k, summing over all species, applying approximation 2.12, and substituting equation 2.11 yields

$$\vec{\nabla} \cdot \vec{i} = 0, \tag{2.15}$$

which expresses continuity of charge. Similarly to equation 2.10, this depends linearly on the material balances, and can replace any one of them whenever any constituent of a phase is charged and local electroneutrality maintains. Equation 2.15 eliminates a second apparent coupling among the material balances through time derivatives.

2.2.4 Multicomponent flux laws

Transport in concentrated electrolytic solutions can be described by Onsager-Stefan-Maxwell theory following Newman [31]. At constant T and p, the balance among the thermodynamic driving force associated with diffusion of species i, $-c_{\mathrm{T}} y_i \vec{\nabla} \mu_i$, and the drag forces exerted on i by all other species obeys an extended Stefan-Maxwell equation,

$$-c_{\mathrm{T}} y_i \vec{\nabla} \mu_i = \sum_{\substack{k=1 \\ k \neq i}}^{n} \frac{RT}{\mathscr{D}_{ik}} \left(y_k \vec{N}_i - y_i \vec{N}_k \right). \tag{2.16}$$

Here R is the gas constant, and $\mathscr{D}_{ij}$ is the Stefan-Maxwell coefficient that quantifies diffusional interactions between species i and j.

2.2.5 Closure of the multicomponent bulk-solution model

Table 2.1 denumerates a set of governing equations applicable to electrolytic transport under isothermal, isobaric conditions, along with the dependent variables involved. The table also lists the total number of dependent scalar variables (each vector is treated as d scalars, where d is the dimensionality of the geometry) and the total number of equations of each type (each vector equation is counted as d scalar equations); the numbers of unknowns and equations differ by $d - 1$, demonstrating model closure for one-dimensional simulations.

If transport occurs in two or three directions, the model in table 2.1 will be underdetermined. In such cases a kinematic relation like equation 2.10 may not be enough to specify the volume-average velocity; closure necessitates including pressure, and carrying a momentum balance alongside the other equations.[2] Appendix A discusses how multidimensional or non-isobaric models can be closed.

2.2.6 Constitutive laws for binary electrolytic solutions

Although the governing system outlined in Table 2.1 is valid generally, it is more typical to use mass balances in the form of the convective diffusion equation. After incorporating flux-explicit transport constitutive equations, the material balances for binary electrolytic solutions can be linearly recombined to obtain a single balance equation similar in form to equation 2.1, which is accompanied by two time-independent local balances of volume and charge.

Consider a salt with a single cation (index $k = +$, equivalent charge $z_+ > 0$) and anion ($k = -$, $z_- < 0$) dissolved in an electrically neutral solvent ($k = 0$, $z_0 = 0$). The

[2] A momentum balance and pressure variable may also be needed in one-dimensional systems to account for 'free convection', which occurs when the density gradients that accompany concentration polarization induce a buoyant force, causing a pressure gradient that drives bulk flow [76].

variables		governing equations		
#	symbol	#	description	equation
1	c_{T}	1	equation of state	Eq. 2.4
n	y_k	1	particle-fraction sum	Eq. 2.5
$n-1$	μ_k	$n-2$	material balances	Eq. 2.9
1	Φ	1	volume continuity	Eq. 2.10
d	$\vec{v}^{\square}$	1	charge continuity	Eq. 2.15
d	$\vec{i}$	d	definition of volume-	Eq. 2.8
nd	$\vec{N}_k$		average velocity	
		d	Faraday's law	Eq. 2.11
		1	electroneutrality	Eq. 2.12
		$n-1$	electrochemical pot'l	Eq. 2.13
			constitutive laws	
		$dn-d$	Stefan-Maxwell laws	Eq. 2.16

Table 2.1: Summary of model equations to describe excluded-volume effects in an isothermal, isobaric, locally electroneutral concentrated electrolytic solution comprising n species. The numbers of scalar dependent variables and equations are provided; vectors are taken to have dimensionality d. Note that the model is underdetermined if transport occurs in more than one direction.

electrolyte partial molar volume $\overline{V}_\mathrm{e}$ is defined as [32]

$$\overline{V}_\mathrm{e} = \nu_+ \overline{V}_+ + \nu_- \overline{V}_-, \tag{2.17}$$

where ν_k indicates the stoichiometry of ion k in a formula unit. A general composition variable y,

$$y = \frac{y_+}{\nu_+}, \tag{2.18}$$

can be adopted to describe local electrolyte content. The Guggenheim relation $z_+\nu_+ + z_-\nu_- = 0$ relates the ionic equivalent charges with their stoichiometries in a formula unit. Electroneutrality and the Guggenheim relation imply that $y = y_-/\nu_-$ as well.

In isothermal, isobaric systems, the total molar concentration and the solvent particle fraction both depend solely on the electrolyte content y. An electrolyte formula unit is taken to consist of $\nu = \nu_+ + \nu_-$ ions in total, so that equation of state 2.4 can be written as

$$\frac{1}{c_\mathrm{T}} = \overline{V}_0 + \left(\overline{V}_\mathrm{e} - \nu\overline{V}_0\right) y, \tag{2.19}$$

and particle-fraction sum 2.5 becomes

$$y_0 + \nu y = 1. \tag{2.20}$$

The Stefan-Maxwell equation describing the thermodynamic force driving solvent diffusion can be rearranged to get transport laws that express the excess ion fluxes relative to the solvent velocity. With equations 2.8 and 2.11, these yield a cation flux law with $\vec{v}^{\,\square}$ as the convective velocity,

$$\vec{N}_+ = \frac{\nu_+ \mathscr{D} \overline{V}_0 {c_\mathrm{T}}^2}{\nu RT} y_0 \vec{\nabla}\mu_0 + \frac{t_+^0 \vec{i}}{F z_+} + \nu_+ c_\mathrm{T} y \left(\vec{v}^{\,\square} - \frac{Q\vec{i}}{F}\right). \tag{2.21}$$

A similar equation was derived by Newman and Chapman [30]. Here

$$\mathscr{D} = \frac{(z_+ - z_-)\,\mathscr{D}_{0+}\mathscr{D}_{0-}}{z_+\mathscr{D}_{0+} - z_-\mathscr{D}_{0-}},\ t_+^0 = \frac{z_+\mathscr{D}_{0+}}{z_+\mathscr{D}_{0+} - z_-\mathscr{D}_{0-}}, \text{and } Q = \frac{\overline{V}_+ t_+^0}{z_+} + \frac{\overline{V}_-\,(1 - t_+^0)}{z_-} \tag{2.22}$$

define t_+^0 and the thermodynamic diffusion coefficient of the electrolyte, $\mathscr{D}$, in terms of Stefan-Maxwell coefficients; the additional property Q that appears [30] can be interpreted as an electro-osmotic coefficient for solvent relative to the volume-average velocity.

Volume-average velocity always appears in the combination $\vec{v}^{\,\square} - Q\vec{i}/F$ seen in the convective term of equation 2.21. Thermodynamic rigor requires this ambiguity because the partial molar volumes of individual ions are not measurable [77]. A solution to any physical problem will be invariant with respect to the value of Q in $\vec{v}^{\,\square} - Q\vec{i}/F$ because any boundary conditions that specify $\vec{v}^{\,\square}$ will prove to involve Q in the same proportion. It is conventional to take $Q = 0$ for simplicity—a convention adopted hereafter. As Newman and Chapman discussed, the convention allows individual ionic partial molar volumes to be computed in principle, but no physical significance should be attached to values so obtained [30]. To express the volume-average velocity in terms of the species fluxes under the convention that $Q = 0$, one can use equations 2.8 and 2.17, the Guggenheim relation, and t_+^0 from equation 2.22, yielding

$$\vec{v}^{\,\square} = \overline{V}_{\mathrm{e}}\left[\frac{(1 - t_+^0)}{\nu_+}\vec{N}_+ + \frac{t_+^0}{\nu_-}\vec{N}_-\right] + \overline{V}_0\vec{N}_0. \tag{2.23}$$

In equation 2.21, the chemical-potential driving force relates to electrolyte composition gradients through a Darken thermodynamic factor χ [78],

$$\frac{y_0}{\nu RT}\vec{\nabla}\mu_0 = -\chi\vec{\nabla}y. \tag{2.24}$$

Darken factors are usually expressed in terms of mean molar electrolyte activities,

such as $\lambda_{+-} = \lambda_+^{\nu_+/\nu}\lambda_-^{\nu_-/\nu}$; the definition here is equivalent through Gibbs-Duhem equation 2.14, which shows with equations 2.12 and 2.20 that[3]

$$\chi = 1 + \left(\frac{\partial \ln \lambda_0}{\partial \ln y_0}\right)_{T,p} = 1 + \left(\frac{\partial \ln \lambda_{+-}}{\partial \ln y}\right)_{T,p}. \tag{2.25}$$

With $Q = 0$, the cation flux is described in terms of composition gradients and the Darken factor as

$$\vec{N}_+ = -\nu_+ \mathscr{D}\chi \overline{V}_0 c_\mathrm{T}^2 \vec{\nabla} y + \frac{t_+^0 \vec{i}}{F z_+} + \nu_+ c_\mathrm{T} y \vec{v}^\square, \tag{2.26}$$

obtained by insertion of equation 2.24 into equation 2.21. Through equations 2.11 and 2.23, this law can also be used to express $\vec{N}_-$ and $\vec{N}_0$ in terms of $\vec{v}^\square$, $\vec{i}$, and $\vec{\nabla} y$.

2.2.7 Closure of the bulk binary-electrolyte model

Flux law 2.21 closes the governing system describing binary electrolytic transport. Material balances 2.9 govern cations, anions, and solvent. Elimination of $\vec{N}_-$ and $\vec{N}_0$ with equations 2.11 and 2.23, followed by insertion of equation 2.21 and rearrangement using equations 2.10 and 2.15, equation 2.12, the Guggenheim relation, equations 2.6 and 2.20, vector identities, and the convention $Q = 0$ result in the governing equations

$$\frac{\partial (c_\mathrm{T} y)}{\partial t} + \vec{v}^\square \cdot \vec{\nabla}(c_\mathrm{T} y) = \vec{\nabla} \cdot \left(\mathscr{D}\overline{V}_0 c_\mathrm{T}^2 \vec{\nabla} y\right) - \frac{\vec{i} \cdot \vec{\nabla} t_+^0}{F z_+ \nu_+} - c_\mathrm{T} y \vec{\nabla} \cdot \vec{v}^\square, \tag{2.27}$$

$$\vec{\nabla} \cdot \vec{v}^\square = -\frac{\overline{V}_\mathrm{e} \vec{i} \cdot \vec{\nabla} t_+^0}{F z_+ \nu_+} - \frac{\mathscr{D} c_\mathrm{T} \chi}{1 - \nu y} \vec{\nabla} y \cdot \vec{\nabla} \overline{V}_\mathrm{e}, \tag{2.28}$$

which hold in addition to charge-continuity equation 2.15.

Information about the cell potential is gained from a second independent Stefan-Maxwell equation (in addition to the solvent equation already used). The Stefan-Maxwell law expressing the force on cations is chosen here, although the force on

[3] Although apparently different, the definition of thermodynamic factor in equation 2.24 actually matches Newman's definition in terms of an activity based on molal concentration m [32]. In a binary, $\chi = \frac{c_\mathrm{T}}{c_0}\left[1 + \left(\frac{\partial \ln \gamma_{+-}}{\partial \ln m}\right)_{T,p}\right] = c_\mathrm{T}\overline{V}_0\left[1 + \left(\frac{\partial \ln f_{+-}}{\partial \ln c}\right)_{T,p}\right]$.

anions would be an equally valid alternative. With equations 2.4, 2.5, 2.11, 2.12, 2.19, 2.20, 2.22, and 2.24, the cation Stefan-Maxwell equation rearranges to

$$\vec{\nabla}\frac{\mu_+}{Fz_+} = -\frac{\vec{i}}{\kappa} + \frac{\nu RT\left(1-t_+^0\right)\chi}{Fz_+\nu_+}\vec{\nabla}\ln y, \tag{2.29}$$

in which the ionic conductivity κ is identified to be a function of electrolyte content y through

$$\frac{1}{\kappa} = \frac{RT\nu_+\nu_-\overline{V}_0}{\left(Fz_+\nu_+\right)^2 y}\left[\frac{y}{\mathscr{D}_{+-}} + \frac{1-\nu y}{\nu_-\mathscr{D}_{0+}+\nu_+\mathscr{D}_{0+}}\right]\left[1+\left(\frac{\overline{V}_\mathrm{e}}{\overline{V}_0}-\nu\right)y\right]. \tag{2.30}$$

Equation 2.29 is a MacInnes equation—a modified version of Ohm's law accounting for overpotentials that arise from electrolyte-composition gradients. Equilibria involving μ_+ can be used to establish a thermodynamic potential relative to a reference electrode of a given kind [74]. Alternatively, by choosing a reference state where $\mu_+^\ominus = 0$ and $\gamma_+ = 1$ in constitutive equation 2.13, it can be used to define Φ as a quasi-electrostatic potential referred to cations [79].

Table 2.2 lists dependent variables and governing equations that suffice to describe locally electroneutral concentrated binary electrolytic solutions in terms of a quasi-electrostatic potential Φ. Although they differ somewhat in their descriptions, the governing equations in table 2.2 follow directly from those in table 2.1 by a sequence of linear transformations. The number of variables again differs from the number of equations by $d-1$, demonstrating closure in one-dimensional systems without free convection. Six material properties are involved: thermodynamic properties $\overline{V}_0$, $\overline{V}_\mathrm{e}$, and χ; and transport properties $\mathscr{D}$, t_+^0, and κ. In isothermal, isobaric systems, these depend at most on the electrolyte composition distribution y.

variables		governing equations		
#	symbol	#	description	equation
1	c_{T}	1	equation of state	Eq. 2.19
1	y	1	electrolyte continuity	Eq. 2.27
1	μ_+	1	volume continuity	Eq. 2.28
1	Φ	1	charge continuity	Eq. 2.15
d	$\vec{v}^{\square}$	d	definition of volume-	Eq. 2.23
d	$\vec{i}$		average velocity	
d	$\vec{N}_+$	d	Faraday's law	Eq. 2.11
d	$\vec{N}_-$	d	cation flux law	Eq. 2.26
d	$\vec{N}_0$	d	MacInnes equation	Eq. 2.29
		1	cation electrochemical	Eq. 2.13
			potential constitutive law	$(k = +)$

Table 2.2: Equation system sufficient to describe solute-volume effects during one-dimensional transport in locally electroneutral concentrated binary electrolytic solutions at constant T and p. In addition to the ionic equivalent charges z_+ and z_-, and the stoichiometric numbers ν_+, ν_-, and $\nu = \nu_+ + \nu_-$, the system contains six material parameters, which depend at most on y: thermodynamic properties $\overline{V}_0$, $\overline{V}_{\mathrm{e}}$, and χ; and transport properties $\mathscr{D}$, t_+^0, and κ.

2.2.8 The simple binary electrolytic solution

Analysis in the next sections will focus on a 'simple' concentrated binary electrolytic solution of a binary electrolyte, for which the governing system in table 2.2 can be solved analytically in a number of circumstances. A simple binary electrolyte will be defined by the conditions that:

1. the partial molar volumes $\overline{V}_{\mathrm{e}}$ and $\overline{V}_0$ are independent of composition. This assumes that the solution density varies linearly with molar electrolyte concentration [32], an approximation that a substantial body of data suggests is fair when electrolytes are not near saturation [62, 80–82]. If density varies linearly with electrolyte molarity, then the solvent partial molar volume $\overline{V}_0$ must also equal the inverse molar concentration of the pure solvent.

2. the Stefan-Maxwell coefficients describing interactions with solvent, $\mathscr{D}_{0+}$ and $\mathscr{D}_{0-}$ (and consequently $\mathscr{D}$ and t_+^0), are relatively constant with composition. The validity of this approximation to first order has been justified by a number of experiments [28].

3. the thermodynamic factor χ is roughly constant with composition, so that the Fickian diffusivity D does not vary substantially when concentration polarization occurs. Electrochemists often make this assumption when analyzing voltammetry data by the Randles-Sevcik or Koutecky-Levich methods [83]; it has been demonstrated to hold very well for some lithium-ion-battery electrolytes [62].

For a simple binary electrolytic solution, the electrolyte and volume continuity equations simplify to

$$\frac{\partial y}{\partial t} + \vec{v}^{\,\square} \cdot \vec{\nabla} y = \mathscr{D}\chi \left[\nabla^2 y - \frac{2\left(\overline{V}_{\mathrm{e}} - \nu \overline{V}_0\right) \vec{\nabla} y \cdot \vec{\nabla} y}{\overline{V}_0 + \left(\overline{V}_{\mathrm{e}} - \nu \overline{V}_0\right) y} \right], \tag{2.31}$$

$$\vec{\nabla} \cdot \vec{v}^{\square} = 0, \tag{2.32}$$

while charge-continuity equation 2.15 retains the same form. MacInnes equation 2.29 can be path integrated to determine potential distributions.

The material balance presented in equation 2.31 involves two terms that do not appear in typical models—the $\vec{v}^{\square} \cdot \vec{\nabla} y$ term, which accounts for convection (Faradaic, free, or forced), and the term proportional to $\vec{\nabla} y \cdot \vec{\nabla} y$, which describes the excluded-volume effect.

2.2.9 Boundary conditions with solution flow

Boundary conditions that describe interfacial mass or charge exchange are needed to solve the governing systems in table 2.1 and 2.2. The present discussion will focus on heterogeneous Faradaic processes, in which interfacial electron exchange drives electrochemistry involving the species in solution and/or adjacent phases.

Generally an interfacial half-reaction can be written in the form

$$\sum_{k=1}^{n} s_k \mathrm{M}_k^{z_k} + \sum_{\substack{\text{species in} \\ \text{other phases}}} s_k \mathrm{M}_k^{z_k} \leftharpoons n_{\mathrm{e}^-} \mathrm{e}^-, \tag{2.33}$$

where n_{e^-} is the number of electrons exchanged; M_k represents the symbol for ionic, molecular, or atomic species k, and s_k, its reaction stoichiometry (s_k is positive for a product and negative for a reactant if the half-reaction is written as a reduction; it vanishes when a species does not react). The left side of the half-reaction balance contains two sums: one sum over the n species in the electrolytic-solution phase, governed by the equation systems summarized in tables 2.1 or 2.2; and one sum over species in other phases, which are not necessarily involved in the description of interior points within the electrolyte. Conservation of charge requires that $\sum_{\text{all species}} s_k z_k = n_{\mathrm{e}^-} z_{\mathrm{e}^-}$, where $z_{\mathrm{e}^-} = -1$ is the electron's equivalent charge and 'all species' counts both solution-phase constituents and those of other phases participating in the half-

reaction.

Given an interfacial electrochemical reaction in the form of equation 2.33, the flux of each species k should be driven by the electric current passing through the interface in proportion to its reaction stoichiometry. Forced or free convection may also occur with velocity $\vec{v}_{\text{conv}}$, which generally can vary independently of the current density [84]. Thus the total molar flux of species k normal to an interface is

$$\left(\vec{N}_k \cdot \vec{n}\right)\Big|_{\vec{S}} = \left[\left(y_k c_{\text{T}} \vec{v}_{\text{conv}} + \frac{s_k \vec{i}}{F z_{\text{e}^-} n_{\text{e}^-}}\right) \cdot \vec{n}\right]\Bigg|_{\vec{S}}, \tag{2.34}$$

where $\vec{S}$ is a vector function describing the evolution of interfacial position relative to a stationary frame, and $\vec{n}$ is a unit surface normal vector pointing from that interfacial position into the solution phase. (Note that the sign convention for s_k implies that $\vec{i}$ is an anodic current.)

To express the interfacial charge balance, multiply both sides of equation 2.34 by $F z_k$, sum over all liquid-phase species, and apply Faraday's law and electroneutrality,

$$\left(z_{\text{e}^-} n_{\text{e}^-} - \sum_{k=1}^{n} z_k s_k\right)\left(\vec{i} \cdot \vec{n}\right)\Big|_{\vec{S}} = 0. \tag{2.35}$$

The current density normal to an interface is therefore independent of $\vec{v}_{\text{conv}}$. Note that if all the charged species involved in half-reaction 2.33 come from the electrolytic solution phase, this equation holds true for any $\vec{i}$; otherwise, this equation may require that $\left(\vec{i} \cdot \vec{n}\right)\big|_{\vec{S}} = 0$.

2.2.10 Faradaic convection: definition

Multiplication of both sides of equation 2.34 by $\overline{V}_k$, summation over all species, insertion of equation 2.8, and simplification with equation 2.4 leads to an expression

for the volume-average velocity component normal to a boundary,

$$(\vec{v}^{\,\square} \cdot \vec{n})|_{\vec{S}} = \frac{\Delta \overline{V}^{\text{sol}}_{\text{rxn}}}{F z_{\text{e}^-} n_{\text{e}^-}} \left(\vec{i} \cdot \vec{n}\right)\Big|_{\vec{S}} + (\vec{v}_{\text{conv}} \cdot \vec{n})|_{\vec{S}}\,. \tag{2.36}$$

Here $\Delta \overline{V}^{\text{sol}}_{\text{rxn}}$ quantifies the solution-volume change per mole of limiting reactant as reaction 2.33 goes to completion,

$$\Delta \overline{V}^{\text{sol}}_{\text{rxn}} = \sum_{k=1}^{n} \overline{V}_k s_k. \tag{2.37}$$

Faradaic convection is formally defined as 'bulk mass transport associated with the portion of volume-average solution velocity driven by interfacial charge-transfer reactions', which is to say, the part of $\vec{v}^{\,\square}$ associated with $\left(\vec{i} \cdot \vec{n}\right)\Big|_{\vec{S}}$ in boundary-condition 2.36. After being induced at the interface, this part of $\vec{v}^{\,\square}$ is distributed across the solution phase in accord with volume continuity (equation 2.10, 2.28, or 2.32), driving bulk convection.

After inserting equation 2.26 into flux law 2.34 for cations, elimination of the volume-average velocity with equation 2.36 and introduction of y through equation 2.18 show that

$$-\left(c_{\text{T}}^2 \vec{\nabla} y \cdot \vec{n}\right)\Big|_{\vec{S}} = \left[\left(\frac{s_+ - \nu_+ c_{\text{T}} y \Delta \overline{V}^{\text{sol}}_{\text{rxn}}}{z_{\text{e}^-} n_{\text{e}^-}} - \frac{t_+^0}{z_+}\right) \frac{\vec{i} \cdot \vec{n}}{F \nu_+ \mathscr{D} \chi \overline{V}_0}\right]\Bigg|_{\vec{S}}, \tag{2.38}$$

a boundary condition that determines how Faradaic convection and migration lead to interfacial composition gradients, independent of $\vec{v}_{\text{conv}}$.

2.3 Symmetric deposition/stripping cells

2.3.1 Boundary and auxiliary conditions

Analysis of an experimental configuration can help to illustrate the impact of the excluded-volume effect and Faradaic convection on concentration profiles and current-voltage relationships. The rest of this discussion will focus on a parallel-electrode cell of the type shown schematically in figure 2.1—the 'symmetric deposition/stripping cell'. In such a cell both electrodes are imagined to be covered by solid films that can reversibly form from or decompose into constituents of the electrolyte. On one electrode, reaction 2.33 occurs in the anodic direction; on the other, it occurs cathodically. It will further be assumed that all the charged species involved in the deposition/stripping reaction come from the solution phase; that identical solid films form or degrade on both electrode surfaces; that the system is oriented to suppress the effects of free convection; and that there is no externally driven flow.

The most common example of this configuration is the 'plating/stripping cell', in which two identical metallic electrodes are separated by an electrolytic solution, and applied voltage or current causes metal ions to plate out of the solution phase on one electrode while being stripped into it from the other. Symmetric deposition/stripping cells have also been used for transport-property measurement by restricted diffusion and galvanostatic polarization, and for general characterization by electrochemical impedance spectroscopy [21, 23–25, 27, 62, 64].

Due to the congruence of the anodic and cathodic reactions, the masses of all species in the solution phase are conserved, so

$$\frac{1}{V}\int_{V} y_k c_{\mathrm{T}} dV = \langle c_k \rangle \,, \tag{2.39}$$

in which $\langle c_k \rangle$ represents the volume-averaged molar concentration of species k. (In an isothermal, isobaric solution at equilibrium, $c_k = \langle c_k \rangle$ uniformly for all species.)

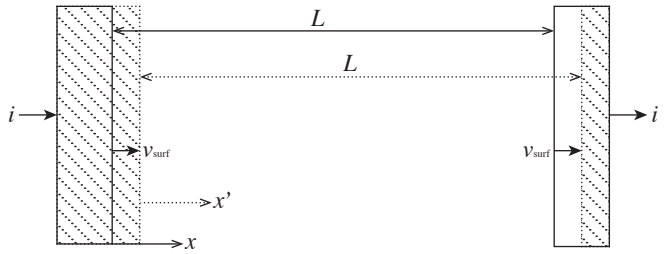

Figure 2.1: Schematic diagram of a planar symmetric deposition/stripping cell.

Equation 2.39 can be useful for describing galvanostatic steady states, in which flux boundary conditions may not suffice to specify concentration distributions.

When analyzing cells in the configuration shown in figure 2.1, it is critical to recognize that electrode surfaces can move as reactions progress, potentially changing the total volume between the electrodes or inducing flow. Generally the volume V in equation 2.39 may vary with time, and the interfacial position $\vec{S}$ in boundary conditions 2.34 through 2.36 should be taken to differ from its initial position $\vec{S}_0$ through a time integral of interfacial velocity $\vec{v}_{\text{surf}}$,

$$\vec{S}(t) - \vec{S}_0 = \int_0^t \vec{v}_{\text{surf}} dt. \tag{2.40}$$

Equation 2.33 distinguishes species in the electrolytic solution from those in other phases to isolate quantities that could contribute to this interfacial motion—a source of forced, rather than Faradaic, convection. In the absence of externally driven flow and free convection, one has that $\vec{v}_{\text{conv}} = \vec{v}_{\text{surf}}$ in equations 2.34 and 2.36.

Under the present circumstances, where it is assumed that all the species that leave the electrolytic-solution phase contribute to the growth or depletion of the solid deposition layers on the electrodes, the interfacial velocities are proportional to the current through

$$\vec{v}_{\text{surf}} = \frac{\Delta \overline{V}^{\text{surf}}_{\text{rxn}}}{z_{\text{e}^-} n_{\text{e}^-} F} \vec{i}, \text{ where } \Delta \overline{V}^{\text{surf}}_{\text{rxn}} = \sum_{\substack{\text{species in} \\ \text{other phases}}} \overline{V}_k s_k. \tag{2.41}$$

Application of local electroneutrality simplifies auxiliary condition 2.39 for a binary electrolyte in a symmetric deposition/stripping cell to

$$\frac{1}{V} \int_V y c_{\text{T}} dV = \langle c \rangle, \tag{2.42}$$

where $\langle c \rangle$ is the equilibrium electrolyte concentration.

Sundstrøm and Bark showed how the moving-boundary problem for a planar

symmetric deposition/stripping cell could be simplified by introducing a reference frame that moves uniformly at instantaneous velocity $\vec{v}_{\text{surf}}$ [61], a transformation detailed in Appendix B. The only changes to the governing system when thrown into the moving frame are that the boundaries appear stationary; that $\vec{v}_{\text{surf}}$ vanishes; and that all fluxes, currents, and velocities are rescaled to remove apparent convection due to the relative motion of the new coordinate system.

2.3.2 Dimensional analysis

It is convenient to non-dimensionalize the equations governing the experiment described in section 2.3.1. For transport along the x'-axis in a cell of thickness L (see figure 2.1), one can introduce dimensionless independent variables describing time τ and position ξ, as well as dependent variables describing electrolyte composition Y, current I, and flow rate (or Péclet number) $V^{\square}$,

$$\tau = \frac{\mathscr{D}\chi t'}{L^2},\ \xi = \frac{x'}{L},\ Y = \frac{y}{\langle y \rangle},\ I = \frac{i}{i_{\text{L}}^{\infty}},\ \text{and}\ V^{\square} = \frac{Lv^{\square}}{\mathscr{D}\chi}. \tag{2.43}$$

Composition y is scaled by $\langle y \rangle$ so that Y remains finite and of order 1 in the limit of extreme dilution; I is scaled by i_{L}^{∞}, the limiting current density at infinite dilution,

$$i_{\text{L}}^{\infty} = \frac{2Fz_+\nu_+\mathscr{D}\chi\langle c \rangle}{\left(\frac{s_+z_+}{z_{\text{e}^-}n_{\text{e}^-}} - t_+^0\right)L}, \tag{2.44}$$

so that its maximum value at steady state is of order 1. (Note the equivalence $\langle c \rangle = \langle c_{\text{T}} y \rangle = \langle c_{\text{T}} \rangle \langle y \rangle$.) Two parameters associated with solute-volume effects appear in the dimensionless governing system,

$$\alpha = \langle c \rangle \left(\nu \overline{V}_0 - \overline{V}_{\text{e}}\right) \ \text{and}\ \beta = \frac{z_+\nu_+\langle c \rangle \Delta\overline{V}_{\text{rxn}}^{\text{sol}}}{z_+s_+ - z_{\text{e}^-}n_{\text{e}^-}t_+^0}. \tag{2.45}$$

Both α and β are proportional to the average electrolyte concentration. In simple binary electrolytes, both properties are also constant with respect to composition.

Charge and volume continuity equations 2.15 and 2.32 take the dimensionless forms

$$\frac{\partial I}{\partial \xi} = 0 \text{ and } \frac{\partial V^{\square}}{\partial \xi} = 0. \tag{2.46}$$

These imply that current and volume-average velocity are independent of position, $I(\tau)$ and $V^{\square}(\tau)$. Application of boundary condition 2.36 shows that the Péclet number instantaneously relates to the current through

$$V^{\square}(\tau) = 2\beta I(\tau), \tag{2.47}$$

allowing the convective velocity to be eliminated from the governing system in favor of the current. Electrolyte balance equation 2.31 can thus be stated dimensionlessly as

$$\frac{\partial Y}{\partial \tau} + 2\beta I \frac{\partial Y}{\partial \xi} = \frac{\partial^2 Y}{\partial \xi^2} + \frac{2\alpha}{1 + (1 - Y)\alpha} \left(\frac{\partial Y}{\partial \xi} \right)^2, \tag{2.48}$$

a second-order partial differential equation on Y.

To set up current/voltage relationships, it is helpful to have a form of MacInnes equation 2.29, which transforms to

$$\frac{\partial u_+}{\partial \xi} = \frac{\partial \ln Y}{\partial \xi} - \frac{I}{\mathrm{K}}, \tag{2.49}$$

in which the dimensionless cation electrochemical potential u_+ is

$$u_+ = \frac{\nu_+ \mu_+}{\nu \chi RT \left(1 - t_+^0\right)}, \tag{2.50}$$

and K is a dimensionless conductivity,

$$\mathrm{K} = \frac{RT\nu\left(1-t_+^0\right)\kappa}{2F^2 z_+^2 \nu_+^2 \mathscr{D}\left\langle c\right\rangle} \cdot \left(\frac{s_+ z_+}{z_{\mathrm{e}^-} n_{\mathrm{e}^-}} - t_+^0\right). \tag{2.51}$$

Incorporating the variables and parameters defined in equations 2.43 and 2.45, boundary condition 2.38 becomes

$$\left.\frac{\partial Y}{\partial \xi}\right|_{\tau,0} = \left.\frac{2\left\{\beta Y - \left[1+\left(1-Y\right)\alpha\right]\right\}\left[1+\left(1-Y\right)\alpha\right] I}{1+\alpha}\right|_{\tau,0}, \tag{2.52}$$

and auxiliary condition 2.42 transforms to

$$\int_0^1 \frac{Y}{1+\left(1-Y\right)\alpha} d\xi = 1. \tag{2.53}$$

2.3.3 Quantification of volume effects

Equation 2.45 defines the two key properties that quantify solute-volume effects: the excluded-volume number α measures the solution volume change incurred when electrolyte is exchanged for solvent; the Faradaic-convection number β quantifies the solution volume change caused by interfacial reactions. Since I, Y and $\partial Y/\partial \xi$ are all of order unity in equations 2.48, 2.52, and 2.53, the general importances of the two solute-volume phenomena are signified directly by the magnitudes of α and β. In the limit of infinite dilution, both α and β tend to zero, and equation 2.48 reduces to Fick's second law. When both solvent and electrolyte have identical partial molar volumes, equation 2.48 reduces to the convective diffusion equation, as it would under the Nernst-Planck theory with constant ion mobilities.

Table 2.3 presents excluded-volume numbers for some exemplary solutions. The relative sizes of solute and solvent determine the sign and magnitude of α. When the electrolyte is relatively small compared to the solvent, α is positive. High-molar-mass solutes, such as tetraethylammonium tetrafluoroborate (teaBF$_4$), tetra-

solute	solvent	α	ref.	solute	solvent	α	ref.
HCl	H_2O	0.016	[80]	$LiBF_4$	DMA	0.164	[85]
HNO_3	H_2O	−0.002	[80]	$LiPF_6$	PC	0.117	[86]
KCl	H_2O	0.006	[80]	$LiPF_6$	EC:DEC	0.093	[87]
KOH	H_2O	0.021	[80]		1:1 by wt		
$AgNO_3$	H_2O	0.002	[80]	$LiPF_6$	ACN	−0.018	[87]
$AgClO_4$	H_2O	−0.010	[80]	$LiPF_6$	EC:EMC	0.115	[62]
$Cu(NO_3)_2$	H_2O	0.018	[80]		3:7 by wt		
LiCl	H_2O	0.017	[80]	$teaBF_4$	ACN	−0.079	[82]
LiBr	H_2O	0.010	[80]	$tbaBF_4$	ACN	−0.222	[82]
$LiNO_3$	H_2O	0.005	[80]	$tbaPF_6$	ACN	−0.230	[82]
Li_2SO_4	H_2O	0.040	[80]	bmimTFSI	ACN	−0.188	[82]
LiCl	DMA	0.178	[85]	$teaBF_4$	DMF	−0.044	[82]
LiBr	DMA	0.169	[85]	$tbaBF_4$	DMF	−0.167	[82]
LiI	DMA	0.163	[85]	$tbaPF_6$	DMF	−0.188	[82]
$LiClO_4$	DMA	0.163	[85]	bmimTFSI	DMF	−0.139	[82]

Table 2.3: Excluded-volume number α for various binary electrolytic solutions at ambient temperature, assuming a 1 M electrolyte concentration. For mixed solvents, α was computed by treating the mixture as a single solvent, with molar mass and molar density determined by mean stoichiometric proportion.

butylammonium hexafluorophosphate ($\mathrm{tbaPF_6}$), and 1-butyl-3-methyl imidazolium bis(trifluoromethyl sulfonyl)imide (bmimTFSI), have partial molar volumes much larger than typical solvents, leading α to be negative. In aqueous solutions, the partial molar volumes of solvent and solute are both relatively small, leading α to be of order 0.01 or smaller. In non-aqueous solutions, however, α is typically of order 0.1. Although the densities of solvents like dimethylacetamide (DMA), ethylene carbonate (EC), ethyl-methyl carbonate (EMC), propylene carbonate (PC), acetonitrile (ACN), and dimethylformamide (DMF) are comparable to the density of water, their molar masses are much greater, leading them to have much higher partial molar volumes.

One reason the Nernst-Planck dilute-solution theory works so well for typical aqueous electrolytes is that such solutions afford relatively small α, minimizing excluded-volume effects. Owing to its relatively large excluded-volume number, a given molarity in a non-aqueous solvent is effectively 'more concentrated' than an identical aqueous molarity, and the excluded-volume effect at that molarity is correspondingly much more significant.

Faradaic convection can also impact transport. For symmetric one-dimensional deposition/stripping cells, definition 2.45 combines with equations 2.17 and 2.37, equation 2.22 (with $Q = 0$), the Guggenheim condition, and the charge balance on half-reaction 2.33 to show that

$$\beta = \langle c \rangle \left(\overline{V}_{\mathrm{e}} + \frac{z_+ \nu_+ s_0 \overline{V}_0}{z_+ s_+ - z_{\mathrm{e}^-} n_{\mathrm{e}^-} t_+^0} \right). \tag{2.54}$$

Thus, in cells where solvent does not react ($s_0 = 0$), β equals the electrolyte volume fraction, and can be computed without any information about transport properties.

Table 2.4 provides Faradaic-convection numbers for cation plating/stripping cells, under the assumption that cations deposit from or dissolve into solution, but that solvent and anions do not react. Values of the Faradaic-convection number β range

solute	solvent	β	ref.	solute	solvent	β	ref.
$AgNO_3$	H_2O	0.034	[80]	LiI	DMA	0.023	[85]
$AgClO_4$	H_2O	0.046	[80]	$LiClO_4$	DMA	0.024	[85]
$Cu(NO_3)_2$	H_2O	0.037	[80]	$LiBF_4$	DMA	0.022	[85]
LiCl	H_2O	0.019	[80]	$LiPF_6$	PC	0.063	[86]
LiBr	H_2O	0.027	[80]	$LiPF_6$	EC:DEC	0.083	[87]
$LiNO_3$	H_2O	0.031	[80]		1:1 by wt		
Li_2SO_4	H_2O	0.014	[80]	$LiPF_6$	ACN	0.122	[87]
LiCl	DMA	0.008	[85]	$LiPF_6$	EC:EMC	0.059	[62]
LiBr	DMA	0.017	[85]		3:7 by wt		

Table 2.4: Faradaic-convection number β for various binary electrolytic solutions undergoing symmetric cation plating/stripping reactions in a one-dimensional cell at ambient temperature, assuming 1 M concentration. For mixed solvents, β was computed by treating the mixture as a single solvent, with molar mass and molar density determined by mean stoichiometric proportion.

between 0.01 and 0.1 for typical aqueous and non-aqueous solutions, and are greater than 0.05 for several lithium-ion-battery electrolytes.

If a Faradaic process reduces solvent ($s_0 < 0$), β can be negative if $z_+\nu_+ s_0 \overline{V}_0 / [(z_+ s_+ - z_{e^-} n_{e^-} t_+^0)\overline{V}_e] < -1$. Water is reduced at the cathode in a typical alkaline battery ($s_0 = -1/2$, $s_+ = 0$, $n_{e^-} = 1$), leading to a β for 1 M aqueous KOH of -0.019 ($\overline{V}_0 = 18$ cm^{3}mol^{-1} and $\overline{V}_e = 15$ cm^{3}mol^{-1} [80]; $t_+^0 = 0.2633$ [88]). In lithium batteries, electrochemical reactions with solvent can sometimes occur; in these cases, reasonable estimates of the cation transference number suggest that β will still be positive.

2.3.4 Statement as a standard convective-diffusion problem

Equation 2.48 does not appear to be amenable to an analytical solution. By introduction of the transformed dependent variable

$$C = \frac{Y}{1 + (1 - Y)\,\alpha} = \frac{c}{\langle c \rangle}, \tag{2.55}$$

however, equations 2.48, 2.49, 2.52, and 2.53 can be thrown into a linear differential balance on material involving a driving term proportional to $I(\tau)$,

$$\frac{\partial C}{\partial \tau} = \frac{\partial^2 C}{\partial \xi^2} - 2\beta I \frac{\partial C}{\partial \xi}, \tag{2.56}$$

which is subject to a Robin boundary condition

$$\left.\frac{\partial C}{\partial \xi}\right|_{\tau,0} = \left[2\,(\beta C - 1)\,I\right]_{\tau,0}, \tag{2.57}$$

and a linear auxiliary mass-conservation condition

$$\int_0^1 C(\tau, \xi)\, d\xi = 1, \tag{2.58}$$

accompanied by a nonlinear current-potential relation

$$\frac{\partial u_+}{\partial \xi} = \frac{1}{1+\alpha C}\frac{\partial \ln C}{\partial \xi} - \frac{I}{\mathrm{K}}. \tag{2.59}$$

For galvanostatic conditions, in which I is constant, equations 2.56 through 2.58 represent a linear differential system. After obtaining $C(\tau, \xi)$, potential distributions can be obtained by integration of (non-linear) equation 2.59.

If the applied current is fixed or mass-transfer limited, only β is needed to specify the distribution of molar concentration because α is not involved in equations 2.56 through 2.58. Although it does not affect concentration, the excluded-volume number α has a direct impact on the diffusion potential through equation 2.59, which arises from the use of a particle-fraction basis when defining χ. Thus, when approximations that justify the convective diffusion equation are applied in an electrolyte-transport analysis, one may still need to consider excluded-volume effects to predict potential distributions accurately.

2.4 Formulas for concentrations and overpotentials

This section focuses on solving equations 2.56 through 2.59. Analytical solutions of the governing system can be achieved to determine concentration profiles and current/ potential relationships for simple binary electrolytes in planar symmetric deposition/stripping cells under a variety of experimental control modes.

The analyses will always start with the determination of concentration profiles. Once these are available, the total diffusion potential Δu_+^{c} can be calculated by discarding the ohmic contribution to equation 2.49 (the term containing K),[4] then inte-

[4]To first order, $\mathscr{D}_{+-} \propto \sqrt{c}$ [28, 89]. Consequently, κ has a strong composition functionality, which tends to vary significantly among solutions, even when they are simple binary electrolytes. Ohmic losses will not be considered, but one could readily compute them by integrating the last term in equation 2.59 with an appropriate $\mathrm{K}(C)$.

grating both sides, showing that

$$\Delta u_+^{\mathrm{c}} = \int_1^0 \left[\frac{\partial u_+}{\partial \xi} + \frac{I(\tau)}{\mathrm{K}(Y(\tau,\xi))} \right] d\xi = \ln\left(\frac{Y(\tau,0)}{Y(\tau,1)} \right) = \ln\left(\frac{C(\tau,0)}{C(\tau,1)} \right) + \ln\left(\frac{1+\alpha C(\tau,1)}{1+\alpha C(\tau,0)} \right). \quad (2.60)$$

2.4.1 Steady-state galvanostatic concentration polarization

A first situation of interest is the steady-state response of the symmetric deposition/stripping cell under galvanostatic conditions. Concentration distributions with constant current will be notated with a superscript I.

At steady state $\partial C^I/\partial \tau = 0$ locally; let $C_{\mathrm{ss}}^I(\xi)$ represent the galvanostatic steady-state concentration distribution. Equations 2.56 through 2.58 are satisfied by

$$C_{\mathrm{ss}}^I(\xi) = \frac{e^{2\beta I} - 1 - 2(1-\beta)\beta I e^{2\beta I \xi}}{\beta\left(e^{2\beta I} - 1\right)}. \quad (2.61)$$

To calculate the dimensionless limiting current I_{L}, let $I = I_{\mathrm{L}}$ and $C_{\mathrm{ss}}^I(1) = 0$ in equation 2.61. This yields an implicit equation for I_{L},

$$I_{\mathrm{L}} = \frac{2(\beta I_{\mathrm{L}})^2}{2\beta I_{\mathrm{L}} + e^{-2\beta I_{\mathrm{L}}} - 1}. \quad (2.62)$$

Figure 2.2 shows how concentration profiles and the limiting current are affected by the Faradaic-convection number β. In dilute electrolytic solutions, β is very small; the concentration profiles become linear, and I_{L} approaches 1, in line with its definition. In more concentrated solutions, Faradaic convection becomes significant. The concentration profiles become curved due to the flow induced by Faradaic processes. Electrolytic solutions with positive β values can bear greater currents, while those with negative β tolerate smaller currents. Taking lithium plating from a 1 M $LiPF_6$ solution in ACN by way of example, the limiting current is around 9% higher than

that predicted assuming infinite dilution.

Figure 2.2(a) also demonstrates that when Faradaic convection is significant, it impacts the concentration polarization in two ways: the concentration difference between the two ends of the cell shrinks as β rises, and the minimum concentration deviates from the dilute-solution prediction according to the applied fraction of the limiting current. Both of these effects are summarized by the diffusion potential Δu_+^c. Figure 2.3(a) illustrates how the diffusion potential Δu_+^c varies with β and applied fraction of the limiting current when the excluded-volume effect is negligible ($\alpha = 0$). Increasing β decreases the diffusion potential at a given current.

The impacts of the excluded-volume number α and Faradaic-convection number β on diffusion potential at $I/I_L = 0.5$ are summarized in figure 2.3(b). Increasing α and β both decrease overpotential. Potential loss induced by cell polarization is suppressed in electrolytic systems with positive α and β values; the potential loss may be larger than expected if either parameter is negative.

2.4.2 Galvanostatic transients

To elucidate the transient relaxation of an initially equilibrated deposition/stripping system in response to an ongoing galvanostatic pulse, governing equation 2.56 can be solved subject to boundary condition 2.57 and auxiliary condition 2.58, with initial condition

$$C^I(0,\xi) = 1. \tag{2.63}$$

The transient concentration distribution is given by

$$C^I(\tau,\xi) = C_{ss}^I(\xi) - 4(1-\beta) I e^{\beta I\xi - \beta^2 I^2 \tau} \times \sum_{m=1}^{\infty} A_m e^{-m^2\pi^2\tau}\left[\cos(m\pi\xi) + \frac{\beta I \sin(m\pi\xi)}{m\pi}\right], \tag{2.64}$$

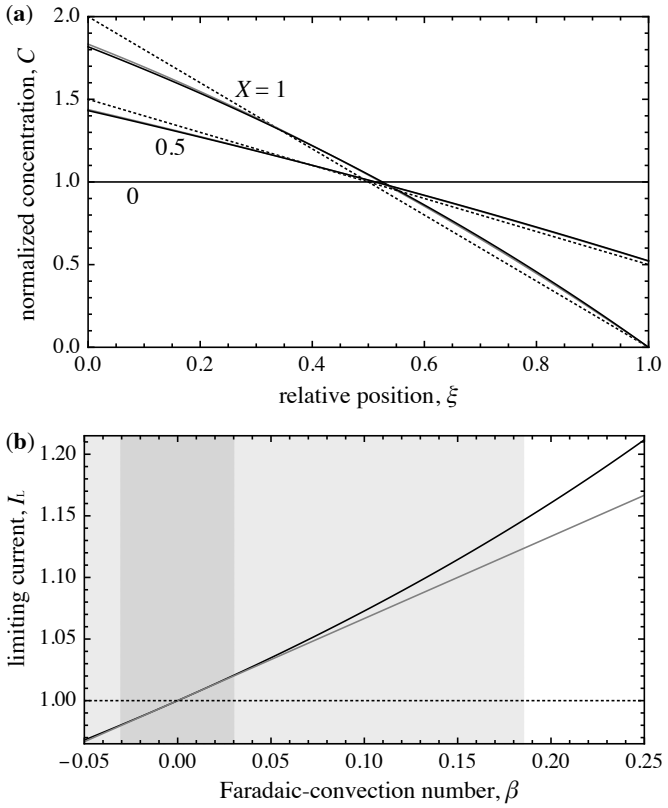

Figure 2.2: Effect of Faradaic convection on concentration profiles and limiting currents. (a) Concentration profiles with $\beta = 0.25$ at three limiting-current fractions $X = I/I_{\mathrm{L}}$. Dotted lines show profiles when $\beta \to 0$; black curves show exact profiles from equation 2.61; gray curves show first-order asymptotic profiles from equation 2.73, which coincide almost exactly with the exact ones. (b) The black curve shows $I_{\mathrm{L}}\,(\beta)$ from equation 2.62; the gray line is the first-order approximation from equation 2.72. The approximation is accurate within 2% in the light gray domain; dilute-solution theory ($I_{\mathrm{L}} = 1$) is accurate within 2% in the dark gray domain.

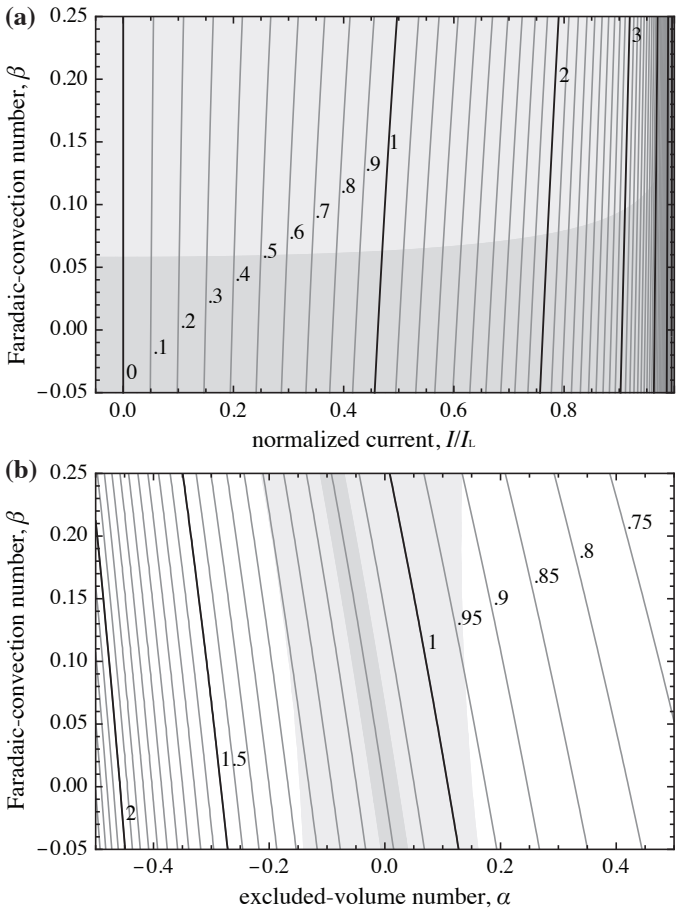

Figure 2.3: Impact of electrolyte volume on diffusion potential. (a) Δu_+^c as a function of β and applied fraction of the limiting current, I/I_L, with α=0; (b) Δu_+^c as a function of β and α at I/I_L = 0.5. The asymptotic solution from equations 2.73 and 2.80 is accurate within 2% in the light gray domains; the dilute-solution theory (α = β = 0) is accurate within 2% in the dark gray domains.

in which the Fourier amplitudes A_m are

$$A_m = \frac{1 - (-1)^m e^{-\beta I}}{m^2\pi^2\left[1 + \left(\frac{\beta I}{m\pi}\right)^2\right]^2}. \tag{2.65}$$

Here there is a convective relaxation time involving the Péclet number $2\beta I$, as well as a diffusional relaxation corresponding to the square of the first eigenvalue, π^2. These two characteristic times—both longer than double-layer relaxation—may be observed in systems where Faradaic convection is significant. Multiple time constants that are longer than the expected double-layer relaxation time have been observed during transference-number measurements by galvanostatic polarization [27].

At very short times ($\tau << 1$) the solution given by equation 2.64 exhibits the Gibbs phenomenon. To obtain a solution of equation 2.56 valid near $\xi = 0$ in the regime of small Fourier number, use boundary condition 2.57 and initial condition 2.63, but replace auxiliary condition 2.58 with a condition describing a semi-infinite geometry,

$$\lim_{\xi\to\infty} C^I(\tau,\xi) = 1. \tag{2.66}$$

Near the inner electrode ($\xi = 0$), a concentration distribution satisfying the governing equation and boundary conditions is given in terms of a series of repeated integrals of the error function complement [90] as

$$\lim_{\tau<<1} C^I(\tau,\xi) = 1 + 4e^{\beta I\xi - \beta^2 I^2\tau}(1-\beta)\times \sum_{m=1}^{\infty} \frac{m}{2\beta}\left(2\beta I\sqrt{\tau}\right)^{2m-1}\left[\mathrm{i}^{2m-1}\mathrm{erfc}\left(\frac{\xi}{2\sqrt{\tau}}\right) - 2\beta I\sqrt{\tau}\,\mathrm{i}^{2m}\mathrm{erfc}\left(\frac{\xi}{2\sqrt{\tau}}\right)\right]. \tag{2.67}$$

To obtain a solution valid near the outer electrode ($\xi = 1$), an opposing concentration distribution can be obtained by replacing I with $-I$ and ξ with $1-\xi$ in equation 2.67.

2.4.3 Cottrell equation

A final analytical solution comparable to a canonical result is provided by analyzing the short-time system response to a step change in potential when Nernstian equilibrium maintains at the plane electrode surface of a semi-infinite system—the assumptions typically used when deriving the classical Cottrell equation [83, 91]. In this case, one again only considers the electrode near $\xi = 0$, and the concentration distribution is determined by solving governing equation 2.56 subject to initial condition 2.63 and boundary condition 2.66. Boundary condition 2.57 can be replaced with a Dirichlet condition at the inner electrode,

$$C^{\Phi}(\tau, 0) = \Delta C_0 + 1, \tag{2.68}$$

where ΔC_0 is the surface excess concentration and the superscript Φ indicates that the applied potential is fixed. A similarity transformation then shows that the concentration distribution evolves according to

$$C^{\Phi}(\tau, \xi) = 1 + \frac{\Delta C_0 \operatorname{erfc}\left(\frac{\xi}{2\sqrt{\tau}} - \frac{\beta \Delta C_0 k}{\sqrt{\pi}}\right)}{\operatorname{erfc}\left(-\frac{\beta \Delta C_0 k}{\sqrt{\pi}}\right)}, \tag{2.69}$$

while the current varies with time as

$$I^{\Phi}(\tau) = \frac{\Delta C_0 k}{2\sqrt{\pi \tau}} \tag{2.70}$$

These functions involve a parameter k that quantifies the deviation from the typical result of dilute-solution theory ($\lim_{\beta \to 0} k = 1$). An implicit formula for k in terms of the surface excess concentration ΔC_0 and the Faradaic-convection number β is

obtained by inserting equations 2.69 and 2.70 into boundary condition 2.57, yielding

$$k = \frac{\exp\left[-\left(\frac{\beta\Delta C_0 k}{\sqrt{\pi}}\right)^2\right]}{\operatorname{erfc}\left(-\frac{\beta\Delta C_0 k}{\sqrt{\pi}}\right)\left[1-\beta\left(1+\Delta C_0\right)\right]}. \tag{2.71}$$

Figure 2.4 shows how the current-evolution parameter k depends on surface excess concentration ΔC_0 and the Faradaic convection number β. Typically k rises with ΔC_0 when $\beta > 0$, and decreases with ΔC_0 when $\beta < 0$.

2.4.4 Asymptotic formulas with solute-volume effects

Since both α and β tend to be of order 0.1, it is worthwhile to perform asymptotic expansions of the non-linear equations from the previous section for use in the limit $|\beta| << 1$ and $|\alpha| << 1$. The light-gray-shaded regions in figures 2.2 through 2.4 indicate the domains of parameters wherein first-order expansions match the exact solutions within 2%. Agreement between the first-order and exact solutions is quite good within practical ranges of α and β.

The galvanostatic systems are imagined to be operated under a specified applied fraction of the limiting current, $X = I/I_{\mathrm{L}}$. Either by formal Maclaurin expansion of the exact solution or by a regular perturbation analysis, the limiting current up to first order in β is found to be

$$I_{\mathrm{L}} \approx I_{\mathrm{L}}^{(0)} + I_{\mathrm{L}}^{(1)}\beta + O\left(\beta^2\right) = 1 + \tfrac{2}{3}\beta + O\left(\beta^2\right), \tag{2.72}$$

while the steady-state concentration distribution is

$$C_{\mathrm{ss}}^{I}(\xi) \approx C_{\mathrm{ss}}^{I(0)} + \beta C_{\mathrm{ss}}^{I(1)} + O\left(\beta^2\right), \text{ where}$$
$$C_{\mathrm{ss}}^{I(0)} = 1 + X\left(1-2\xi\right) \text{ and } C_{\mathrm{ss}}^{I(1)} = -X\left\{\tfrac{1}{3}\left(1-2\xi\right) + X\left[\tfrac{1}{3} - 2\xi\left(1-\xi\right)\right]\right\}. \tag{2.73}$$

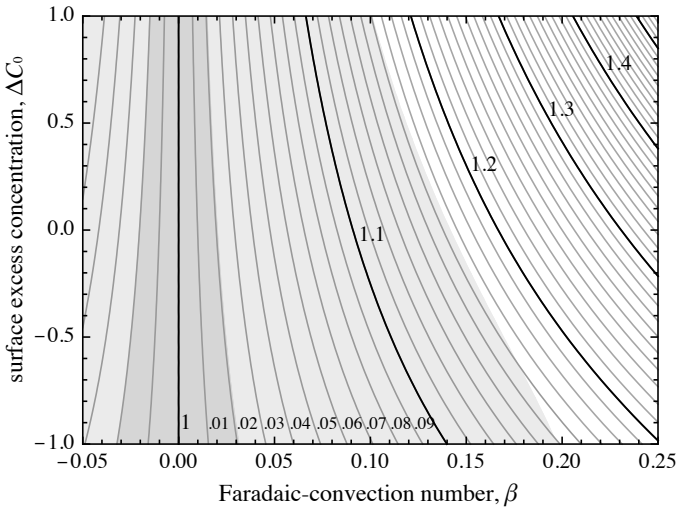

Figure 2.4: Contour plot of the current-evolution parameter k as a function of electrolyte surface excess concentration ΔC_0 and Faradaic-convection number β. The asymptotic equation 2.79 is accurate within 2% in the light gray domain, and the dilute-solution-theory value ($k = 1$) is accurate within 2% in the dark gray domain.

The expressions for $I_{\mathrm{L}}^{(0)}$ and $C_{\mathrm{ss}}^{I(0)}$ are familiar results from dilute-solution theory [92]. The galvanostatic transient concentration as $\beta \to 0$ also matches the literature [92],

$$C^{I(0)}(\tau,\xi) = C_{\mathrm{ss}}^{I(0)} + C_{\mathrm{t}}^{I(0)}, \text{ where}$$
$$C_{\mathrm{t}}^{I(0)} = -2X \sum_{m=1}^{\infty} \frac{e^{-4(m-\frac{1}{2})^2\pi^2\tau} \cos\left[2\left(m-\frac{1}{2}\right)\pi\xi\right]}{\left(m-\frac{1}{2}\right)^2\pi^2}. \quad (2.74)$$

The transient concentration is corrected to first order as

$$C^{I}(\tau,\xi) \approx C^{I(0)} + \beta C^{I(1)} + O\left(\beta^2\right), \text{ where}$$
$$C^{I(1)} = C_{\mathrm{ss}}^{I(1)} - \left[\tfrac{1}{3} + \tfrac{1}{2}X(1-2\xi)\right] C_{\mathrm{t}}^{I(0)} - X^2 \sum_{m=1}^{\infty} \frac{e^{-4(m-\frac{1}{2})^2\pi^2\tau} \sin\left[2\left(m-\frac{1}{2}\right)\pi\xi\right]}{\left(m-\frac{1}{2}\right)^3\pi^3}$$
$$- X^2 \sum_{m=1}^{\infty} \frac{e^{-4m^2\pi^2\tau}\cos(2m\pi\xi)}{m^2\pi^2}. \quad (2.75)$$

The short-time transient solution valid near $\xi = 0$ asymptotically satisfies

$$\lim_{\tau<<1} C^{I}(\tau,\xi) = \lim_{\tau<<1}\left[C^{I(0)} + \beta C^{I(1)} + O\left(\beta^2\right)\right], \text{ where}$$
$$\lim_{\tau<<1} C^{I(0)} = 1 + 4X\sqrt{\tau}\,\mathrm{ierfc}\left(\tfrac{\xi}{2\sqrt{\tau}}\right) \text{ and}$$
$$\lim_{\tau<<1} C^{I(1)} = \left(\tfrac{3}{2}X\xi - \tfrac{1}{3}\right)\left(\lim_{\tau<<1} C^{I(0)} - 1\right) - 2X^2\tau\,\mathrm{erfc}\left(\tfrac{\xi}{2\sqrt{\tau}}\right). \quad (2.76)$$

Here the zero-order solution, $\lim_{\tau<<1} C^{I(0)}$, agrees with the formula from dilute-solution theory that underpins the theory of galvanostatic polarization measurements [21, 25].

Finally, a Cottrell equation corrected to first order for Faradaic convection can be determined. First, the concentration distribution is given up to order β by

$$\lim_{\tau<<1} C^{\Phi}(\tau,\xi) = \lim_{\tau<<1}\left[C^{\Phi(0)} + \beta C^{\Phi(1)} + O\left(\beta^2\right)\right],$$
$$\text{where } \lim_{\tau<<1} C^{\Phi(0)} = 1 + \Delta C_0\,\mathrm{erfc}\left(\frac{\xi}{2\sqrt{\tau}}\right) \text{ and}$$
$$\lim_{\tau<<1} C^{\Phi(1)} = \tfrac{2}{\pi}\Delta C_0^2\left[\exp\left(-\tfrac{\xi^2}{4\tau}\right) - \mathrm{erfc}\left(\tfrac{\xi}{2\sqrt{\tau}}\right)\right]. \quad (2.77)$$

It follows that the current distribution satisfies

$$\lim_{\tau<<1} I^{\Phi}(\tau) = \frac{\Delta C_0}{2\sqrt{\pi\tau}}\left\{1+\beta\left[1+\left(1-\tfrac{2}{\pi}\right)\Delta C_0\right]+O\left(\beta^2\right)\right\}. \tag{2.78}$$

The zero-order term matches the classical Cottrell equation exactly; in the limit $\beta \to 0$, $k \to 1$ and $I \to \Delta C_0/\sqrt{4\pi\tau}$. A comparison between equation 2.70 and 2.78 also gives an asymptotic equation for calculating the current-evolution parameter,

$$k = k^{(0)} + \beta k^{(1)} + O\left(\beta^2\right) = 1+\beta\left[1+\left(1-\tfrac{2}{\pi}\right)\Delta C_0\right]+O\left(\beta^2\right). \tag{2.79}$$

To evaluate the impact of the excluded-volume number α, one can perform an asymptotic expansion of the MacInnes equation. Up to second order in both solute-volume numbers, the diffusion potential is

$$\begin{aligned}\Delta u_+^{c} = \Delta u_+^{c(0)} &+ \alpha\left[C^{(0)}(\tau,1) - C^{(0)}(\tau,0)\right] \\ &+ \beta\left[\frac{C^{(1)}(\tau,0)}{C^{(0)}(\tau,0)} - \frac{C^{(1)}(\tau,1)}{C^{(0)}(\tau,1)}\right] + O\left(\alpha^2\right) + O(\alpha\beta) + O\left(\beta^2\right), \\ &\text{where } \Delta u_+^{c(0)} = \ln\left(\frac{C^{(0)}(\tau,0)}{C^{(0)}(\tau,1)}\right)\end{aligned} \tag{2.80}$$

The zero-order term is the standard Nernstian overpotential. A correction of order α involves the zero-order concentration polarization, $C^{(0)}(\tau,1) - C^{(0)}(\tau,0)$; the first-order concentration distributions are involved in a correction of order β.

2.5 Conclusion

Two solute-volume effects intrinsic to transport in electrolytes have been considered: the excluded-volume effect, associated with a dimensionless number α, and Faradaic convection, associated with a number β. The excluded-volume effect is important in solutions where significant differences exist among species partial molar

volumes, and where partial molar volumes are relatively large. Faradaic convection is significant when electrode reactions induce substantial solution-volume changes—typically when heterogeneously reacting components occupy a large volume fraction of the solution phase. The impacts of both effects increase with electrolyte concentration, but may also be important at more moderate concentrations in non-aqueous electrolytes. A comprehensive analysis has been conducted to study quantitatively the influences of solute-volume effects on planar, symmetric deposition/stripping cells subjected to galvanostatic polarization or step changes in potential. Faradaic convection usually reduces concentration polarization and raises the apparent limiting current; depending on the relative sizes of electrolyte and solvent molecules, the excluded-volume effect may either reduce or increase diffusion potentials.

Fitting of experimental current/voltage data is involved in most of the standard transport-property measurement techniques. But data are usually fit using equations that neglect solute-volume effects altogether. This chapter demonstrates that the experimental current/voltage data for, say, a typical lithium-ion-battery electrolyte in a symmetric plating/stripping cell (expected to have significant values of α and β, *cf.* tables 2.3 and 2.4) will exhibit features arising from solute-volume effects. When fit by a model that neglects such effects, systematic errors may be induced that cause parameters derived from data fitting to be either inaccurate or inconsistent with other experimental observations.

By way of example, consider a non-aqueous Li-ion electrolyte at moderate molarity (which experimental data summarized in this paper suggest will have a β value around 0.05, or even as large as 0.15 if its concentration is above 1 M). If a restricted-diffusion measurement is performed with a symmetric plating/stripping cell to measure the electrolyte diffusivity, that measurement will yield a diffusivity that underpredicts the experimentally observed limiting current by a factor of approximately $1 - \frac{2}{3}\beta$ when inserted into the usual formula for plane geometries. Alternatively, if a

linear-sweep voltammetry experiment on the same cell is used to measure a limiting current, and the standard formula is used to extract the diffusivity from that datum, the diffusivity so determined will be artificially high by a factor of approximately $1 + \frac{2}{3}\beta$, because the standard equation neglects Faradaic convection. The ramifications for parameters gathered from galvanostatic-polarization experiments, which involve a constant-current pulse (in which Faradaic convection will be significant in determining the end-of-pulse concentration profile) followed by an open-circuit hold wherein diffusion-potential relaxation is recorded (during which time the excluded-volume effect is significant), are much harder to parse; they will be addressed in future work.

CHAPTER III

Electrolyte Property Measurements

3.1 Introduction

The complete description of mass transfer in an electrolytic system composed of n species requires $n\,(n-1)\,/2$ transport properties [32, 33]. For a binary electrolytic solution comprising three species (cations, anions, and solvent), these fundamental transport properties are ionic conductivity, κ, cation transference number, t_+^0, and thermodynamic electrolyte diffusivity, $\mathscr{D}$. In addition, three thermodynamic properties are needed to describe a concentrated binary electrolyte: a volumetric state equation incorportates partial molar volumes for the dissolved electrolyte and the solvent, $\overline{V}_{\mathrm{e}}$ and $\overline{V}_0$, respectively; nonideal solution energetics are accounted for by a thermodynamic factor, χ. Thermodynamic factors are particularly important because they can be strongly composition dependent [62]; the time scales over which concentration nonuniformities relax are determined by the Fickian diffusivity $D = \mathscr{D}\chi$, rather than the thermodynamic diffusivity [30].

Ionic conductivity is directly measurable, and is typically quantified using DC conductometry [93, 94] or impedance spectroscopy [95, 96]. Partial molar volumes are not directly measurable, but their composition dependences can be quantified independently of the other properties *via* densitometry [82, 97]. The remaining three solution properties are not directly measurable, and cannot be measured in isolation;

values of $\mathscr{D}$, t_+^0, and χ must be deconvoluted from the results of three independent experiments. When the three experiments are potentiometric, deconvolution of $\mathscr{D}$, t_+^0, and χ involves the use of theoretical expressions for the dependence of measured cell voltage on composition.

Ma *et al.* developed a standard battery of three independent potentiometric experiments to establish $\mathscr{D}$, t_+^0, and χ [21]. A 'concentration cell' is fabricated, in which two electrolytic solutions with different concentrations are put in chemical contact using a porous membrane that prevents significant mixing during the experimental period; the open-circuit voltage of such a cell after quasi-equilibrium is reached relates to χ and t_+^0 [27, 62]. A planar electrolytic cell with parallel electrodes that reversibly produce or consume species from the solution phase (and produce no new liquid-phase species) is used for the other two measurements. In a 'restricted diffusion' experiment, a non-uniform concentration distribution is induced in the cell; the relaxation of concentration polarization at long times depends on $\mathscr{D}$ and χ [30, 98], and can be tracked by recording the transient open-circuit voltage [22, 30]. In a 'galvanostatic polarization' experiment, a short current pulse is applied to produce diffusion boundary layers near the electrode surfaces; the open-circuit voltage relaxation at times before the boundary layers come into contact depends on $\mathscr{D}$, t_+^0, and χ [21, 99]. Restricted-diffusion and galvanostatic-polarization experiments can both be implemented with the same cell, since a current pulse can be used to establish the non-uniform concentration distribution for restricted diffusion. In practice, the two experiments need to be run separately, to achieve good signal-to-noise ratios for voltages in the short-time and long-time relaxation regimes.

Theoretical expressions were provided by Ma *et al.* [21] to cast the voltage transients observed during potentiometric restricted-diffusion and galvanostatic-polarization experiments in terms of $\mathscr{D}$, t_+^0, and χ. A number of restrictions apply to their analysis. In particular, the theory requires that concentration differences are

relatively small, despite the fact that large concentration differences may need to be imposed to get an adequate signal during chronopotentiometry. Also, the theory requires that electrolyte convection associated with current pulses is negligible – but this effect can be significant for moderately concentrated non-aqueous electrolytes [100].

Although Ma *et al.* obtain sensible property data [21], some implementations of their characterization protocol by others have led to surprising results for lithium-battery electrolytes. These include unexpectedly high diffusivities [27] and low – or even negative – transference numbers [24]. In light of these observations, this chapter aims to serve three primary purposes. First, the theory underpinning measurement of $\mathscr{D}$, t_+^0, and χ in planar electrolytic cells is extended, to relax the assumptions of low concentration polarization and negligible Faradaic convection. Second, several relationships are provided to help guide experimentalists in the future design of galvanostatic-polarization experiments. Third, this extended theory is used to rationalize the counterintuitive observations made by prior researchers, whose experimental protocols may have violated the theoretical assumptions stated by Ma *et al.*

3.2 Analysis and discussion

3.2.1 Electrolyte composition bases

Solute molalities m_k are the most typical composition basis used to express the composition dependences of solution properties, primarily because they are very precisely quantifiable: to make a solution of a given molality does not require a volume measurement, and, since they are referred to solvent mass, molalities are independent of temperature and pressure. Although solvent molality is conveniently constant (equaling the inverse of its molar mass M_0), the molalities of solutes become very

large when little solvent is present, and diverge when there is no solvent. Thus molality is a difficult composition basis to apply to very concentrated solutions. The need to specially identify a particular species as a 'solvent' also forces some degree of arbitrariness when describing mixed-solvent systems on a molal basis.

Molar species concentrations c_k are bounded throughout the entire domain of miscibility and treat all species on equal footing, avoiding the problems associated with molality in very concentrated or multiple-solvent systems. The molar basis places strict limits on experimental precision, however, because solution preparation involves a volume measurement. Since solution densities depend on temperature T, pressure p, and local composition, the use of a molar basis can easily lead to systematic errors in property measurements. The T and p dependences of molarity also make it vague as a basis for solution properties in coupled transport scenarios.

Species particle fractions y_k have the advantage of molality, because they are independent of T and p, and also of molarity, because they apply equally to all the species in a system and have finite bounds. They are convenient from a theoretical standpoint because they are dimensionless and bounded between 0 and 1. As a basis for activity they are also useful, because chemical-potential constitutive laws in which species activities are based on particle fractions satisfy the Gibbs-Duhem equation naturally in the ideal-solution limit.

When electrolytic solutions are in thermodynamic equilibrium, or when they are observed on length scales relevant to macroscpic transport phenomena, their ion contents satisfy a local electroneutrality relationship. Thus one does not need to distinguish the cation particle fraction y_+ and the anion particle fraction y_-. Letting ν_+ and ν_- represent the ion stoichiometries in a formula unit of salt, a single composition variable

$$y = \frac{y_+}{\nu_+} = \frac{y_-}{\nu_-} \tag{3.1}$$

can be used. The quantity y represents the number of salt formula units, scaled by

the total number of ion and solvent particles (*i.e.*, the numbers of all three species) in solution. The particle-fraction basis relates to salt molarity m and salt molarity c through

$$y(m) = \frac{mM_0}{1 + \nu m M_0} \quad \text{and} \quad y(c) = \frac{c\overline{V}_0}{1 + c\left(\nu\overline{V}_0 - \overline{V}_e\right)}, \tag{3.2}$$

in which $\nu = \nu_+ + \nu_-$ stands for the total number of ions in a formula unit of salt.

3.2.2 Basic thermodynamics

Consider a general electrolytic cell containing a simple binary electrolyte, which is diagrammed using the standard schematic representation [32, 83] in Figure 3.1. The half-reactions at each of the electrodes (α and α') can be expressed in the form

$$\text{species in electrode \& other phases} + s_+ \mathrm{M}^{z_+} + s_- \mathrm{X}^{z_-} + s_0 \mathrm{N} \rightleftharpoons n_{e^-} e^- . \tag{3.3}$$

The cell in Figure 3.1 is taken to be 'symmetric', in the sense that the reaction stoichiometric coefficients s_k are the same in both electrode reactions; the number of electrons transferred, n_{e^-}, should also be the same.[1] Fabrication of a symmetric electrolytic cell does not require that both half reactions are identical: the components in other phases (if present) and their involvement in the electrode reactions can generally differ.[2]

When no current is allowed to pass through the cell in Figure 3.1, the change in open-circuit potential (ΔU, abbreviated as OCP) arising from the composition

[1] Note that s_k is positive for a product and negative for a reactant when half-reaction 3.3 is written as a reduction. If the species in the electrodes and other phases are uncharged, conservation of charge requires that $\sum_k s_k z_k = n_{e^-} z_{e^-}$, where $z_{e^-} = -1$ is the equivalent charge of electrons.

[2] For instance, a standard alkaline battery can be considered to be a symmetric electrolytic cell: both cell half-reactions involve the same number of electrons, and both electrodes react with solvent (water) and anions (hydroxide) in the same proportions.

Figure 3.1: Schematic drawing of a general electrolytic cell containing a simple binary electrolyte. M, X, and N are the chemical symbols of cations, anions, and solvent, respectively, and z_+ and z_- are the ionic equivalent charges.

change across the transition region is given by the path integral

$$F\int_{\delta}^{\delta'} dU = \frac{s_+}{n_{e^-}}\int_{\delta}^{\delta'} d\mu_+ + \frac{s_-}{n_{e^-}}\int_{\delta}^{\delta'} d\mu_- + \frac{s_0}{n_{e^-}}\int_{\delta}^{\delta'} d\mu_0. \tag{3.4}$$

Here μ_k represents the electrochemical potential of species k and F is Faraday's constant. Equation 3.4 for the OCP difference holds true so long as there is an unbroken path of chemical contact that can be traversed from δ to δ'. The 'transition region' in Figure 3.1 is meant to represent any means by which this continuous contact is supported: it can be a fabricated liquid junction (*e.g.*, a glass frit or a porous membrane in a concentration-cell experiment), or simply a nonuniform distribution of composition in the intermediating liquid between two electrodes.

Equation 3.4 can be simplified to an expression dependent only on y using thermodynamic principles and standard constitutive laws. The salt dissociation equilibrium $\mu_e = \nu_+\mu_+ + \nu_-\mu_-$ can be used to eliminate μ_-; the isothermal, isobaric, electroneutral Gibbs-Duhem equation, in the form $yd\mu_e + y_0 d\mu_0 = 0$, then allows elimination of the chemical potential of the salt. Changes in the chemical potential of the solvent relate to changes in the electrolyte composition through a constitutive law that defines χ [100],

$$d\mu_0 = -\frac{\nu RT\chi}{y_0}dy, \tag{3.5}$$

so terms involving the solvent chemical potential can be replaced with terms involving y. Incorporation of the MacInnes equation under a condition of zero current [100] allows $d\mu_+$ to be eliminated in favor of dy as well. Finally, under isothermal, isobaric conditions, thermodynamic consistency requires that $U(y)$ only. Thus one can write

$$\int_{\delta}^{\delta'}\left\{\frac{dU}{d\ln y} - \frac{\nu RT\chi}{F}\left[\frac{s_+}{n_{e^-}\nu_+} - \frac{z_{e^-}t_+^0}{z_+\nu_+} - \frac{s_0 y}{n_{e^-}(1-\nu y)}\right]\right\} d\ln y = 0. \tag{3.6}$$

Finally, since this relationship must hold along any portion of the path between δ and δ', the integrand must vanish uniformly. Therefore

$$\frac{dU}{d\ln y} = \frac{\nu RT\chi}{F}\left[\frac{s_+}{n_{e^-}\nu_+} - \frac{z_{e^-}t_+^0}{z_+\nu_+} - \frac{s_0 y}{n_{e^-}(1-\nu y)}\right]. \tag{3.7}$$

Many electrolytes can be treated as 'simple binary electrolytic solutions' [100], for which the six fundamental properties needed to describe isothermal, isobaric mass and charge transport are relatively constant with composition. In this case equation 3.7 can be integrated directly, yielding

$$\Delta U = U^{\delta'} - U^{\delta} = \frac{RT\chi}{F}\left[\frac{\nu}{\nu_+}\left(\frac{s_+}{n_{e^-}} - \frac{z_{e^-}t_+^0}{z_+}\right)\ln\frac{y^{\delta'}}{y^{\delta}} + \frac{s_0}{n_{e^-}}\ln\frac{1-\nu y^{\delta'}}{1-\nu y^{\delta}}\right]. \tag{3.8}$$

Equation 3.8 is the sole expression needed to relate changes in the OCP to solution composition, and serves as the theoretical foundation of the subsequent analysis. It differs from the expression used by Ma *et al.* [21] because χ is determined by the variation in the mean molar salt activity coefficient on a particle-fraction basis, rather than being based on molar concentration.

3.2.3 Concentration cell

During concentration-cell measurements, the cell voltage is recorded while no appreciable mass diffusion is allowed across the transition region in Figure 3.1. Experimental implementations typically involve using a membrane or frit to separate two compartments containing well-stirred electrolytic solutions, in which reference electrodes are immersed. On one side of the cell, solution composition is fixed at $y^{\delta'} = y_{\text{ref}}$; on the other side, a test composition $y^{\delta} = y_{\text{test}}$ is varied in the close vicinity of y_{ref}. The potential difference between the two electrodes is determined by y_{test} and y_{ref}, giving a function $\Delta U(y_{\text{test}}, y_{\text{ref}})$. Plotting this potential difference as a function of the logarithm of the concentration ratio $y_{\text{test}}/y_{\text{ref}}$ yields a curve, whose slope can be

extrapolated to find the value of $dU/d\ln y$ at y_{ref}, denoted formally as $(dU/d\ln y)|_{y_{\text{ref}}}$ [21]. Given the tranference number at y_{ref}, the thermodynamic factor at y_{ref} can be calculated from $(dU/d\ln y)|_{y_{\text{ref}}}$ through equation 3.7, or *vice versa*.

3.2.4 Polarization cell

Restricted diffusion and galvanostatic polarization both involve tracking the relaxation of an initially nonuniform concentration distribution in a cell at open circuit [21, 25, 30]. Both measurements can be implemented with a single chronopotentiometric experiment. An isothermal, isobaric cell is polarized with a constant current at time $t = 0$ for an appropriate period of time t_{pulse} to create a nonuniform concentration profile in the solution. After t_{pulse}, an open-circuit condition is enforced by a galvanostat, which also records the relaxation of the OCP as the concentration profile relaxes.

For a moderately concentrated simple binary electrolyte in a one-dimensional cell of length L in the x direction, the composition distribution during polarization and relaxation is governed by [100]

$$\frac{\partial y}{\partial \tau} + 2\beta I \frac{\partial y}{\partial \xi} = \frac{\partial^2 y}{\partial \xi^2} + \frac{2\alpha}{\langle y\rangle + (\langle y\rangle - y)\,\alpha}\left(\frac{\partial y}{\partial \xi}\right)^2, \tag{3.9}$$

where $\langle y\rangle$ is the equilibrium composition. The dimensionless time τ, position ξ, and current density I are

$$\tau = \frac{\mathscr{D}\chi t}{L}, \quad \xi = \frac{x}{L}, \quad \text{and} \quad I = \frac{i}{i_{\text{L}}^{\infty}}, \tag{3.10}$$

in which the limiting current at infinite dilution, i_{L}^{∞}, is

$$i_{\text{L}}^{\infty} = \frac{2F z_+ \nu_+ \mathscr{D}\chi \langle c\rangle}{\left(\frac{s_+ z_+}{z_{\text{e}^-} n_{\text{e}^-}} - t_+^0\right) L}, \tag{3.11}$$

(The equilibrium molar concentration of salt, $\langle c\rangle$, relates to $\langle y\rangle$ through equation

3.2.) For binary electrolytes, $\mathscr{D}$ and t_+^0 are defined in terms of the Stefan-Maxwell coefficients describing ion-solvent interactions as

$$\mathscr{D} = \frac{(z_+ - z_-)\,\mathscr{D}_{0+}\mathscr{D}_{0-}}{z_+\mathscr{D}_{0+} - z_-\mathscr{D}_{0-}} \quad \text{and} \quad t_+^0 = \frac{z_+\mathscr{D}_{0+}}{z_+\mathscr{D}_{0+} - z_-\mathscr{D}_{0-}}. \tag{3.12}$$

Solute-volume effects, which were assumed to be negligible by Ma *et al.* [21] and Hafezi and Newman [25], are described by the parameters

$$\alpha = \langle c \rangle \left(\nu \overline{V}_0 - \overline{V}_\mathrm{e}\right) \quad \text{and} \quad \beta = \frac{z_+\nu_+ \langle c \rangle \Delta\overline{V}_\mathrm{rxn}^\mathrm{sol}}{z_+ s_+ - z_{\mathrm{e}^-} n_{\mathrm{e}^-} t_+^0}, \tag{3.13}$$

in which $\Delta\overline{V}_\mathrm{rxn}^\mathrm{sol} = \sum_j s_j \overline{V}_j$ represents the solution-phase volume change per mole of limiting reactant as reaction 3.3 goes to completion. Observe that the calculation of β may require knowledge of partial molar volumes for individual ions. Newman and Chapman [30] showed for binary electrolytic solutions that it is natural to assume that ionic partial molar volumes satisfy

$$\bar{V}_+ = \frac{(1 - t_+^0)\,\bar{V}_\mathrm{e}}{\nu_+} \quad \text{and} \quad \bar{V}_- = \frac{t_+^0 \bar{V}_\mathrm{e}}{\nu_-} \tag{3.14}$$

relationships which are generally needed to calculate $\Delta\overline{V}_\mathrm{rxn}^\mathrm{sol}$.

Because of the interfacial half-reaction, governing equation 3.9 is subject to a boundary condition

$$\left.\frac{\partial y}{\partial \xi}\right|_{\tau,0} = -\frac{2\langle y \rangle}{1+\alpha} \times \left\{\left[1 + \left(1 - \frac{y}{\langle y \rangle}\right)\alpha - \frac{y}{\langle y \rangle}\beta\right]\left[1 + \left(1 - \frac{y}{\langle y \rangle}\right)\alpha\right] I\right\}\Bigg|_{\tau,0}, \tag{3.15}$$

which relates the composition gradient at one of the electrodes to the dimensionless current I. To describe the pulse process, current is described by a driving function

$$I(\tau) = \begin{cases} I_\mathrm{pulse}, & \tau \le \tau_\mathrm{pulse} \\ 0, & \tau > \tau_\mathrm{pulse} \end{cases}. \tag{3.16}$$

In addition, an auxiliary condition,

$$\int_0^1 \frac{y}{\langle y \rangle + (\langle y \rangle - y)\,\alpha} d\xi = 1, \tag{3.17}$$

guarantees mass conservation in the solution phase, which is maintained instantaneously as a consequence of the symmetry in the cell half-reactions.

The solution of equation 3.9 subject to the conditions in equations 3.15 through 3.17 describes how a galvanostatic pulse induces concentration polarization. Such a pulse can be used to initiate either restricted diffusion or galvanostatic polarization experiments: short-time chronopotentiometry data during the open-circuit relaxation period relates to the diffusivity and transference number, while long-time relaxation data depends on diffusivity alone.

Even in a system where transient diffusional relaxations occur, equation 3.8 determines the instantaneous relationship between OCP and composition. To describe restricted diffusion and galvanostatic polarization, y^{δ} and $y^{\delta'}$ are taken to be the transient solution compositions in domains immediately adjacent to the the electrode surfaces (*i.e.*, $y^{\delta'} = y(\tau, 0)$ and $y^{\delta} = y(\tau, 1)$), determined by the pulse current and pulse duration.

Galvanostatic-polarization measurements track OCP relaxations associated with diffusion in boundary layers close to the electrodes. The underlying theory relies on data collected before the diffusion boundary layers induced by the current pulse meet – a time domain in which both migration and diffusion control the developing concentration profile. In this regime, the interelectrode distance is unimportant and the solutions near the electrodes can be approximated as semi-infinite domains. Restricted-diffusion measurements track OCP relaxations long after a concentration polarization – a time domain when migration is unimportant and detailed information about the initial distribution of composition is lost. In this situation the timescale

for relaxation depends strongly on the interelectrode distance.

3.2.5 Linearization of potential

Potentiometric restricted-diffusion and galvanostatic-polarization measurements both use OCP as a proxy for the composition difference across the cell. If the magnitude of concentration polarization is sufficiently small, the open-circuit voltage can be linearized about the equilibrium composition within the cell, yielding

$$\Delta U \approx \left.\frac{dU}{dy}\right|_{\langle y\rangle} \Delta y, \quad \text{or} \quad \Delta U \approx \left.\frac{dU}{d\ln y}\right|_{\langle y\rangle} \frac{\Delta y}{\langle y\rangle} \tag{3.18}$$

where $\Delta y = y^{\delta'} - y^{\delta}$. This proportionality between ΔU and Δy has been adopted instead of equation 3.8 in the analyses of many electrolyte-characterization experiments [21, 24, 25, 27, 62, 99, 101, 102]; several groups have employed equation 3.18 when implementing diffusivity and transference-number measurements in particular [24, 62, 101, 102]. The restriction to small Δy can easily be violated in practice, however, because relatively large concentration differences may be needed to achieve a significant voltage signal during a relaxation. In cases where Δy is too large, the measured ΔU actually corresponds to a lower Δy than equation 3.18 predicts. When equation 3.18 is used, potentiometric experiments must be designed to minimize the error induced by the linearization.

3.2.6 Restricted diffusion

To implement a restricted-diffusion measurement, an initially nonuniform concentration distribution is set up and the logarithm of the concentration difference between ends of the cell (or the difference in some other local solution characteristic that is proportional to concentration) is tracked as a function of time. Data gathered at long times are fit with a line, whose slope is proportional to the Fickian diffusivity

$D = \mathscr{D}\chi$.

Although OCP is a logical solution characteristic to track, restricted-diffusion measurements can be performed in a number of ways that do not involve potentiometry. For example, the classic Harned technique for measuring D relies on local DC conductometry to establish the salt concentrations at either end of a restricted-diffusion cell [98]; Newman and colleagues have used both UV/visible spectrophotometry [87] and interferometry [30] in a similar capacity. It has been observed that non-potentiometric techniques yield lower diffusivities than potentiometric ones [87, 103]. This observation is natural in light of the inaccuracy that the approximation in equation 3.18 can induce in data processing. As concentration polarization decreases during the relaxation period, the difference between the real experimental Δy (denoted as Δy_{real}) and Δy obtained from ΔU through equation 3.18 (denoted as Δy_{appr}, which is generally higher than Δy_{real}) gets smaller. The magnitude of the slope of $\ln(\Delta y_{\text{appr}})$ *vs.* time is higher than that of $\ln(\Delta y_{\text{real}})$ *vs.* time, leading to higher apparent electrolyte diffusivity. Nevertheless, the inaccuracy brought by applying equation 3.18 is usually minimal, since the approximation that composition differences are small is often reasonable during relaxations after long times.

3.2.7 Galvanostatic polarization

Data processing for galvanostatic polarization requires precise knowledge of the OCP immediately after the current pulse. When performing galvanostatic-polarization experiments, some capacitive relaxation associated with double-layer relaxation – neglected by the theory – occurs at very short times after the pulse. Thus, researchers have almost exclusively used an extrapolation method [21, 25], in which the OCP during relaxation is recorded as a function of a transformed time variable $\tilde{\tau}$, defined as

$$\tilde{\tau} = \frac{\sqrt{\tau_{\text{pulse}}}}{\sqrt{\tau} + \sqrt{\tau - \tau_{\text{pulse}}}}. \tag{3.19}$$

This time variable is conveniently restricted between 0 and 1, where 0 corresponds to time infinity and 1 to the initial instant of relaxation after $\tau_{\text{pulse}} = Dt_{\text{pulse}}/L^2$. According to the solution of the transient diffusion equation with $\beta = 0$, and assuming the validity of equation 3.18, ΔU should be a linear function of $\tilde{\tau}$, the extrapolation of which gives $\Delta U|_{\tilde{\tau}=1}$, the OCP immediately after the current pulse. In principle, a plot of $\Delta U|_{\tilde{\tau}=1}$ *vs.* $i\sqrt{t}$ should also be linear; its slope M satisfies the formula [21]

$$M = \frac{4\left(1 - t_+^0\right)}{z_+\nu_+ F \langle c\rangle \sqrt{\pi \mathscr{D}\chi}} \left(\frac{dU}{d\ln c}\right)\Bigg|_{\langle c\rangle}, \tag{3.20}$$

where

$$\frac{1}{\langle c\rangle}\left(\frac{dU}{d\ln c}\right)\Bigg|_{\langle c\rangle} = \frac{\left[\overline{V}_0 - \left(\nu\overline{V}_0 - \overline{V}_{\text{e}}\right)\langle y\rangle\right]^2}{\overline{V}_0\langle y\rangle}\left(\frac{dU}{d\ln y}\right)\Bigg|_{\langle y\rangle}. \tag{3.21}$$

Insertion of expressions 3.7 and 3.21 into equation 3.20 gives a relation among the transference number, diffusivity, and thermodynamic factor.

The application of the linearization in equation 3.18 has a great impact on measurements by galvanostatic polarization, which involve setting up steep concentration gradients in boundary layers. Many groups have observed curvature in the ΔU *vs.* $\tilde{\tau}$ data as $\tilde{\tau}$ approaches 1 [25, 27]. The curvature observed in experiments is often observed over much longer time scales than double-layer capacitances can justify [27]. Replacement of the approximation from equation 3.18 with equation 3.8 rationalizes the prior observations of non-capacitive curvature in ΔU *vs.* $\tilde{\tau}$ curves.

Figure 3.2 shows a series of simulated relaxation curves after galvanostatic polarization of 0.85 M lithium hexafluorophosphate ($LiPF_6$) in propylene carbonate (PC), in a planar, symmetric plating/stripping cell of 1 cm length with lithium-metal electrodes. (Both electrode half-reactions are $Li^+ + e^- \rightleftharpoons Li$.) Properties of this solution have been reported by Nishida *et al.* [104] and Stewart *et al.* [86, 105], and are listed in Table 3.1. To implement simulations, a number of pulse currents were used, while pulse time was held constant at $t_{\text{pulse}} = 500$ s. The curves in Figure 3.2(a) show results

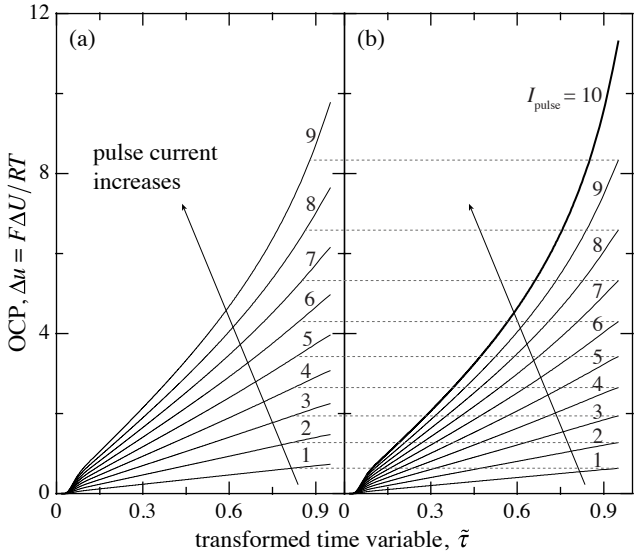

Figure 3.2: Simulated OCP *vs.* $\tilde{\tau}$ curves for 0.85 M $LiPF_6$ in PC subjected to a 500 s current pulse. Curves correspond to pulse currents ranging from I_{pulse} = 1 to I_{pulse} = 10. (a) Response in the absence of solute-volume effects (α = 0, β = 0); (b) Response with α = 0.099 and β = 0.054. Dashed lines illustrate the correspondence between curves with the same pulse currents. The thick black curve in (b) has no corresponding curve in (a) because when solute-volume effects are neglected, Sand's time exceeds 500 s when I_{pulse} = 10.

prop.	value	ref.	prop.	value
κ	0.65 S m^{-1}	[86]	$\mathscr{D}_{+-}$	3.9×10^{-11} m^2 s^{-1}
D	4.0×10^{-10} m^2 s^{-1}	[104]	$\mathscr{D}_{0+}$	1.0×10^{-10} m^2 s^{-1}
t_+^0	0.38	[105]	$\mathscr{D}_{0-}$	1.7×10^{-10} m^2 s^{-1}
$\overline{V}_0$	89.6 cm^3 mol^{-1}	[86]	$\overline{V}_0$	89.6 cm^3 mol^{-1}
$\overline{V}_\mathrm{e}$	62.8 cm^3 mol^{-1}	[86]	$\overline{V}_+$	38.9 cm^3 mol^{-1}
			$\overline{V}_-$	23.9 cm^3 mol^{-1}
$\Delta U\,(0.85\text{ M}, 1.75\text{ M})$	−0.064 V	[105]	χ	3.1

Table 3.1: Properties of 0.85 M $LiPF_6$ in PC. The properties in the left column are reported in the stated references; the properties on the right were calculated from the properties on the left, and were used for simulations. Values of κ and $\mathscr{D}_{+-}$ were not needed for simulations, but are provided for completeness.

in the limit that $\alpha = 0$ and $\beta = 0$, where solute-volume effects are unimportant; Figure 3.2(b) includes the solute-volume effects (discussed in more detail in the next section). At low pulse currents, concentration polarization is relatively low and the relaxation curves are more or less linear, as expected based on the prior theory using equation 3.18. Even when neglecting solute-volume effects, the curves become increasingly nonlinear as pulse current rises, because the concentration polarization is larger at t_{pulse} and equation 3.18 is no longer accurate. Polarizing the solution too much and mistakenly fitting the part of the data near $\tilde{\tau} = 1$ may result in an artificially high M, which, when inserted in equation 3.20 along with correct values of D and $dU/d\ln c$, would produce low transference numbers. This could explain the negative values of t_+^0 observed by Doeff *et al.* [24].

3.2.8 Solute-volume effects

Solute-volume effects, intrinsic in electrolyte transport processes, can be significant in (even moderately) concentrated electrolytes, especially non-aqueous ones [100]. The 'excluded-volume effect' arises from volume redistribution in a polarized cell, and is quantified by α (*cf.* equation 3.13); 'Faradaic convection' occurs when interfacial electrochemical reactions induce bulk flow, and is measured by β (*cf.* equation 3.13). These effects are comparable in importance to the Fickian diffusion process if the associated parameters are near 1. For simple binary electrolytes, Faradaic convection alters the maximum steady-state current tolerance of an electrolytic cell (*i.e.*, its limiting current), and the excluded-volume effect impacts the relationship between concentration polarization and the OCP. Substantial measurement errors can arise when experimental pulse/relaxation data are analyzed with a theory that ignores solute-volume effects.

Currents higher than the limiting current are often desirable for galvanostatic polarization because they induce high concentration polarization over short distances.

In a cell polarized exactly at its limiting current, the concentration of the active species is driven to zero at one of the electrodes only when the cell achieves steady state (after an infinite amount of time). When a higher current is applied, complete consumption of the active species at the electrode surface takes a finite amount of time, known as 'Sand's time' [106–108]. In a solution where solute-volume effects are negligible, Sand's time t_{sand} (or dimensionlessly, τ_{sand}) can be shown to relate to the current through

$$\tau_{\text{sand}}^{\infty} = \frac{Dt_{\text{sand}}^{\infty}}{L^2} = \frac{\pi}{16I^2}. \tag{3.22}$$

This equation is derived by the method reported in Bard and Faulkner's book [83] with $\alpha = 0$ and $\beta = 0$; the relationship here is somewhat extended, however, because Bard and Faulkner neglect migration, assuming a well-supported electrolyte for which $t_+^0 = 0$. The derivation of equation 3.22 assumes a semi-infinite diffusion domain, and its validity is therefore restricted to times before the diffusion boundary layers come into contact.

Equation 3.22 shows that given the same polarization current, a system with a longer Sand's time has a longer pulse tolerance; given the same Sand's time, a system with a larger limiting current can tolerate a higher-current pulse of a given duration.

Although there are a few notable exceptions, Faradaic convection usually increases the current tolerance of electrolytic solutions [100]. For example, Faradaic convection participates in the simulated transport process that gives the OCP *vs.* $\tilde{\tau}$ curves in Figure 3.2(b), but does not in 3.2(a). The highest pulse current adopted in generating Figure 3.2(b) is $I_{\text{pulse}} = 10$ (the thick black curve); in the limit $\alpha, \beta \to 0$, an applied current of this magnitude cannot be sustained, because the specified pulse duration is greater than Sand's time. Generally, solutions with Faradaic convection will have longer Sand's times when $\beta > 0$.

In diffusivity and transference-number measurements, establishing a composition distribution that can be tracked and predicted by equations 3.9 through 3.17 is essen-

tial. The polarization process should be strictly controlled to prevent the complete consumption of a limiting reactant at either electrode – a process that can be guided by Figure 3.3. The black curves in the figure show Sand's time as computed numerically using equations 3.9 through 3.17. Sand's time is presented as a function of the polarization current for solutions with different Faradaic-convection numbers. Unlike equation 3.22, this calculation makes no semi-infinite assumption and accounts for the Faradaic-convection effect. The apparent Sand's time increases when the polarization is close to $I_{\text{pulse}} = 1$, because the boundary layers reach the opposing ends of the cell before the pulse is over; apparent Sand's time also increases with the Faradaic-convection number. Experimental polarization processes for galvanostatic polarization should be implemented to the left of the black curves to ensure well-characterized electrolyte redistribution.

In galvanostatic polarization experiments, only data collected before the concentration boundary layers meet are useful for analysis. As long as there is a concentration gradient, the two boundary layers will propagate towards each other, no matter whether there is an applied current or not. The time it takes for the boundary layers to meet does not depend on the polarization current or time, but solely on the transport characteristics of the solution.

For a pulse/relaxation experiment, designate the time that the concentration boundary layers propagating from the two electrodes meet as τ_{BL}. (This should be counted from the first instant at which current is applied, and therefore includes both the pulse and relaxation times). A conservative practical estimate for this time was chosen to be $\tau_{\text{BL}} = \frac{1}{16}$, which corresponds to a certain transformed time variable $\tilde{\tau}$ through equation 3.19. The shaded contours in Figure 3.3 give the values of $\tilde{\tau}$ at the instant the two boundary layers touch in a certain galvanostatic polarization experiment. Only data between the $\tilde{\tau}$ values indicated by the contours and 1 on an OCP vs. $\tilde{\tau}$ curve should be used for galvanostatic-polarization data analysis.

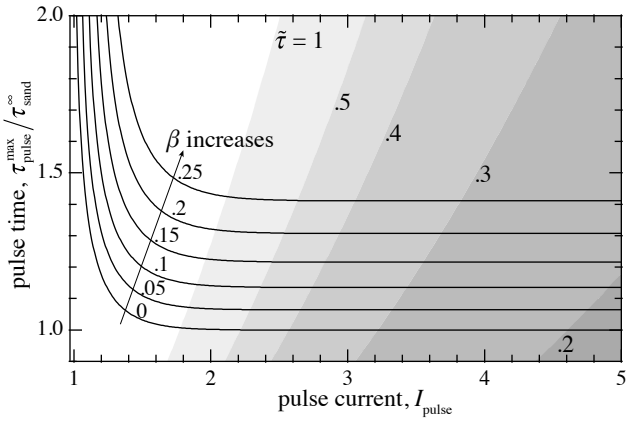

Figure 3.3: A plot to provide guidance for implementing restricted diffusion and galvanostatic polarization experiments using current pulses above the limiting current. The black curves give the longest polarization time (Sand's time) for a given applied pulse current to prevent the active species from depleting at the electrodes. The shaded contours on the plot indicate the value of $\tilde{\tau}$ (the transformed time variable in galvanostatic polarization experiments) for a given experimental setup (*i.e.*, polarization current and time), at which the boundary layers come into contact.

In addition to changing the apparent current tolerance of a solution, solute-volume effects also influence the diffusion potential. The OCP during transient relaxation is lower when solute-volume effects are involved than when they are not, as shown by the horizontal tie lines connecting curves at the same current in Figures 3.2(a) and 3.2(b). In most electrolytic systems of practical interest, solute-volume effects suppress diffusion potential, resulting in lower-than-expected OCP in diffusivity and transference-number measurements. Solute-volume effects are intrinsic in transport processes, and are significant in moderately concentrated non-aqueous solutions. When relying on equation 3.20 to obtain properties, inaccuracies are introduced into the measurement by fitting the OCP vs. $\tilde{\tau}$ data with a model that does not account for solute-volume effects.

3.2.9 Data fitting

Governing equations 3.9 through 3.17 were solved numerically to fit the relaxation OCP *vs.* $\tilde{\tau}$ data gathered by Valøen and Reimers for a 2.24 M $LiPF_6$ solution in a mixed PC/EC/DMC solvent [27], which are reproduced in Figure 3.4. The relaxation data show curvature at the beginning of relaxation ($\tilde{\tau}$ close to 1), when the concentration gradient across the cell is the largest and the assumed proportionality between ΔU and Δy in equation 3.18 is the least accurate. Valøen and Reimers performed an independent concentration-cell measurement to show $dU/d\ln c = 0.11$ at 2.24 M, assumed a cation transference number of 0.38, and then used galvanostatic polarization to get the diffusivity with equation 3.20. By fitting the data between $\tilde{\tau}$ = 0.5 and $\tilde{\tau}$ = 0.8, they concluded that the electrolyte diffusivity was about 1.8×10^{-6} cm^2 s^{-1}. Our simulation based on equations 3.9 through 3.17 fits the entire range of the experimental data well, including the curved part. Since our model accounts for the intrinsic and important existence of the solute-volume effects in such a concentrated non-aqueous solution, the diffusion potential is suppressed. Adopting the transfer-

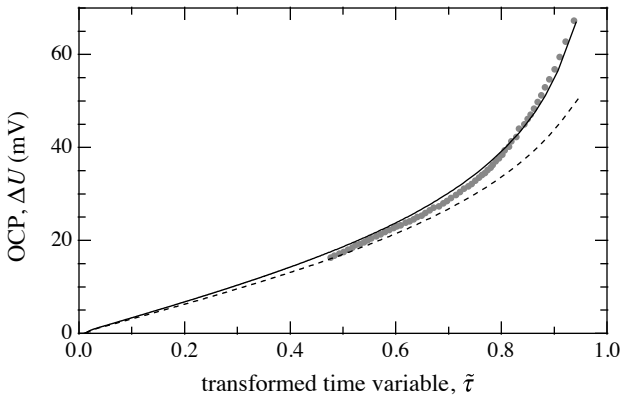

Figure 3.4: Experimental OCP *vs.* $\tilde{\tau}$ relaxation curve (gray dots) and model outputs from equations 3.9 through 3.17. The black solid curve is generated with $D = 1.55 \times 10^{-6}$ cm^2 s^{-1} and $t_+^0 = 0.38$, the black dashed curve with $D = 1.8 \times 10^{-6}$ cm^2 s^{-1} and $t_+^0 = 0.38$.

ence number (t_+^0 = 0.38) and the diffusivity (D = 1.8×10^{-6} cm^2 s^{-1}) used by Valøen and Reimers, our simulation yields a curve that systematically underpredicts their voltages. The data can be matched well if a somewhat lower diffusivity, 1.55×10^{-6} cm^2 s^{-1}, is used for the simulation. (A complete set of properties used for fitting the experimental data is listed in Table 3.2.) Fitting the correct part of the relaxation curves with models that neglect the effects discussed above can be misleading, and result in a low M. When incorporated into equation 3.20, this will result in higher measured diffusivities or transference numbers than expected.

3.3 Conclusion

A detailed analysis of potentiometric restricted-diffusion and galvanostatic-polarization experiments has been performed to address issues in measurements that may lead to inaccurate property determination. The methods for measuring electrolyte thermodynamic factor, diffusivity and transference number in simple binary electrolytic solutions are developed on the basis of a single equation that relates open-circuit potential to solution composition. Using a particle-fraction basis brings mathematical convenience, and helps avoid systematic errors in experiments that may be induced by temperature or pressure fluctuation.

The assumption of a proportionality between the polarization-induced open-circuit potential drop ΔU and the extent of concentration polarization Δy is only accurate when Δy is small. When Δy gets too large, a measured value of ΔU will correspond to an actual Δy lower than the one predicted by the linear approximation. The curvature observed by many research groups in OCP vs. $\tilde{\tau}$ curves from galvanostatic-polarization experiments is caused primarily by inappropriate use of the linear relation between ΔU and Δy, which may result in low – or even negative – transference numbers.

Solute-volume effects lead to other issues in measurements, changing the current

prop.	value	ref.	prop.	value
κ	1.0 S m^{-1}	[27]	$\mathscr{D}_{+-}$	2.1×10^{-11} m^2 s^{-1}
D	1.55×10^{-10} m^2 s^{-1}	◊	$\mathscr{D}_{0+}$	1.8×10^{-10} m^2 s^{-1}
t_+^0	0.38	[27]	$\mathscr{D}_{0-}$	3.0×10^{-10} m^2 s^{-1}
$\overline{V}_0$	78.1 cm^3 mol^{-1}	◊	$\overline{V}_0$	78.1 cm^3 mol^{-1}
$\overline{V}_e$	55.5 cm^3 mol^{-1}	◊	$\overline{V}_+$	34.4 cm^3 mol^{-1}
			$\overline{V}_-$	21.1 cm^3 mol^{-1}
$dU/d\ln c$	0.017 V	[27]	χ	0.68

Table 3.2: Properties of 2.24 M $LiPF_6$ in the mixed PC/EC/DMC solution studied by Valøen and Reimers. Properties in the right column were used for simulations, and were calculated from the properties on the left. Diamonds indicate properties reported for the first time here.

tolerance of electrolytic solutions and also impacting their diffusion potentials. Sand's time was recalculated for electrolytic solutions with different Faradaic-convection numbers, showing the impacts of finite interelectrode distance and reaction-induced convection during the polarization. The galvanostatic polarization experiments should be designed and implemented so that the polarization process lasts no longer than Sand's time, and so that enough data can be collected before diffusion boundary layers come into contact. Neglecting solute-volume effects when analyzing experimental data leads to inaccurate measurement of transport properties; the data may seem characteristic of an electrolyte with elevated diffusivity or transference number.

CHAPTER IV

Capacity-Limiting Factors in Li/O_2 Batteries

4.1 Introduction

The extremely high theoretical energy density obtained by reacting metallic lithium with gaseous oxygen suggests that rechargeable Li/O_2 batteries could compete with combustion-based propulsion systems [109], an observation that has bolstered significant research interest as the demand for electric and hybrid-electric vehicles continues to grow [110–124]. A reversible non-aqueous (aprotic) rechargeable Li/O_2 battery was first proposed by Abraham and Zhang [3], who demonstrated that a cell based on the half-reactions

$$Li^+ + e^- \rightleftharpoons Li \tag{4.1}$$

at the negative electrode and

$$2Li^+ + O_2 + e^- \rightleftharpoons Li_2O_2 \tag{4.2}$$

at the positive electrode could be realized. The associated cell reaction provides an equilibrium open-circuit potential $U^{\ominus}$ around 3 V [3, 6, 125], usually implemented in a planar device comprising a metallic lithium negative electrode, a separator permeated by a non-aqueous lithium-conductive electrolyte, and a porous, electronically conductive, electrolyte-saturated positive electrode that is exposed to ambient oxygen

gas. The desired basic chemistry of the aprotic Li/O_2 cell is now well accepted, and many recent studies have provided insight into the details of the positive-electrode reaction mechanism and its reversibility [50, 125–138].

A number of barriers must be overcome before Li/O_2 technology can be put to practical use [6, 139–142]. One problem is the 'sudden death' of the cell voltage during the discharge process, which occurs far below the theoretical maximum energy capacity and has been observed by many research groups [3, 143–150].

Numerous research efforts have been dedicated to elucidating the sudden-death phenomenon. Scholars divide primarily into two camps: one group suggests that the insulating nature of the lithium peroxide (Li_2O_2) layer that deposits during discharge causes a barrier to electron transport after its dimensions reach certain thresholds, limiting capacity by constraining the discharge-product layer thickness [118–120, 132, 151–153]; the other group contends that the low permeability of dissolved oxygen in porous and tortuous positive electrodes causes it to be depleted within the cell, limiting capacity by reducing utilization of the positive electrode's available pore volume [50, 126, 154–157].

A main challenge confronted in Li/O_2 cell modeling is that deposition of insoluble discharge products on pore walls causes microstructural changes in the porous cathode as discharge progresses. In principle, discharge-product growth may shrink (or even block) pores in the electrode, displace liquid electrolyte, and alter the surface area available for charge transfer; the discharge-product layer itself may incur resistances to charge exchange (either by conducting or tunneling mechanisms) or material transport.

Neidhardt *et al.* extended the porous-electrode theory, providing a macrohomogeneous approach that allows the simulation of spatial domains comprising more than two phases [158]. They provided a general method by which possible morphology changes in porous electrodes can be associated with the formation of insoluble

discharge products. The present chapter implements Neidhardt *et al.*'s formalism in the description of the porous positive electrode of an Li/O_2 cell, accounting for three distinct phases within it, and allowing possible charge-exchange processes at discharge-product/electrolyte interfaces or electrolyte/solid interfaces. The proposed model is designed with the aim of providing sufficient flexibility to account for many of the discharge-product growth mechanisms hypothesized in the literature.

Simulation results are presented to illustrate the effects that three hypothetical positive-electrode-reaction mechanisms and discharge-product morphologies have on the voltage response during Li/O_2 cell discharge. In one case, heterogeneous kinetics is assumed to occur at the substrate/electrolyte interface, so that the growth of the product is controlled by material diffusion through the porous discharge-product layer. In two other cases, heterogeneous kinetics is assumed to occur at the discharge-product/electrolyte interface, so that the electronic resistance of the discharge-product phase limits its growth. Both compact and porous discharge-product-phase morphologies are considered in the latter two cases where electronic resistance restricts product growth.

Experiments in the superficial current-density range of 0.1 to 1.0 mA cm^{-2} agree with simulations that assume oxygen transport to be rate limiting, in the sense that when the model is parameterized with properties known from literature, it predicts discharge-voltage curves that agree qualitatively with experiments and also quantitatively match the experimentally measured dependence of cell capacity on discharge rate. For simulations to match the experimental discharge curves, the electrical resistivity of the discharge-product phase must be several orders of magnitude lower than the resistivity of a bulk insulator. When a compact discharge-product layer through which electron tunneling occurs was modeled, cell capacities were found to be significantly lower than the capacities measured in cells with porous positive electrodes.

4.2 Model development

4.2.1 Cell geometry and ambient conditions

Table 4.1 presents the full set of model equations used to describe discharge of a one-dimensional planar cell under isothermal, isobaric conditions. The distributions of materials and potential are resolved throughout the liquid-saturated-separator and porous-positive-electrode domains, which are taken to have finite thicknesses of L_{sep} and L_+, respectively. Since the negative-electrode reaction occurs at a plane surface normal to the position coordinate x, it is described in the model through a boundary condition at $x = 0$. Transport processes in the gas phase are not considered explicitly: the liquid surface at the electrode-gas interface ($x = L_{\text{sep}} + L_+$) is taken to be in equilibrium with the adjacent O_2 gas, which is assumed to be stagnant and at constant pressure p. This pressure does not appear directly in the model, but presumably affects the saturated oxygen concentration of the liquid, $c_{O_2}^{\text{sat}}$. (The experiments modeled here used pure O_2 gas at a gauge pressure of 1 bar.) The absolute temperature T is also assumed to be constant and uniform throughout the cell.

4.2.2 Liquid and solid phases

The physical description of the liquid phase—both within the separator and in the electrolyte that occupies free volume in the porous electrode—is presented in a general form that allows for an arbitrary number n of ionic or molecular constituents to be included if necessary. Multicomponent transport in the liquid is taken to follow Onsager-Stefan-Maxwell constitutive laws, which establish how the electrochemical-potential gradient of species k, $d\mu_k/dx$, relates to the differences between its molar flux, N_k, and the fluxes of all other species j through drag coefficients involving the Stefan-Maxwell diffusivities $\mathscr{D}_{kj}$, the local composition y_k, and the universal gas constant R. Molecular diffusion and charge migration are distinguished by incor-

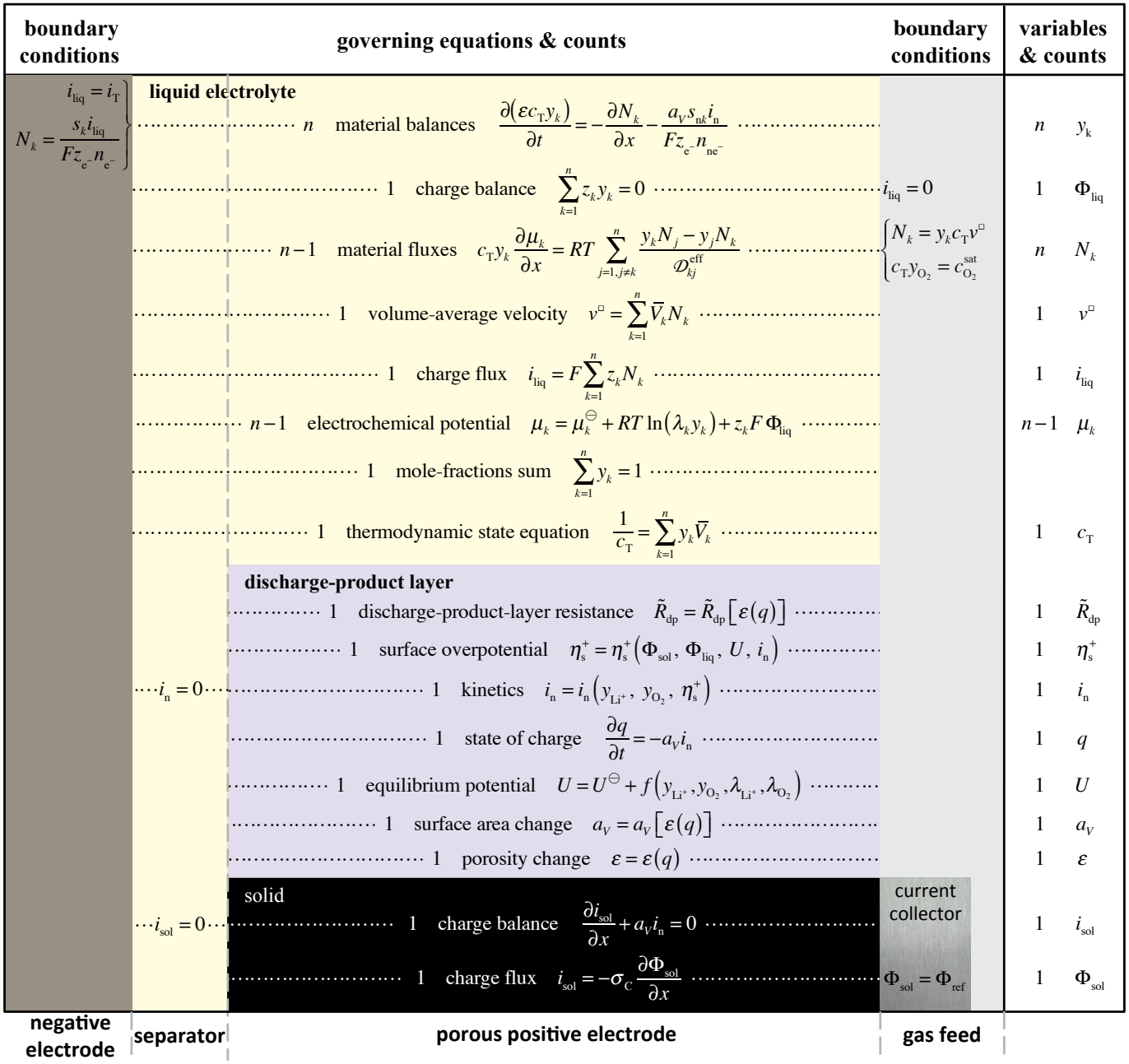

Table 4.1: General structure of the one-dimensional Li/O_2 cell model, listing the governing equations that hold at interior points and the boundary conditions associated with each differential equation. The positive electrode contains pore-filling liquid (yellow background), solid (black background), and discharge-product (purple background) phases. The counts of the equations and dependent variables are provided to illustrate model closure: $3n + 12$ equations and unknowns are needed if there are n liquid-phase constituents.

porating constitutive equations that cast μ_k in terms of species mole fractions y_k (whose gradients drive diffusion) and a liquid-phase quasi-electrostatic potential Φ_{liq} (whose gradient drives migration of charged species). Although thermodynamic factors λ_k were included to allow for solution nonideality if needed, nonideality was found to have a minimal impact on results when reasonable values of activity coefficients [62] were used. For simplicity, results presented here are computed under the ideal-electrolyte assumption that $\lambda_k = 1$ for every species. Previous efforts to simulate Li/O_2 batteries [50, 154, 158] have mostly adopted the transport equations developed by Doyle, Fuller, and Newman, based on the concentrated-solution theory for binary electrolytes [35, 36], and appended a separate flux law for oxygen. The basis in Onsager-Stefan-Maxwell transport theory distinguishes the present model.

Simulations were performed for comparison with the experiments of Griffith *et al.* [159], which employed a four-species electrolyte ($n = 4$), comprising a single solvent (dimethoxyethane, or DME), dissolved Li^+, bis-(trifluoromethanesulfonyl)imide ($TFSI^-$) anions and O_2. The Onsager-Stefan-Maxwell framework allows for the possibility of ion/oxygen diffusional interactions, which could lead to electro-osmosis of oxygen, as well as salt flux induced by oxygen gradients, although these phenomena are neglected for now. Three (*i.e.*, $n - 1$) independent flux laws are written to describe solvent, dissolved O_2, and Li^+; a fourth law, governing the electrochemical potential of $TFSI^-$, is omitted from the model presented in Table 4.1 because it can be shown to depend on the others through the Gibbs-Duhem equation and kinematic considerations.

Faraday 's law is adopted to express the liquid-phase ionic current i_{liq} in terms of the molar fluxes and the species equivalent charges z_k. As is typical when simulating volume elements that are large in comparison to the Debye length, an assumption of local electroneutrality is adopted throughout the liquid phase.

Another unique aspect of the model in Table 4.1 is that it accounts rigorously

for the changes in liquid volume that accompany concentration polarization during the discharge process. To ensure a proper balance of volume, a variable was introduced to quantify the volume-average solution velocity $v^{\square}$ induced by species fluxes, and the standard thermodynamic constitutive laws from concentrated-solution theory [10, 28–32] were augmented with a local volume-explicit equation of state. The state equation locally enforces the known dependence of total molar solution concentration c_{T} on composition through species partial molar volumes $\overline{V}_k$. Note that these considerations provide rigor, but also restrict the model to one-dimensional simulations; for simulations of higher-dimensional cell geometries a momentum balance must be appended to the equation system to ensure closure [100].

Standard material balances describe the liquid electrolyte in the separator domain. As contemporary air-battery research efforts typically employ separators comprising an inert porous matrix such as Celgard [156, 160–164] or glass fiber [133, 165–167] permeated by liquid electrolyte, these balances also include the free volume available for liquid, which generally differs between the separator ($\varepsilon_{\mathrm{sep}}$) and the positive electrode (ε). (Glass-fiber separators were used to gather the experimental data modeled here.) Diffusivities corrected according to the Bruggeman correlation [32, 168]

$$\mathscr{D}_{kj}^{\mathrm{eff}} = \varepsilon^{1.5}\mathscr{D}_{kj} \tag{4.3}$$

are also adopted, to account for dispersion induced by the porosity and tortuosity of porous structures.

To describe electron transport in the porous solid, a charge-continuity equation is included, as in the porous-electrode theory developed by Newman and colleagues [10, 32, 35, 36]. Charge flux in the solid is described by Ohm's law, which relates the electronic current density i_{sol} to the spatial variation of solid-phase potential Φ_{sol}. The charge balance contains a generation term proportional to the reaction-current

density i_{n}, which is associated with local production or consumption of electrons by half-reaction 4.2 at reactive surfaces within the porous electrode. By Newman's convention, anodic reaction currents are defined to be positive. Since i_{n} parameterizes a heterogeneous process, it is naturally expressed per unit of surface area available for electron exchange; in balance equations, multiplication by a surface-to-volume ratio a_V thus converts i_{n} to a rate of anodic charge transfer per unit porous-electrode volume. An equation is also included to define a variable that measures the local volumetric extent of discharge q, whose rate of change with respect to time is $-i_{\mathrm{n}}a_V$.

When describing the electrode-permeating part of the liquid phase, complementary generation terms are incorporated into the species balances to account for consumption or production of liquid constituents by electrochemical half-reactions in the solid positive electrode. Again following typical practice from porous-electrode theory, these terms are taken to be proportional to the local value of $i_{\mathrm{n}}a_V$ through stoichiometric coefficients $s_{\mathrm{n}k}$ and the number of electrons involved in the positive-electrode half-reaction, $n_{\mathrm{ne^-}}$, as well as Faraday's constant F. Note that this general structure provides some flexibility in the treatment of reaction mechanisms involving multiple species (or intermediates). For the present analysis, reactions 4.1 and 4.2 were used, and assumed to be elementary.

In addition to the use of the Onsager-Stefan-Maxwell transport model and the incorporation of a local volumetric equation of state for the liquid, it should be noted that two other features suggested by Neidhardt *et al.* [158] differentiate the present model from most multiphysics air-battery models. First, the free porosity in the positive electrode, ε, is allowed to vary as a function of position (or local values of state variables) within it. Second, the surface-to-volume ratio a_V available for charge exchange between the liquid and discharge-product phase may similarly vary. Different hypotheses about discharge-product morphology and the discharge pathway for half-reaction 4.2 can be expressed by choosing different dependences of ε and a_V

on q.

4.2.3 Boundary and initial conditions

The simulations performed here describe galvanostatic discharge at total current density i_{T}. At the negative electrode/separator interface (position $x = 0$), this total current is carried by charged species in the electrolyte. Also, all the material fluxes at this interface are proportional to the total current through the stoichiometry of interfacial half-reaction 4.1. At the opposing current collector ($x = L_{\mathrm{sep}} + L_{+}$), all the current enters through the porous-solid phase. The molar concentration of O_2 in the liquid is also taken to be saturated at the liquid/gas boundary.

In addition to diffusion and migration, there is also convection of electrolyte in the cell. This convection comes from two sources: the occlusion of pores by discharge product [124] and liquid-phase flow arising from concentration polarization or reaction-induced convection [100]. Efflux of liquid constituents due to discharge-product displacement and solute-volume effects in the liquid is associated with the volume-average velocity at the electrode/gas interface.

4.2.4 Cell potential

During the discharge process, a Li/O_2 cell expends free energy on a number of internal processes. If one considers a thermodynamic path from the negative-electrode interface ($x = 0$), through the liquid phase to the interface with the current collector ($x = L_{\mathrm{sep}} + L_{+}$), across the discharge-product phase at that location, and through the discharge-product/solid surface, then one recognizes four distinct sources of potential loss: kinetic overpotential associated with half-reaction 4.1 at the negative electrode, η_{s}^{-}; loss due to liquid-phase transport, ΔV_{liq}; kinetic overpotential associated with half-reaction 4.2 at the positive electrode, η_{s}^{+}; and possibly an ohmic potential drop associated with the areal resistance (denoted as $\tilde{R}_{\mathrm{dp}}$) of the discharge-product layer,

$i_{\mathrm{n}}\tilde{R}_{\mathrm{dp}}$. The total cell potential, V, is thus expressed as

$$V = U^{\ominus} - \eta_{\mathrm{s}}^{-}|_{0} - \Delta V_{\mathrm{liq}} + \eta_{\mathrm{s}}^{+}|_{L_{\mathrm{sep}}+L_{+}} + \left(i_{\mathrm{n}}\tilde{R}_{\mathrm{dp}}\right)\Big|_{L_{\mathrm{sep}}+L_{+}}, \tag{4.4}$$

where $U^{\ominus}$ is the open-circuit potential of the cell at its equilibrium composition and charge state. Here the kinetic surface overpotential η_{s}^{+} is written as a reduction potential, so that i_{n} is a cathodic current. In a discharge process, the last two terms on the right-hand side of the above equation are both negative in value, contributing to the total potential loss in the battery system. Assuming that the potential is measured by a reference electrode reversible only to lithium cations, the liquid-phase transport loss, which includes both the ohmic drop and diffusion potential, is related to the difference in cation electrochemical potential across the liquid phase:

$$\Delta V_{\mathrm{liq}} = F\left(\mu_{\mathrm{Li^+}}|_{0} - \mu_{\mathrm{Li^+}}|_{L_{\mathrm{sep}}+L_{+}}\right). \tag{4.5}$$

Note that equation 4.4 can also be used to calculate the cell potential in a recharge process; in that case the potential losses naturally 'flip sign', becoming gains above $U^{\ominus}$.

4.2.5 Electron-transfer kinetics

The mechanisms of half-reactions 4.1 and 4.2 are taken to be elementary, following Butler-Volmer kinetics. For reaction 4.2, the species activities a_i are involved in prefactors of the anodic and cathodic terms:

$$\frac{i_{\mathrm{n}}}{i^{*}} = \left(\frac{a_{\mathrm{Li^+}}}{a_{\mathrm{Li^+}}^{\mathrm{ref}}}\right)^{-s_{\mathrm{Li^+}}}\left(\frac{a_{\mathrm{O_2}}}{a_{\mathrm{O_2}}^{\mathrm{ref}}}\right)^{-s_{\mathrm{O_2}}}\exp\left[\frac{(1-\beta)\,n_{\mathrm{e^-}}F\eta_{\mathrm{s}}^{+}}{RT}\right] - \left(\frac{a_{\mathrm{Li_2O_2}}}{a_{\mathrm{Li_2O_2}}^{\mathrm{ref}}}\right)^{s_{\mathrm{Li_2O_2}}}\exp\left(-\frac{\beta n_{\mathrm{e^-}}F\eta_{\mathrm{s}}^{+}}{RT}\right). \tag{4.6}$$

Here i^{*} is the exchange-current density, β the symmetry factor, $s_{\mathrm{Li^+}} = -2$, $s_{\mathrm{O_2}} = -1$ and $s_{\mathrm{Li_2O_2}} = 1$ the stoichiometric coefficients in reaction 4.2 (for a general half-reaction

expressed as a reduction, s_j is positive for products and negative for reactants); a_j^{ref} represents the reference activity of species j (*i.e.*, the activity at the composition where i^* and $U^{\ominus}$ are experimentally measured). Note that since the Li_2O_2 forms a separate solid, its activity was taken to be 1 at all times. The term was left in equation 4.6 because particle structure or surface energy may contribute to differences in the activity of the solid phase that forms—a consideration that may be useful for future modeling efforts.

4.2.6 Material properties

Table 4.2 lists all the property values used for simulations, alongside their sources [5, 62, 152, 154, 169–171]. Mechanical characteristics of the cell, such as the separator and electrode thicknesses and porosities, are chosen to match the experimental setup of Griffith *et al.* [159]. A wetting measurement implemented by Griffith gives an accessible positive-electrode porosity of about 0.7, although the manufacturer reports a porosity of 0.8.

Stefan-Maxwell diffusion coefficients were calculated from literature values using the conversion formulas provided by Newman and Thomas-Alyea [32]. In the calculations, dissolved O_2 was taken to interact only with solvent, *i.e.*, $1/\mathscr{D}_{+O_2} = 1/\mathscr{D}_{-O_2} = 0$ s m^{-2}, and to occupy no partial molar volume. These assumptions are likely reasonable since the saturated oxygen concentration is so low; neglect of ion/solvent interactions is consistent with other multiphysics discharge models [50, 124, 172, 173].

Exchange-current densities at both the negative and positive electrodes are estimates, but their orders of magnitude are comparable to values reported in other studies [114, 152]. For simplicity, the symmetry factors for both half-reactions were taken to be 0.5.

prop.	value	ref.	prop.	value	ref.
electrolyte			**discharge-product layer**		
$\mathscr{D}_{0+}$	4.96×10^{-10} m^2 s^{-1}	[116]	i^*	100 nA m^{-2}	[152]
$\mathscr{D}_{0-}$	6.57×10^{-10} m^2 s^{-1}	[116]	β	0.5	
$\mathscr{D}_{0\mathrm{O_2}}$	1.80×10^{-9} m^2 s^{-1}	[154]	$\overline{V}_{\mathrm{Li_2O_2}}$	19.9 cm^3 mol^{-1}	[5]
$\mathscr{D}_{+-}$	2.89×10^{-11} m^2 s^{-1}	[62]	**separator & solid backbone**		
$\mathscr{D}_{+\mathrm{O_2}}$	∞		L_+	235 µm	♢
$\mathscr{D}_{-\mathrm{O_2}}$	∞		a_{V0}	4.7 µm^{-1}	♢
$c^{\mathrm{sat}}_{\mathrm{O_2}}$	3.5 mM	[154]	ε_0	0.7	♢
$\overline{V}_0$	104.3 cm^3 mol^{-1}	[5]	σ_{C}	1 S mm^{-1}	[171]
$\overline{V}_{\mathrm{e}}$	21.0 cm^3 mol^{-1}	[170]	L_{sep}	650 µm	♢
$\overline{V}_{\mathrm{O_2}}$	0 cm^3 mol^{-1}		$\varepsilon_{\mathrm{sep}}$	0.5	♢

Table 4.2: Material properties used in the simulation. Diamonds in the reference column indicate values provided by suppliers.

4.3 Reaction mechanisms

Three distinct reaction mechanisms are studied here, which are depicted schematically in Figure 4.1. Although Li_2O_2-formation reaction 4.2 was taken to be elementary in all cases, the mechanisms account for different discharge-product morphologies and various sites for electron exchange.

4.3.1 Mechanism I

Discharge-product growth is controlled by electron exchange at the product/solid interface. The Li_2O_2 layer is not compact, *i.e.*, it may be permeated by liquid electrolyte ($\varepsilon_{\mathrm{dp}} \neq 0$). Current exchanged between the liquid phase and the solid backbone is carried by ion transport through the layer, and the electron exchange described by half-reaction 4.2 occurs at the solid surface. Ion transfer is taken to be fast on the basis that the discharge-product layer is thin, so that concentration gradients across the layer are minimal.

Since the electron-transfer site is on the solid surface, the area associated with electron exchange does not change as discharge progresses,

$$a_V(q) = a_{V0}, \tag{4.7}$$

where a_{V0} indicates the original surface-to-volume ratio of the pristine porous electrode. No electron transfer through the product layer occurs, so the overpotential driving half-reaction 4.2 is

$$\eta_{\mathrm{s}}^{+} = \Phi_{\mathrm{sol}} - \Phi_{\mathrm{liq}} - U^{\ominus}, \tag{4.8}$$

with no term for Ohmic loss.

4.3.2 Mechanism II

Discharge-product growth is controlled by electron exchange at the liquid/discharge-

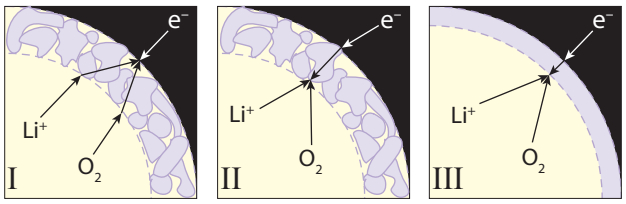

Figure 4.1: Three reaction mechanisms. The figures show a volume element in the positive electrode, containing three phases: liquid electrolyte (yellow); solid backbone (black) and the discharge-product layer (bounded by purple dashed lines). Discharge-product morphologies, charge carriers, and electron-transfer sites differ among the three mechanisms.

product interface. The discharge-product layer is not compact ($\varepsilon_{\mathrm{dp}} \neq 0$), but electron propagation through the discharge-product layer (either through bulk conduction, across surfaces, or *via* defects) supports electrochemical Li_2O_2 formation away from the native porous-electrode surface.

As the free volume in the electrode changes, the surface area available for material exchange with free liquid may change as well. Assuming relatively regular pore geometry, one can establish relationships between a_V and ε by assuming simple geometries for the native pore structure and the structure of the discharge-product layer covering the pore walls. Here, the free volume is taken to exist within cylindrical pores, and the product is assumed to grow inward from the solid surface. Thus the surface area of the free-volume/discharge-product interface shrinks through

$$a_V(q) = a_{V0}\sqrt{\frac{\varepsilon(q)}{\varepsilon_0}}. \tag{4.9}$$

Note that other substrate geometries, such as aggregates of spherical balls [174] or connected spherical cavities [154], have been discussed as representative pore structures. Depending on the geometric assumptions, a_V can increase or decrease with a number of different dependences on ε (or q) as discharge progresses. Simulations were performed using several geometries, but the computed discharge curves and total capacities did not differ significantly, suggesting that the effects of substrate geometry are of second order.

The overpotential that drives product formation in this case is

$$\eta_{\mathrm{s}}^{+} = \Phi_{\mathrm{sol}} - \Phi_{\mathrm{liq}} - U^{\ominus} - i_{\mathrm{n}}\tilde{R}_{\mathrm{dp}}. \tag{4.10}$$

The calculation of the areal resistance $\tilde{R}_{\mathrm{dp}}$ also depends on the assumed pore geometry. Assuming charge transport in the radial direction through a cylindrical annulus,

the areal resistance is

$$\tilde{R}_{\mathrm{dp}} = \frac{\rho_{\mathrm{dp}}}{a_{V0}} \sqrt{\varepsilon_0 \varepsilon} \, \ln\left(\frac{\varepsilon_0}{\varepsilon}\right), \tag{4.11}$$

where ρ_{dp} represents the effective discharge-product-layer resistivity.

4.3.3 Mechanism III

Discharge-product growth is controlled by tunneling of electrons through a compact discharge-product film. In this mechanism, the Li_2O_2 layer grows with no porosity ($\varepsilon_{\mathrm{dp}} = 0$), as suggested by Viswanathan and colleagues, but the discharge-product grows electrochemically [120], occuring *via* electron tunneling through the dense film. Similar to mechanism II, the electrode reaction occurs at the liquid/discharge-product interface, whose area varies according to equation 4.9, and surface overpotential must include an ohmic potential drop across the discharge-product layer, described by equations 4.10 and 4.11.

Viswanathan *et al.* investigated charge transport through dense Li_2O_2 with a metal-insulator-metal (MIM) model, and reported the resistivity of the layer as a function of its thickness. The resistivity rises exponentially with the thickness; an empirical expression

$$\frac{\rho_{\mathrm{dp}}}{1\ \Omega\ \mathrm{m}} = 4 \times 10^{-8} \sinh\left(\frac{6.5d}{1\ \mathrm{nm}}\right) \tag{4.12}$$

fits the data given by Viswanathan well, and is incorporated into equation 4.11 for simulations.

4.3.4 Maximum capacity

For all three mechanisms, there is a maximum amount of discharge product, $c^{\max}_{\mathrm{Li_2O_2}}$, that a given region of the electrode can hold due to the volume restriction. In mechanisms I and II, this maximum amount is determined by total local pore volume and discharge-product compactness; when the discharge-product layer fills pores, the in-

terfacial reaction can no longer occur due to thermodynamic restrictions. As discharge progresses, the electrode porosity decreases. If a Li/O_2 cell is designed well enough to completely utilize the electrode, then the maximum amount of a non-compact discharge product is

$$c^{\max}_{Li_2O_2} = \frac{\varepsilon_0 \left(1 - \varepsilon_{dp}\right)}{s_{Li_2O_2} \overline{V}_{Li_2O_2}}. \tag{4.13}$$

In mechanism III, $c^{\max}_{Li_2O_2}$ is restricted by the maximum thickness of the discharge-product layer, $d_{\max}$, through which electrons can propagate,

$$c^{\max}_{Li_2O_2} = \frac{1 - \left(d_{\max} a_{V0} / 2\varepsilon_0\right)^2}{s_{Li_2O_2} \overline{V}_{Li_2O_2}}. \tag{4.14}$$

Equation 4.14 assumes that the pores are cylindrical annulus; other geometries give slightly different expressions. The electrode reaction will cease in regions where electrons are isolated from the dissolved active species by the discharge-product layer. This condition can be understood formally as a state where the ohmic drop across the discharge-product film for a given rate of current exchange exceeds the kinetic overpotential needed to achieve the same current.

4.4 Results and discussion

4.4.1 Mechanism validation

The model was validated by comparison to the experimental first-discharge curves produced by Griffith *et al.*, which were gathered at a variety of rates ranging from 0.1 to 1.0 mA cm^{-2} [159]. Figure 4.2 illustrates simulation results using mechanism I, alongside the experimental discharge curves. The simulations successfully reproduce the initial relaxation of voltage, as well as the typical voltage-plateau-followed-by-sudden-death behavior seen in experiments [3, 143–150]. In addition to the qualitative agreement with the shapes of typical discharge curves, the simulations quan-

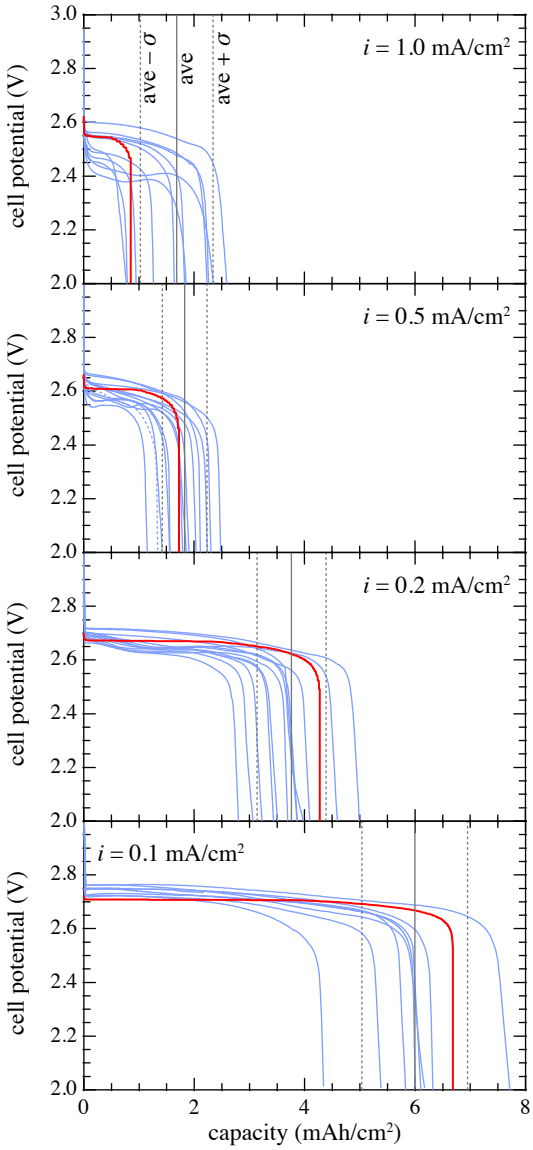

Figure 4.2: Experimental capacity *vs.* rate data are consistent with discharge mechanism I. Comparison of experimental (blue) and theoretical discharge curves produced using mechanism I (red) at different rates. The vertical solid lines indicate the experimental mean cell capacity; vertical dotted lines indicate ±1 standard deviation in the experimental capacity.

titatively match the cell capacities at various discharge rates fairly well, supporting possible validity of the mechanism.

Discharge curves produced at four different discharge rates from all three mechanisms are compared in Figure 4.3. The parameters used to produce Figure 4.2 are used as the baseline parameter set in Figure 4.3. For mechanism II, two resistivities of the discharge-product layer are examined. A resistivity of 10^8 Ω cm (at the border of the insulator regime and semiconductor regime) or lower yields discharge curves similar to those produced by mechanism I, matching the cell capacity and reproducing the sudden-death feature. When a higher resistivity is adopted, the qualitative appearances of the simulated discharge curves differ significantly from the experimental results. Ohmic potential loss across the discharge-product layer rises rapidly as the product layer thickens, eliminating the voltage plateau, suppressing the sudden-death behavior, and lowering the total cell capacity. These results show that mechanism II could be consistent, but only if the effective electronic resistance of the discharge-product layer is several orders of magnitude lower than what would be expected for bulk Li_2O_2.

With mechanism III, the discharge curves retain the voltage plateau and sudden-death features, but the cell capacities are far lower than those observed in the experiments. Electrons tunneling through the Li_2O_2 layer manifest a very low resistivity of the layer when it is thin (less than about 6 nm according to Viswanathan *et al.* [120]), but the exponential growth of resistivity with the layer thickness prevents discharge after the layer gets thicker than the threshold. Since the kinetic parameters for the 'tunneling mechanism' have been confirmed by both theory and experiment [120], the inability to match experimental cell capacities suggests that tunneling does not control capacity in the system studied by Griffith *et al.* [159].

Putting all three mechanisms together, one may safely conclude that resistivity of the discharge-product layer does not limit the cell capacity of Li/O_2 cells. In fact, this

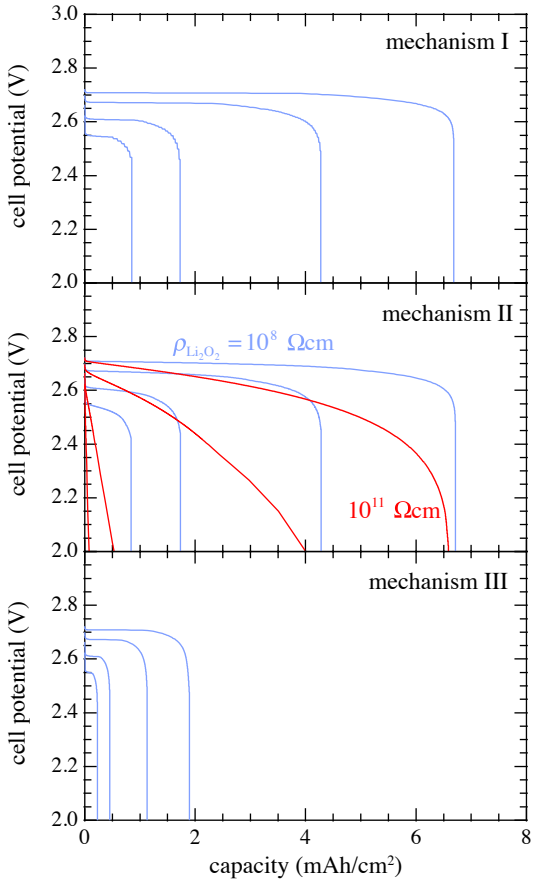

Figure 4.3: Discharge curves generated with all three mechanisms at discharge rates of 0.1, 0.2, 0.5 and 1.0 mA cm^{-2}. The end-of-discharge cell capacities decrease with rising rates for all mechanisms. Two Li_2O_2 resistivities are used in simulations with mechanism II—an insulator resistivity (10^{11} Ω cm) gives much higher overpotential than expected, while a semiconductor resistivity (10^8 Ω cm) reproduces the sudden-death feature.

layer must not contribute significantly to the total overpotential if discharge curves exhibit voltage-plateau and sudden-death features, since tunneling cannot account for cell capacities that match experimental observations.

4.4.2 Overpotential

To understand the sources of sudden death, overpotential breakdowns are shown in Figure 4.4, in which potential losses are expressed as fractions of the total overpotential as discharge progresses. As explained in section 'cell potential', there are four sources of potential loss in a Li/O_2 battery. For all three reaction mechanisms, potential losses due to negative-electrode kinetics and liquid-phase transport contribute about 2% to the total overpotential, and they decrease as discharge progresses. Positive-electrode kinetic overpotential is one main source of potential loss, and ohmic drop across the Li_2O_2 layer is another if the resistivity of the layer is (or becomes) high.

In situations where ohmic potential drop takes up to 60% of the total loss, this potential loss dramatically brings down the cell potential (Figure 4.3), preventing the discharge curve from having a plateau, or causing cell sudden death at a much earlier stage of discharge. This observation further suggests that electron transport through the discharge-product layer is not likely to be a capacity-limiting factor in Li/O_2 batteries that exhibit a voltage plateau on discharge. It could be that electrons can conveniently propagate on the surface of the Li_2O_2 particles in the deposition layer and cause insignificant ohmic potential drop across the layer, as suggested by Radin *et al.* [175], in which case mechanism II is valid. It is also possible that cathode reaction always occurs at the discharge-product/solid-backbone interface, and electrons do not need to transport through the layer at all, in which case mechanism I predicts what happens.

Higher exchange current density i^* and larger surface area available for reaction

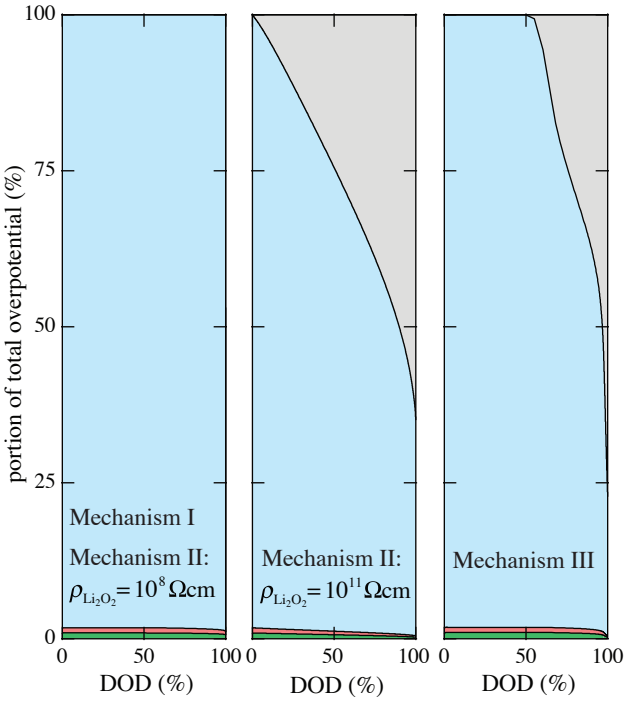

Figure 4.4: Overpotential breakdown ($i_T = 0.1$ mA cm^2) for all three mechanisms. On the plots, green represents potential loss due to electrolyte transport, red is loss due to negative-electrode kinetic, blue stands for loss due to positive-electrode kinetics, and gray indicates ohmic potential loss across the discharge-product layer. Like in Figure 4.3, two Li_2O_2 resistivities are used in mechanism II. A resistivity of 10^8 Ω cm gives an overpotential breakdown very similar to that obtained with mechanism I (showing the two data together), while the overpotential breakdown calculated with a resistivity of 10^{11} Ω cm exhibits much ohmic potential drop across the discharge-product layer.

a_V lead to faster electrode kinetics and thus lower kinetic overpotential. Simulation results show that increasing i^* or a_V can reduce the kinetic overpotential, but changes in i^* or a_V do not affect cell capacity at all. That is to say, catalysts that accelerate the electrode reaction can raise the energy efficiency of a Li/O_2 cell, but will not improve the energy capacity.

4.4.3 Capacity-limiting factors

Lu *et al.* recorded the discharge curves of Li/O_2 single cells at a series of rates [116]; Adams *et al.* reported the overall discharge capacity as a function of current density for Li/O_2 cells, and observed a sudden drop in capacity as discharge rates increased [176]; Griffith *et al.* put the capacity *vs.* rate data on a log-log scale, and obtained a Peukert's slope of about 1.6 [159]. To rationalize these observations and summarize the data, Figure 4.5 puts all the above experimental data together on a log-log scale. All three sets of data qualitatively show three key features: a plateau at low rates, a transition region (shoulder), and a power-law decay at high rates. A series of discharge simulations (Mechanism I) were also performed with Griffith *et al.*'s experimental conditions to evaluate how discharge capacity depends on rate, which are shown on Figure 4.5 with the red curve. This simulation curve agrees with the experimental data well, and clearly shows the three features mentioned above. Using different cell properties in the simulation moves the location of the shoulder on the curve, but never changes the general shape of the curve. For example, decreasing oxygen solubility or diffusivity in the liquid phase moves the shoulder to lower rate; decreasing positive electrode thickness pushes the shoulder to higher rate and lower capacity.

These observations suggest that two distinct mechanisms determine the cell capacity at low and high rates respectively, as indicated by the two dashed lines associated with each set of experimental data on Figure 4.5. At low rates, O_2 consumption rate

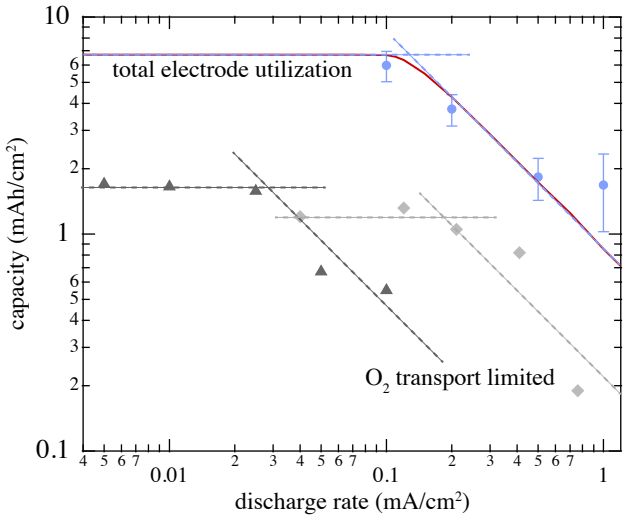

Figure 4.5: Cell capacity as a function of discharge rate. The blue dots with error bars are experimental data obtained by Griffith *et al.*, the triangles by Adam *et al.*, and the diamonds by Lu *et al.*; the red curve is the simulation result generated with mechanism I. For each set of experimental data, two associated dashed lines indicate that two distinct factors limit the cell capacity at low and high discharge rates respectively.

is slow enough for the active species to penetrate through the entire positive electrode, and the electrode is completely utilized. Thus total pore volume and discharge product morphology in the positive electrode determines the cell capacity, which remains relatively constant at the low-rate regime. At higher rates, O_2 reacts so fast within the electrode that diffusion is not able to deliver enough O_2 to locations that are relatively far away from the O_2 source at the current collector. O_2 therefore is fact consumed in the positive electrode, which limits the cell capacity. In the high-rate regime, cell capacity decreases with rising discharge rate.

To confirm the above hypotheses, Figure 4.6 illustrates the distributions of porosity, reaction rate, and O_2 concentration at five depths of discharge (DODs) under Mechanism I. At the lower discharge rate of 0.1 mA cm^{-2}, the O_2 transport rate is fast enough that O_2 is always available. Thus the 'reaction zone' spans the entire electrode. Note that since the reaction distribution is skewed toward the oxygen side of the porous electrode, discharge product forms faster there. At about 60% DOD, the maximum occupancy of discharge product is achieved at the electrode/oxygen interface, and the reaction zone begins to shrink. Since the discharge product is not compact, the growing 'full zone' still permits oxygen diffusion into the electrode interior. The discharge rate is sufficiently low that the diffusion of oxygen across the full zone does not limit capacity. Eventually, the 'full zone' grows to span the entire electrode. In this situation, the electrode is completely utilized at sudden death (at least to the extent allowed by the porosity of the discharge product).

At a higher discharge rate of 0.5 mA cm^{-2}, O_2 transport rate is too slow to match its consumption rate by the electrode reaction. O_2 only penetrates about three quarters of the way into the electrode even before 30% DOD, leaving a 'dead zone' on the separator side where no reaction occurs. As a full zone begins to form, the total rate of reaction throughout the reaction zone has to rise; this forces a higher flux of oxygen, causing the reaction zone to shrink. Eventually, the reaction zone

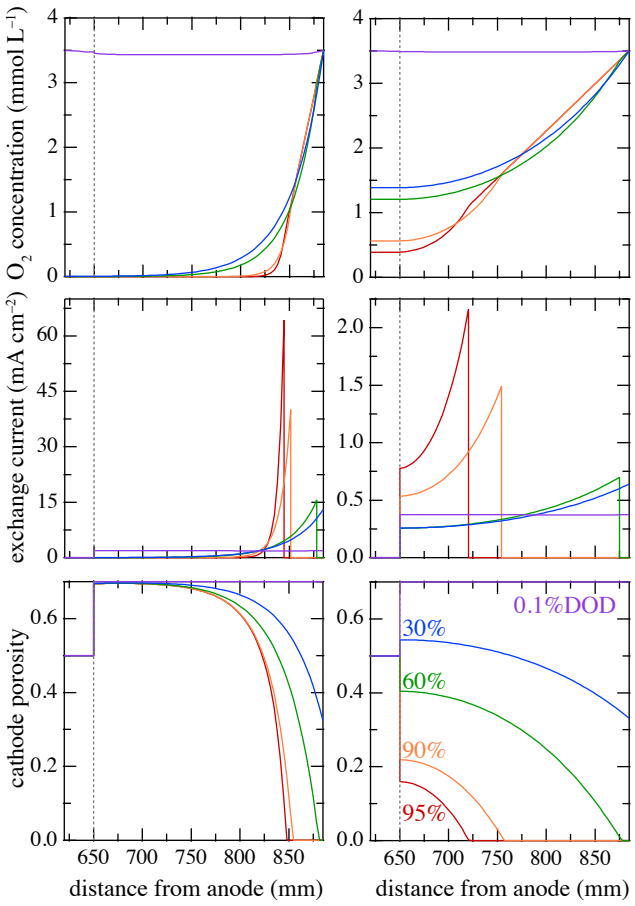

Figure 4.6: Porosity, reaction rate and O_2 concentration distribution in the positive electrode at 5 distinct discharge instants. Plots on the left column are generated at $i_T = 0.5$ mA cm^{-2} (high-rate regime), and those on the right column at $i_T = 0.1$ mA cm^{-2} (low-rate regime). The dashed lines indicate the separator/positive electrode boundaries.

vanishes and the cell dies. In this situation, the electrode is only partially utilized at sudden death.

4.4.4 Capacity *vs.* rate

To understand the power-law decay of capacity apparent in Figure 4.5 one can use the fact that the maximum flux of oxygen through the full zone should match the applied current at sudden death, and that the capacity in this state should scale as the thickness of the full zone. This yields a scaling law that connects the cell capacity to the discharge rate,

$$\text{cell capacity} \sim \frac{F^2 \left\langle \mathscr{D}_{0\mathrm{O}_2}^{\mathrm{eff}} \right\rangle c_{\mathrm{O}_2}^{\mathrm{sat}} c_{\mathrm{Li_2O_2}}^{\mathrm{max}}}{i_{\mathrm{T}}} \tag{4.15}$$

Here $\left\langle \mathscr{D}_{0\mathrm{O}_2}^{\mathrm{eff}} \right\rangle$ is an average diffusivity of oxygen through the pore-filling liquid. (Since local porosity varies during the discharge process, this average diffusivity differs somewhat from the diffusivity used in simulations.) Equation 4.15 suggests that the cell capacity is inversely proportional to discharge rate, and explains the slope of about −1 at high rates on the capacity *vs.* rate log-log plot. The slight deviation from −1 comes from the fact that the effective diffusion coefficient varies with regards to position and time as discharge progresses; thus the average quantity in equation 4.15 is expected to change slightly with discharge rate.

In Figure 4.5, as the discharge rate gets higher, the predicted capacity gets systematically lower than the experimental values given by Griffith *et al.* This probably owes to the rate dependence of the discharge-product layer morphology [111, 112, 114, 144], which is neglected in these simulations. SEM images from the literature [116, 176, 177] show that various sizes of $\mathrm{Li_2O_2}$ particles form when different discharge currents are applied; in the model these would reflect different discharge-product-layer porosities $\varepsilon_{\mathrm{dp}}$. At low rates, $\mathrm{Li_2O_2}$ particles are disk-like, porosity $\varepsilon_{\mathrm{dp}}$ is relatively high; at

high rates, the particles are needle-like, making $\varepsilon_{\mathrm{dp}}$ lower. Combining equation 4.13 with scaling law 4.15, one can conclude that that smaller $\varepsilon_{\mathrm{dp}}$ should yield higher cell capacity, as shown by the comparison between the simulation and the experimental data in Figure 4.5.

4.5 Conclusion

Three mechanisms are proposed and implemented with continuum-scale three-phase models to study the first discharge process of a Li/O_2 battery. Discharge-product layer morphologies and positive-electrode reaction locations are assumed different in the mechanisms. The simulation discharge curves are compared with the experimental ones to validate the mechanisms. Mechanisms I and II give good matches, while mechanism III does not. We conclude that ohmic potential drop across the discharge-product layer should not play an important role in the cell, and positive-electrode kinetic overpotential should be the main source of cell potential drop. Electrode reaction can either occur at the discharge-product/backbone interface, or at the discharge-product/liquid-electrolyte interface. In the former situation, ions carry the current through the Li_2O_2 layer instead of electrons, thereby avoiding an ohmic drop across the layer. In the latter, electrons carry the current through the layer, whose electric resistivity should be equal or lower than that of a semiconductor.

Cell capacity *vs.* discharge rate curves on a log-log scale are composed of a plateau, a shoulder and a straight-line decay. Using different cell properties in the simulation moves the shoulder around on the plot without varying the general shape of the curve. The plateau and the decay parts of the curve correspond to two distinct factors that determine the cell capacity, and the shoulder is the transition between them. In the plateau region (low-rate region), cell capacity is determined by the total volume of the electrode pores, while in the decay region (high-rate region), it is limited by O_2 transport. Development of distributions of O_2, electrode reaction, and porosity in the

positive electrode during discharge are also provided to confirm the capacity-limiting factors. Finally, a dimensional analysis gives a scaling rule to explain the '−1' slope of the straight-line decay.

CHAPTER V

Charging Mechanism of Na/O_2 Batteries

5.1 Introduction

The concept of an alkali-metal/oxygen (M/O_2) battery was first introduced by Abraham and Jiang in 1996, who reported a rechargeable lithium/oxygen (Li/O_2) cell [3]. The development of electric vehicles has spurred research into these high-energy-density battery systems [178]. The Li/O_2 cell is of particular interest because of its exceptionally high theoretical energy density of 3500 Wh kg^{-1}, which is far greater than that of the present lithium-ion (Li-ion) battery (550 Wh kg^{-1}) [179]. Despite its promise, a number of practical problems face Li/O_2 system development, including the extremely high overpotentials that accompany the discharge and recharge processes [6, 176, 180]. High overpotentials translate into large energy losses during cycling, which substantially lower the practically available energy density from its theoretical maximum. Large overpotentials are also associated with poor power efficiency, which significantly affects the performance of Li/O_2 cells, even at moderate drain rates. Many research efforts have been dedicated to understanding and lowering overpotentials: theoretical models have been developed and simulations have been implemented to identify sources of voltage losses [115, 120, 121, 181], and catalysts have been designed to improve reaction kinetics [138, 161, 182, 183].

Recently, a number of groups have proposed the idea of replacing lithium with

sodium to build a similar sodium/oxygen (Na/O_2) battery [4, 184–187]. Like the Li/O_2 cell, the Na/O_2 cell comprises a pure-sodium negative electrode, a porous, air-breathing positive electrode, and an electrolyte-soaked separator between the electrodes. At the negative electrode, the interfacial half-reaction

$$Na^+ + e^- \rightleftharpoons Na \tag{5.1}$$

ideally occurs. At the positive electrode, two reactions have been thought possible, producing sodium peroxide (Na_2O_2) or sodium superoxide (NaO_2) discharge products. Sun *et al.* assembled a Na/O_2 battery, which was cycled at room temperature [184]. Crystalline Na_2O_2 was found to form on discharge and disappear on charge, and NaO_2 was believed to be an intermediate species. On the other hand, Hartmann *et al.* pointed out that sodium and lithium exhibit quite different oxygen reactivity, although they are in the same group and adjacent to each other on the periodic table [4]. While lithium superoxide (LiO_2) is highly unstable and quickly disproportionates to Li_2O_2 and O_2 in the Li/O_2 environment, NaO_2 can be stably formed during the discharge of a Na/O_2 battery through

$$Na^+ + O_2 + e^- \rightleftharpoons NaO_2. \tag{5.2}$$

This reaction has been confirmed to dominate by several research groups [4, 180, 186–188]. The equilibrium open-circuit cell potential of a Na/O_2 battery is measured to be $U^\ominus = 2.27$ V based on half-reactions 5.1 and 5.2.

There has been substantial research into the reversibility of the Na/O_2 cell reaction. Hartmann *et al.* presented a methodology for studying the positive-electrode kinetics by measuring the pressure dynamics in the enclosed oxygen reservoir attached to the battery cell [187]. McCloskey *et al.* plotted the number of electrons per number of O_2 molecules consumed and generated during discharge and charge for Li/O_2 and

Na/O_2 batteries, and showed that the Na/O_2 system has higher coulombic efficiency than Li/O_2 [180].

This chapter seeks to use a multiphase, multi-physics continuum model to study the Na/O_2 battery, and bring insight into the reaction reversibility and the recharging mechanism. The model treats the insoluble discharge product, assumed to predominantly comprise NaO_2, as a separate phase in the positive electrode (in addition to the liquid-electrolyte phase and the solid-backbone phase). The discharge-product phase grows during discharge, when NaO_2 is produced, and shrinks during recharge, when it is consumed.

5.2 Model description

Although Chapter IV provides more details [181], a brief overview of the air-battery cell model will be stated here. The cell is assumed to be planar, made up of a solid negative electrode and a porous, electrolyte-saturated positive electrode; the two electrodes sandwich a slab of electrolyte-saturated porous separator material. Macroscopic material transport in the direction perpendicular to the electrode/separator interfaces occurs through the liquid phase, which permeates the separator and positive electrode. Material and charge transports in the liquid phase are governed by a modified concentrated-solution model [100]. Electronic conduction through the solid backbone is governed by Ohm's law, which relates the local current density in the positive electrode to the electrostatic potential drop within it [35, 36]. Interfacial half-reactions are taken to occur at the surface of the negative electrode and on the pore surface within the positive electrode. Oxygen sorption is assumed to be quasi-equilibrated at the liquid/gas interface on the outside edge of the positive electrode.

The porous electrode domain is taken to comprise three phases: the pore-filling liquid-electrolyte, the electronically conductive solid-backbone, and a discharge-product-layer phase that occupies the pores to an increasing extent as the cell's state

of charge (SOC) decreases. As the discharge-product layer grows and shrinks during discharge and charge, the positive-electrode porosity varies with local SOC, indicating the amount of discharge product 'stored' within the pores at each point within the positive electrode.

Chapter IV probed different mechanisms by which the morphology and charge-transport capability of the discharge-product layer can vary with SOC [181]. Li/O_2 first-discharge data were found to be consistent with a mechanism in which the discharge-product layer is electronically resistant but retains a porous structure that permits ion transport. This allows half-reaction 5.2 to proceed freely at every SOC, because the porosity of the discharge product permits perpetual interfacial contact between the liquid electrolyte and solid backbone during the discharge process.

The half-reactions at both electrodes are taken to be elementary, and can be described by Butler-Volmer kinetics. Reactions in cathodic and anodic directions are both accounted in a single Butler-Volmer equation. For positive-electrode reaction 5.2, this equation can be written as

$$\frac{i_{\mathrm{n}}}{i^{*}} = \left(\frac{a_{\mathrm{Na^{+}}}}{a^{\mathrm{ref}}_{\mathrm{Na^{+}}}}\right)^{-s_{\mathrm{Na^{+}}}} \left(\frac{a_{\mathrm{O_2}}}{a^{\mathrm{ref}}_{\mathrm{O_2}}}\right)^{-s_{\mathrm{O_2}}} \exp\left[\frac{(1-\beta)\, n_{\mathrm{e^{-}}} F \eta_{\mathrm{s}}^{+}}{RT}\right] - \left(\frac{a_{\mathrm{NaO_2}}}{a^{\mathrm{ref}}_{\mathrm{NaO_2}}}\right)^{s_{\mathrm{NaO_2}}} \exp\left(-\frac{\beta n_{\mathrm{e^{-}}} F \eta_{\mathrm{s}}^{+}}{RT}\right), \tag{5.3}$$

where i^{*} is the exchange-current density, β the symmetry factor, $n_{\mathrm{e^{-}}} = 1$ the number of electrons transferred in the reaction; s_k represents the stoichiometric coefficient of species k in the reaction (negative for reactants and positive for products when a half-reaction is written as a reduction). Within a volume element of the positive electrode, the current exchanged between the electrolyte phase and the backbone phase per unit pore area, i_{n}, is directly proportional to the reaction rate. Surface overpotential, η_{s}^{+}, measures the excess potential drop between the liquid and solid phases in the volume element relative to the equilibrium voltage of the half-reaction; it provides the driving force for the reaction. Butler-Volmer equation 5.3 defines

the surface overpotential as a reduction potential and i_{n} as a cathodic current. In a discharge process, η_{s}^{+} is positive, driving the reaction in the cathodic direction (toward the right of reaction 5.2); during a charge process, η_{s}^{+} is negative, driving the reaction in the anodic direction (toward the left of reaction 5.2).

The prefactors of the cathodic and anodic terms of equation 5.3 involve ratios between species activities, a_k, and the reference activities at which the equilibrium potential is established, a_k^{ref}. Liquid-phase species activities relate to their local concentrations, given as functions of position x and time t by the transport equations. Since the insoluble discharge product forms a pure, single-component, separate phase, its activity is taken to be $a_{\mathrm{NaO_2}} = 1$ when present (when SOC > 0), and $a_{\mathrm{NaO_2}} = 0$ when not present (when SOC = 0).

Table 5.1 lists all the properties used for simulations, which were developed for comparison with the experimental $\mathrm{Na/O_2}$ data reported by Hartmann *et al.* [4]. Geometric characteristics of the cell (including the separator and positive-electrode thicknesses L_{sep} and L_{+}) and its constituent materials (including the initial positive-electrode porosity and surface-to-volume ratio ε_0 and a_{V0}) are obtained from their paper. The separator porosity $\varepsilon_{\mathrm{sep}}$ is assumed to be 0.5. Ma measured the complete set of transport properties for sodium triflate ($\mathrm{NaSO_3CF_3}$) in poly(ethylene oxide) (PEO, with up to 160 repeating units), chemically similar to the $\mathrm{NaSO_3CF_3}$ salt and the diethylene glycol dimethyl ether (DEGDME) solvent used by Hartmann; thus electrolyte properties such as Stefan-Maxwell diffusion coefficients ($\mathscr{D}_{jk}$) and the electrolyte partial molar volume ($\overline{V}_{\mathrm{e}}$) are calculated or estimated from their measurements [21]. The diffusivity ($\mathscr{D}_{0\mathrm{O_2}}$) and solubility ($c_{\mathrm{O_2}}^{\mathrm{sat}}$) of $\mathrm{O_2}$ are obtained and estimated from similar electrolytic solutions for $\mathrm{Li/O_2}$ batteries [154], and diffusing $\mathrm{O_2}$ molecules are assumed to place minimal drag on diffusing ions (*i.e.*, $\mathscr{D}_{+\mathrm{O_2}} = \mathscr{D}_{-\mathrm{O_2}} = \infty$). Molar volumes of the solvent ($\overline{V}_0$) and the discharge product ($\overline{V}_{\mathrm{NaO_2}}$) are obtained from the CRC handbook [5], and the conductivity of the solid backbone σ_{C} from ref-

prop.	value	ref.	prop.	value	ref.
electrolyte			**discharge-product layer**		
$\mathscr{D}_{0+}$	1.18×10^{-10} m^2 s^{-1}	[188]	i^*	800 nA cm^{-2}	
$\mathscr{D}_{0-}$	6.67×10^{-10} m^2 s^{-1}	[188]	β	0.5	
$\mathscr{D}_{0\mathrm{O}_2}$	1.80×10^{-9} m^2 s^{-1}	[100]	$\overline{V}_{\mathrm{NaO}_2}$	25.0 cm^3 mol^{-1}	[5]
$\mathscr{D}_{+-}$	8.30×10^{-11} m^2 s^{-1}	[188]	**separator & solid backbone**		
$\mathscr{D}_{+\mathrm{O}_2}$	∞		L_+	210 µm	[4]
$\mathscr{D}_{-\mathrm{O}_2}$	∞		a_{V0}	0.45 µm^{-1}	[4]
$c^{\mathrm{sat}}_{\mathrm{O}_2}$	3.5 mM	[100]	ε_0	0.8	[4]
$\overline{V}_0$	143.2 cm^3 mol^{-1}	[5]	σ_{C}	1 S mm^{-1}	[171]
$\overline{V}_{\mathrm{e}}$	30.6 cm^3 mol^{-1}	[188]	L_{sep}	260 µm	[4]
$\overline{V}_{\mathrm{O}_2}$	0 cm^3 mol^{-1}		$\varepsilon_{\mathrm{sep}}$	0.5	

Table 5.1: Mechanical and material properties used in the simulation.

erence [171]. The exchange current density and the discharge-product-layer porosity are taken to be 800 nA cm^{-2} and 0.82 to best fit the experimental discharge/charge curves obtained at various rates. All simulations are implemented under the assumption that temperature and pressure are constant.

5.3 Results and discussion

In the experiments of Hartmann *et al.*, Na/O_2 cells were discharged with constant current until the cell voltage dropped to a cutoff value of 1.8 V, then held at open circuit until the potential relaxed back to equilibrium before being recharged with the same constant current up to a cutoff voltage of 3.0 V [4]. Simulations using the same control parameters were implemented to produce the discharge/charge curves reported here.

Figure 5.1 shows experimental data from Hartmann *et al.*[4] in blue. Several features are displayed by the experimental curves: as discharge proceeds, there is an initial cell-potential relaxation, followed by a steady cell-potential plateau, which terminates in a 'sudden death' of voltage; the transition from discharge to charge is accompanied by a steep increase in cell potential; as recharge proceeds, another cell-potential relaxation occurs, followed by a fairly steady recharge-voltage plateau, and finally, an extremely sharp rise of cell potential. The simulated curves (in red) shown on Figure 5.1 reproduce almost all the features mentioned above except for the potential relaxations at the beginning of the charge process, and the SOC at which the potential shoots up at the end of charge.

At the discharge/charge rate of 120 µA cm^{-2}, the experimental discharge/charge curve displays overpotentials of about 70 mV and 30 mV—much lower than the overpotentials of the Li/O_2 cell also assembled and studied by Hartmann *et al.* [4]. Adopting the same Butler-Volmer equation 5.3 in discharge and charge, the simulation gives both overpotentials between 60 and 70 mV, qualitatively matching the

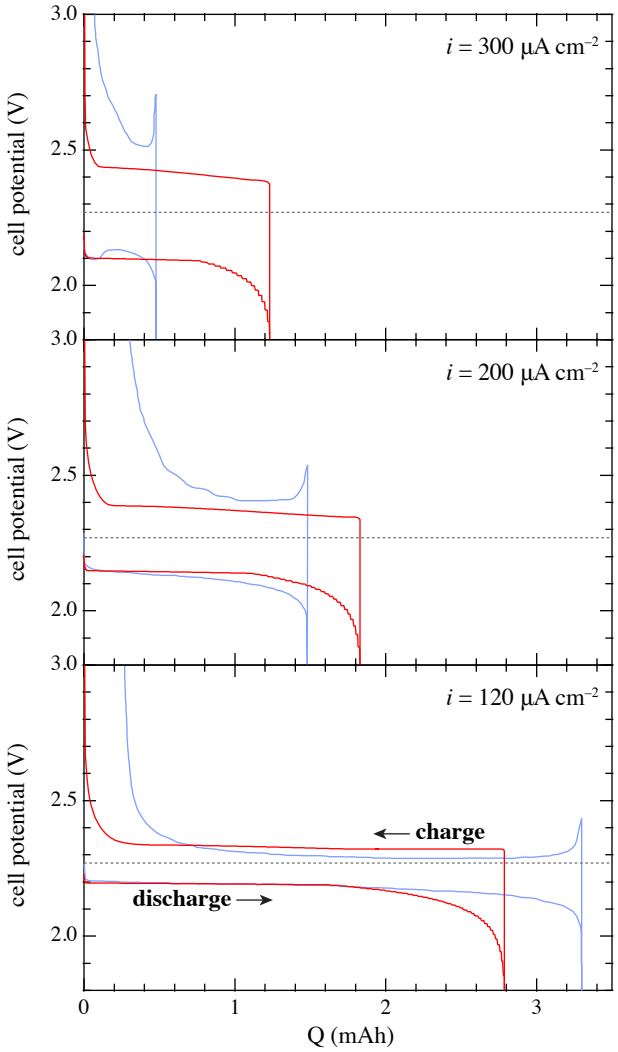

Figure 5.1: Discharge and charge of the Na/O_2 battery at a series of rates. The blue curves are the experimental data obtained by Hartmann *et al.*, and the red ones are simulated curves. The dashed lines indicate the equilibrium cell potential of 2.27 V.

low-overpotential features claimed for the Na/O_2 system. The fact that the same Butler-Volmer kinetics give low and comparable overpotentials during discharge and charge supports the argument that the mechanism of Na/O_2-battery discharge/charge follows a pathway in which the rate-determining electrochemical step has relatively low activation energy, and is similar during both discharge and charge. The Li/O_2 system, on the other hand, suffers from a charging overpotential about 3 to 4 times greater than the discharging overpotential, suggesting asymmetric cell reaction pathways or even asymmetric chemistry.

Figure 5.2 provides a breakdown of the overpotential during cycling of the Na/O_2 cell at rate $120\,\mu A\ cm^{-2}$. Three dynamic processes contribute to the overpotential: there is potential loss due to electrolyte transport (including diffusion overpotential and ohmic potential drop), loss due to negative-electrode kinetics (reaction 5.1), and loss due to positive-electrode kinetics (reaction 5.2). The potential losses are recorded as percentages of the total overpotential with respect to the SOC. Upon discharge, the electrolyte transport and the negative-electode kinetics both contribute about 5% of the total overpotential, while positive-electrode kinetics makes about 90% of the total overpotential, which rises to about 98% at the 'sudden death' of the cell. Upon charge, electrolyte transport contributes about 10% of the overpotential; negative-electrode kinetics accounts for around 5%. At the end of charge, cell potential shoots up steeply due to the sharp increase of kinetic overpotential at the positive electrode,which again accounts for almost all of the observed overpotential.

The sudden decrease in cell potential at the end of discharge and the sharp increase at the end of charge both owe to the fact that positive-electrode reaction 5.2 is starved of reactants in one direaction or the other. Numerous researchers have demostrated that the sudden death of Li/O_2 batteries during discharge is due to the fact that O_2 becomes inaccessible in certain regions of the positive electrode [155, 157, 164, 181]. The lack of O_2 pushes the positive-electrode surface overpotential to a very high value,

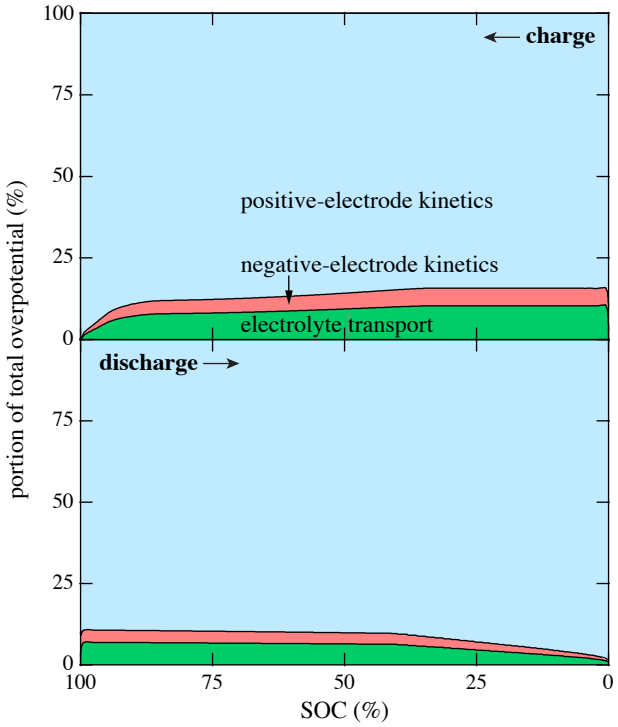

Figure 5.2: Overpotential breakdowns for discharge and charge processes. The discharge/charge rate is 120 µA cm^{-2}.

which can no longer be delivered by the cell reaction. Similarly, the steep potential rise at the end of charge occurs due to the disappearance of the discharge product (*i.e.*, NaO_2 or Na_2O_2 in a Na/O_2 cell).

Figure 5.3 shows the distributions of i_n and ε in the positive electrode during the charge process. The local value of i_n corresponds to the interfacial reaction rate, and that of ε, the amount of insoluble NaO_2 'stored' in the positive electrode's pores. At the beginning of charge, NaO_2 is stored everywhere throughout the electrode, and the electrode reaction is distributed relatively uniformly. At high discharge rate, pores are fully utilized (completely full of discharge product) on the side of the positive electrode adjacent to the O_2 gas reservoir. They are only partially full at the interface with the separator [181], as indicated by the distribution of porosity at 0.1% SOC. The discharge product is therefore first completely consumed on the separator side of the positive electrode. The limited availability of reactant severely increases the magnitude of local surface overpotential needed to drive reaction 5.2 to the left; the reaction zone is consequently constrained to the region where NaO_2 is still available, as shown by the 60%- and 80%-SOC distributions of i_n. At the end of charge, cell potential shoots up due to the dramatic rise in positive-electrode surface overpotential, suggesting the completion of recharge.

The sudden rise of cell potential on charge happens at a lower SOC in the experiment than in the simulation. This is probably caused by the presence of some undesired side reactions that occur towards the end of discharge, which lead the battery to yield less apparent capacity during recharge; there may also be side reactions that occur in parallel with the recharge process [4], which are not accounted for in the simulation.

Another feature in the experimental charge curve that is not given by the simulation is the cell voltage relaxation at the beginning of charge. We postulate that this relaxation is induced by the redistribution of O_2 in the system. The electrochemical

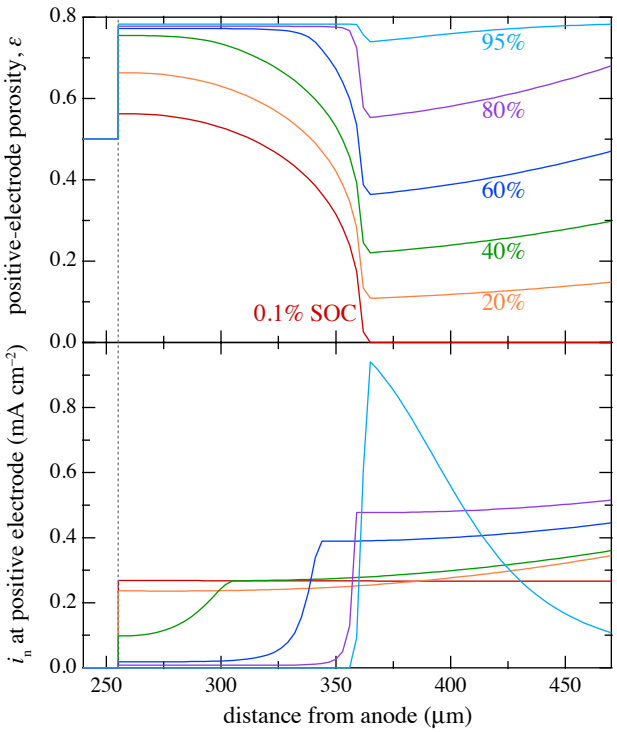

Figure 5.3: Positive-electrode porosity and reaction distributions at six distinct SOCs during the charging process at the rate of 120 µA cm^{-2}. The dashed line represents the interface between the battery separator and the positive electrode.

potential of O_2 should contribute to the cell voltage, which factor, however, is not considered in the current simulation, as the interaction between O_2 and the charged species is neglected (*i.e.*, $\mathscr{D}_{+O_2} = \mathscr{D}_{-O_2} = \infty$). Further research is needed to understand how concentration overpotentials might arise from electro-osmotic drag on diffusing oxygen.

5.4 Conclusion

The first discharge/charge cycle of a Na/O_2 battery is simulated with a continuum-scale multiphase model. The model adopts identical Butler-Volmer kinetic formulas to simulate the discharging and the charging processes. The simulated discharge/charge curves successfully reproduce most of the features of the experimental curves. The fact that the same kinetic equation can describe discharge and charge suggests that the cell reactions in the Na/O_2 battery are not only chemically reversible, but also take pathways during discharge and recharge that have the same rate-determining electrochemical steps. An overpotential breakdown reveals that potential loss to positive-electrode kinetics dominates the total overpotential on both discharge and charge. Finally a detailed analysis of positive-electrode porosity and reaction distributions indicates that the lack of reactant (O_2 for discharge, and NaO_2 for charge) causes the sudden death and sudden cell-potential rise at the end of the discharging and charging processes.

APPENDICES

APPENDIX A

Bulk-solution model closure

Closure for multidimensional simulations with Faradaic convection and the excluded-volume effect can be achieved by the adoption of a momentum balance, with sufficient generality being supplied by the Cauchy equation

$$\rho\left(\frac{\partial\vec{v}}{\partial t}+\vec{v}\cdot\vec{\nabla}\vec{v}\right)=-\vec{\nabla}p-\vec{\nabla}\cdot\vec{\vec{\tau}}+\rho\vec{b}, \tag{A.1}$$

where ρ is the mass density, $\vec{v}$ the mass-average velocity, p the external pressure, $\vec{\vec{\tau}}$ the deformation-stress tensor, and $\vec{b}$ a vector quantifying how local body acceleration depends on position, electric field, *etc.* In addition to vector equation A.1, a tensor constitutive law such as the Navier-Stokes law (for Newtonian liquids),

$$\vec{\vec{\tau}}=-\mu\left[\vec{\nabla}\vec{v}+\left(\vec{\nabla}\vec{v}\right)^{\mathrm{T}}-\tfrac{2}{3}\vec{\vec{I}}\vec{\nabla}\cdot\vec{v}\right], \tag{A.2}$$

where $\vec{\vec{I}}$ is the identity tensor, is needed to relate the components of $\vec{\vec{\tau}}$ to $\vec{v}$ and account for viscosity μ or other mechanical properties. (An alternative to equation A.2, which applies to porous separator media or gel electrolytes, is to set $\vec{\vec{\tau}}=\vec{\vec{0}}$ and adopt d'Arcy's law to relate the pressure gradient to mass-average velocity.) The

constitutive law

$$\rho = c_{\mathrm{T}} \sum_{k=1}^{n} M_k y_k \tag{A.3}$$

expresses ρ in terms of total molar concentration, the composition basis, and the particle molar masses M_k; and the vector constitutive law

$$\rho \vec{v} = \sum_{k=1}^{n} M_k \vec{N}_k \tag{A.4}$$

defines the mass-average velocity. (It is necessary to use the mass-average velocity as a basis for momentum so that the definitions of total mass flux and local momentum density coincide—equation A.4 defines both.) Equations A.1 through A.4 represent a set of governing equations over $d^2 + 2d + 1$ scalar components.

In a d-dimensional space, consideration of momentum requires that more dependent variables be involved in the calculation: $\vec{\vec{\tau}}$ ($d \times d = d^2$ scalar components), $\vec{v}$ (d scalar components), p (1 scalar), and ρ (1 scalar). $d^2 + d + 2$ unknowns are added to the model listed in table 2.1. In light of the additional $d^2 + 2d + 1$ scalar governing equations introduced by momentum considerations, a balance of the total numbers of equations and unknowns is achieved for systems in which $d > 1$.

In multidimensional simulations it is necessary that equilibrium properties such as $\overline{V}_k$ and λ_k be taken to depend on local pressure in thermodynamically consistent ways; pressure gradients should also be incorporated into the Stefan-Maxwell diffusion driving force [33]. Note that Gibbs-Duhem equation 2.14 contains additional terms when pressure or temperature varies, so care must be taken when analyzing the thermodynamic consistency of parameters.

APPENDIX B

Transformation to moving frames

Sundstrøm and Bark provided a path to solve moving-boundary problems in parallel-electrode symmetric plating/stripping cells [55], by expressing the entire problem in a frame moving uniformly at $\vec{v}_{\text{surf}}$ as follows. Introduce a new coordinate system, $(t', \vec{x}')$, where the time t' and position $\vec{x}'$ are described by transformed variables

$$t' = t \text{ and } \vec{x}' = \vec{x} - \int_0^t \vec{v}_{\text{surf}} dt. \tag{B.1}$$

With the chain rule, differential operators in the two coordinate systems can be related through

$$\frac{\partial}{\partial t} = \frac{\partial}{\partial t'} - \vec{v}_{\text{surf}} \cdot \vec{\nabla}' \text{ and } \vec{\nabla} = \vec{\nabla}', \tag{B.2}$$

where it is understood that if both frames are orthogonal coordinate systems, then

$$\vec{\nabla} = \vec{e}_1 \frac{\partial}{\partial x_1} + \vec{e}_2 \frac{\partial}{\partial x_2} + \vec{e}_3 \frac{\partial}{\partial x_3} \text{ and } \vec{\nabla}' = \vec{e}'_1 \frac{\partial}{\partial x'_1} + \vec{e}'_2 \frac{\partial}{\partial x'_2} + \vec{e}'_3 \frac{\partial}{\partial x'_3}. \tag{B.3}$$

Motion of the coordinates also transforms all vectors that quantify flow. Molar fluxes, current density, and volume-average velocity are expressed in the moving frame as

$$\vec{N}_k' = \vec{N}_k - c_{\mathrm{T}} y_k \vec{v}_{\mathrm{surf}}, \ \vec{i}' = \vec{i}, \text{ and } \vec{v}'^{\square} = \vec{v}^{\square} - \vec{v}_{\mathrm{surf}}. \tag{B.4}$$

(Observe that due to electroneutrality, current density is the same in either a stationary or a moving coordinate.) Using transformations B.2 through B.4, equation 2.9 is

$$\frac{\partial \left(c_{\mathrm{T}} y_k\right)}{\partial t'} = -\vec{\nabla}' \cdot \vec{N}_k' \tag{B.5}$$

in the moving frame, and boundary conditions 2.34 become

$$\left(\vec{N}_k' \cdot \vec{n}\right)\Big|_{\vec{S}_0} = \left\{\left[y_k c_{\mathrm{T}} \left(\vec{v}_{\mathrm{conv}} - \vec{v}_{\mathrm{surf}}\right) + \frac{s_k \vec{i}'}{F z_{\mathrm{e}^-} n_{\mathrm{e}^-}}\right] \cdot \vec{n}\right\}\Bigg|_{\vec{S}_0}. \tag{B.6}$$

For a planar symmetric deposition/stripping cell without free or forced convection, in which all species formed in other phases displace the interfacial surface, $\vec{v}_{\mathrm{surf}}$ is proportional to the current through equation 2.41, but does not need to be considered explicitly when solving the transport equations because $\vec{v}_{\mathrm{conv}} = \vec{v}_{\mathrm{surf}}$, canceling the convective term from equation B.6. The equation system in table 2.1 applies, with flux vectors and differential operators residing in a coordinate frame that moves with the system boundaries over time. Primes are suppressed in most of the equations from section 2.4 for notational simplicity.

BIBLIOGRAPHY

BIBLIOGRAPHY

[1] Energy information administration monthly energy review (Oct. 2014).

[2] V. Srinivasan, Batteries for vehicular applications, AIP Conference Proceedings Physics of Sustainable Energy 1044 (2008) 283–296.

[3] K. M. Abraham, Z. Jiang, A polymer electrolyte-based rechargeable lithium/oxygen battery, Journal of The Electrochemical Society 143 (1996) 1–5.

[4] P. Hartmann, C. L. Bender, M. Vracar, A. K. Dürr, A. Garsuch, J. Janek, P. Adelhelm, A rechargeable room-temperature sodium-superoxide (NaO_2) battery, Nature Materials 12 (2013) 228–232.

[5] W. M. Haynes (Ed.), CRC Handbook of Chemistry and Physics, 94th ed., CRC Press, LLC, 2013.

[6] J. Christensen, P. Albertus, R. S. Sanchez-Carrera, T. Lohmann, B. Kozinsky, R. Liedtke, J. Ahmed, A. Kojic, A critical review of Li/air batteries, Journal of The Electrochemical Society 159 (2011) R1–R30.

[7] D. N. Bennion, C. W. Tobias, Current distribution at a gas-electrode-electrolyte interface: II . theoretical treatment, Journal of The Electrochemical Society 113 (1966) 593–599.

[8] J. Newman, Engineering design of electrochemical systems, Industrial & Engineering Chemistry 60 (1968) 12–27.

[9] J. S. Dunning, D. N. Bennion, J. Newman, Analysis of porous electrodes with sparingly soluble reactants: II . variable solution properties, convection, and complexing, Journal of The Electrochemical Society 120 (1973) 906–913.

[10] J. Newman, W. Tiedemann, Porous-electrode theory with battery applications, AIChE Journal 21 (1975) 25–41.

[11] Y. Kao, P. C. Wayner, The transient response of the sulfur/polysulfide electrode based on a varying concentration model, Journal of The Electrochemical Society 124 (1977) 230–236.

[12] R. Pollard, J. Newman, Transport equations for a mixture of two binary molten salts in a porous electrode, Journal of The Electrochemical Society 126 (1979) 1713–1717.

[13] T. I. Evans, T. V. Nguyen, R. E. White, A mathematical model of a lithium/thionyl chloride primary cell, Journal of The Electrochemical Society 136 (1989) 328–339.

[14] B. Paxton, J. Newman, Modeling of nickel/metal hydride batteries, Journal of The Electrochemical Society 144 (1997) 3818–3831.

[15] V. Srinivasan, J. W. Weidner, R. E. White, Mathematical models of the nickel hydroxide active material, Journal of Solid State Electrochemistry 4 (2000) 367–382.

[16] D. Dees, E. Gunen, D. Abraham, A. Jansen, J. Prakash, Electrochemical modeling of lithium-ion positive electrodes during hybrid pulse power characterization tests, Journal of The Electrochemical Society 155 (2008) A603–A613.

[17] A. Shah, M. Watt-Smith, F. Walsh, A dynamic performance model for redox-flow batteries involving soluble species, Electrochimica Acta 53 (2008) 8087–8100.

[18] A. A. Shah, X. Li, R. G. A. Wills, F. C. Walsh, A mathematical model for the soluble lead-acid flow battery, Journal of The Electrochemical Society 157 (2010) A589–A599.

[19] R. Chandrasekaran, T. F. Fuller, Analysis of the lithium-ion insertion silicon composite electrode/separator/lithium foil cell, Journal of The Electrochemical Society 158 (2011) A859–A871.

[20] R. Purkayastha, R. M. McMeeking, A linearized model for lithium-ion batteries and maps for their performance and failure, Journal of Applied Mechanics-Transactions of the ASME 79 (2012).

[21] Y. Ma, M. Doyle, T. F. Fuller, M. M. Doeff, L. C. DeJonghe, J. Newman, The measurement of a complete set of transport properties for a concentrated solid polymer electrolyte solution, Journal of The Electrochemical Society 142 (1995) 1859–1868.

[22] A. Ferry, M. M. Doeff, L. C. DeJonghe, Transport property measurements of polymer electrolytes, Electrochimica Acta 43 (1998) 1387–1393.

[23] M. M. Doeff, P. Georen, J. Qiao, J. Kerr, L. C. DeJonghe, Transport properties of a high molecular weight poly(propylene oxide)-$LiCF_3SO_3$ system, Journal of The Electrochemical Society 146 (1999) 2024–2028.

[24] M. M. Doeff, L. Edman, S. E. Sloop, J. Kerr, L. C. DeJonghe, Transport properties of binary salt polymer electrolytes, Journal of Power Sources 89 (2000) 227–231.

[25] H. Hafezi, J. Newman, Verification and analysis of transference number measurements by the galvanostatic polarization method, Journal of The Electrochemical Society 147 (2000) 3036–3042.

[26] P. Georén, G. Lindbergh, Characterisation and modelling of the transport properties in lithium battery gel electrolytes: Part I. the binary electrolyte PC/$LiClO_4$, Electrochimica Acta 49 (2004) 3497 – 3505.

[27] L. O. Valøen, J. N. Reimers, Transport properties of $LiPF_6$-based Li-ion battery electrolytes, Journal of The Electrochemical Society 152 (2005) A882–A891.

[28] J. Newman, D. Bennion, C. W. Tobias, Mass transfer in concentrated binary electrolytes, Berichte der Bunsengesellschaft 69 (1965).

[29] J. Newman, Effect of ionic migration on limiting currents, Industrial & Engineering Chemistry Fundamentals 5 (1966) 525–529.

[30] J. Newman, T. W. Chapman, Restricted diffusion in binary solutions, AIChE Journal 19 (1973) 343–348.

[31] J. Newman, C. W. Tobias, Transport processes in electrolytic solutions, Advances in Electrochemistry and Electrochemical Engineering 5 (1967) 87–135.

[32] J. Newman, K. E. Thomas-Alyea, Electrochemical Systems, 2nd ed., Prentice-Hall, 1991.

[33] L. Onsager, Theories and problems of liquid diffusion, Annals of the New York Academy of Sciences 46 (1945) 241–265.

[34] E. N. Lightfoot, E. L. Cussler, R. L. Rettig, Applicability of the stefan-maxwell equations to multicomponent diffusion in liquids, AIChE Journal 8 (1962) 708–710.

[35] M. Doyle, T. F. Fuller, J. Newman, Modeling of galvanostatic charge and discharge of the lithium/polymer/insertion cell, Journal of The Electrochemical Society 140 (1993) 1526–1533.

[36] T. F. Fuller, M. Doyle, J. Newman, Simulation and optimization of the dual lithium ion insertion cell, Journal of The Electrochemical Society 141 (1994) 1–10.

[37] R. Darling, J. Newman, Modeling a porous intercalation electrode with two characteristic particle sizes, Journal of The Electrochemical Society 144 (1997) 4201–4208.

[38] P. M. Gomadam, J. W. Weidner, R. A. Dougal, R. E. White, Mathematical modeling of lithium-ion and nickel battery systems, Journal of Power Sources 110 (2002) 267–284.

[39] J. Newman, K. E. Thomas, H. Hafezi, D. R. Wheeler, Modeling of lithium-ion batteries, Journal of Power Sources 119-121 (2003) 838–843.

[40] C. Delacourt, Modeling Li-ion batteries with electrolyte additives or contaminants, Journal of The Electrochemical Society 160 (2013) A1997–A2004.

[41] C. Y. Wang, W. B. Gu, B. Y. Liaw, Micro-macroscopic coupled modeling of batteries and fuel cells: I. model development, Journal of The Electrochemical Society 145 (1998) 3407–3417.

[42] W. B. Gu, C. Y. Wang, B. Y. Liaw, Micro-macroscopic coupled modeling of batteries and fuel cells: II. application to nickelcadmium and nickelmetal hydride cells, Journal of The Electrochemical Society 145 (1998) 3418–3427.

[43] K. A. Smith, C. D. Rahn, C.-Y. Wang, Control oriented 1D electrochemical model of lithium-ion battery, Energy Conversion and Management 48 (2007) 2565–2578.

[44] D. Danilov, P. H. L. Notten, Mathematical modelling of ionic transport in the electrolyte of Li-ion batteries, Electrochimica Acta 53 (2008) 5569–5578.

[45] N. A. Chaturvedi, R. Klein, J. Christensen, J. Ahmed, A. Kojic, Modeling, estimation, and control challenges for lithium-ion batteries, American Control Conference (ACC), 2010 (2010) 1997–2002.

[46] K. A. Smith, C. D. Rahn, W. Chao-Yang, Model-based electrochemical estimation and constraint management for pulse operation of lithium-ion batteries, Control Systems Technology, IEEE Transactions on 18 (2010) 654–663.

[47] Y. Dai, L. Cai, R. E. White, Simulation and analysis of stress in a Li-ion battery with a blended $LiMn_2O_4$ and $LiNi_{0.8}Co_{0.15}Al_{0.05}O_2$ cathode, Journal of Power Sources 247 (2014) 365–376.

[48] G. Sikha, B. N. Popov, R. E. White, Effect of porosity on the capacity fade of a lithium-ion battery: Theory, Journal of The Electrochemical Society 151 (2004) A1104–A1114.

[49] Q. Zhang, R. E. White, Moving boundary model for the discharge of a $LiCoO_2$ electrode, Journal of The Electrochemical Society 154 (2007) A587–A596.

[50] P. Andrei, J. P. Zheng, M. Hendrickson, E. J. Plichta, Some possible approaches for improving the energy density of Li-air batteries, Journal of The Electrochemical Society 157 (2010) A1287–A1295.

[51] S. Khaleghi Rahimian, S. Rayman, R. E. White, Extension of physics-based single particle model for higher charge-discharge rates, Journal of Power Sources 224 (2013) 180–194.

[52] Y. Ji, Y. Zhang, C.-Y. Wang, Li-ion cell operation at low temperatures, Journal of The Electrochemical Society 160 (2013) A636–A649.

[53] W. Du, A. Gupta, X. Zhang, A. M. Sastry, W. Shyy, Effect of cycling rate, particle size and transport properties on lithium-ion cathode performance, International Journal of Heat and Mass Transfer 53 (2010) 3552 – 3561.

[54] A. Gupta, J. H. Seo, X. Zhang, W. Du, A. M. Sastry, W. Shyy, Effective transport properties of $LiMn_2O_4$ electrode *via* particle-scale modeling, Journal of The Electrochemical Society 158 (2011) A487–A497.

[55] W. Shyy, Y.-C. Cho, W. Du, A. Gupta, C.-C. Tseng, A. Sastry, Surrogate-based modeling and dimension reduction techniques for multi-scale mechanics problems, Acta Mechanica Sinica 27 (2011) 845–865.

[56] G. B. Less, J. H. Seo, S. Han, A. M. Sastry, J. Zausch, A. Latz, S. Schmidt, C. Wieser, D. Kehrwald, S. Fell, Micro-scale modeling of Li-ion batteries: Parameterization and validation, Journal of The Electrochemical Society 159 (2012) A697–A704.

[57] V. R. Subramanian, V. Boovaragavan, V. Ramadesigan, M. Arabandi, Mathematical model reformulation for lithium-ion battery simulations: Galvanostatic boundary conditions, Journal of The Electrochemical Society 156 (2009) A260–A271.

[58] P. W. C. Northrop, V. Ramadesigan, S. De, V. R. Subramanian, Coordinate transformation, orthogonal collocation, model reformulation and simulation of electrochemical-thermal behavior of lithium-ion battery stacks, Journal of The Electrochemical Society 158 (2011) A1461–A1477.

[59] V. Ramadesigan, K. Chen, N. A. Burns, V. Boovaragavan, R. D. Braatz, V. R. Subramanian, Parameter estimation and capacity fade analysis of lithium-ion batteries using reformulated models, Journal of The Electrochemical Society 158 (2011) A1048–A1054.

[60] A. Guduru, P. C. Northrop, S. Jain, A. Crothers, T. R. Marchant, V. Subramanian, Analytical solution for electrolyte concentration distribution in lithium-ion batteries, Journal of Applied Electrochemistry 42 (2012) 189–199.

[61] L.-G. Sundstrom, F. H. Bark, On morphological instability during electrodeposition with a stagnant binary electrolyte, Electrochimica Acta 40 (1995) 599–614.

[62] A. Nyman, M. Behm, G. Lindbergh, Electrochemical characterisation and modelling of the mass transport phenomena in $LiPF_6$-EC-EMC electrolyte, Electrochimica Acta 53 (2008) 6356–6365.

[63] A. Nyman, T. G. Zavalis, R. Elger, M. Behm, G. Lindbergh, Analysis of the polarization in a Li-ion battery cell by numerical simulations, Journal of The Electrochemical Society 157 (2010) A1236–A1246.

[64] A. Nyman, M. Behm, G. Lindbergh, A theoretical and experimental study of the mass transport in gel electrolytes I. mathematical analysis of characterization method, Journal of The Electrochemical Society 158 (2011) A628–A635.

[65] A. Nyman, An experimental and theoretical study of the mass transport in lithiumion battery electrolytes, Ph.D. thesis, Kungliga Tekniska Högskolan, 2011.

[66] J. Camacho, H. Brenner, On convection induced by molecular diffusion, Industrial & Engineering Chemistry Research 34 (1995) 3326–3335.

[67] S. Alsoy, J. L. Duda, Influence of swelling and diffusion-induced convection on polymer sorption processes, AIChE Journal 48 (2002) 1849–1855.

[68] R. B. Bird, W. E. Steward, E. N. Lightfoot, Transport Phenomena, 1st ed., John Wiley & Sons, 1960.

[69] C. F. Curtiss, J. O. Hirschfelder, Transport properties of multicomponent gas mixtures, Journal of Chemical Physics 17 (1949) 550–555.

[70] S. A. Shain, A note on multicomponent diffusion, AIChE Journal 7 (1961) 17–19.

[71] J. Newman, The polarized diffuse double layer, Transactions of the Faraday Society 61 (1965) 2229–2237.

[72] K. B. Oldham, A. M. Bond, How valid is the electroneutrality approximation in the theory of steady-state voltammetry?, Journal of Electroanalytical Chemistry 508 (2001) 28–40.

[73] F. H. Stillinger, R. Lovett, Ion-pair theory of concentrated electrolytes. I. basic concepts, The Journal of Chemical Physics 48 (1968) 3858–3868.

[74] E. A. Guggenheim, Thermodynamics: An Advanced Treatment for Chemists and Physicists, 5th ed., North-Holland Physics Publishing, 1967.

[75] C. W. Monroe, C. Delacourt, Continuum transport laws for locally non-neutral concentrated electrolytes, Electrochimica Acta 114 (2013) 649–657.

[76] J. O. Bockris, A. K. N. Reddy, M. Gamboa-Aldeco, Modern Electrochemistry, volume 2, Springer, 2000.

[77] E. A. Guggenheim, The conceptions of electrical potential difference between two phases and the individual activities of ions, The Journal of Physical Chemistry 33 (1929) 842–849.

[78] L. S. Darken, Diffusion, mobility and their interrelation through free energy in binary metallic systems, Transactions of the American Institute of Mining and Metallurgical Engineers 175 (1948) 184–201.

[79] W. H. Smyrl, J. Newman, Potentials of cells with liquid junctions, The Journal of Physical Chemistry 72 (1968) 4660–4671.

[80] T. W. Chapman, J. S. Newman, A Compilation of Selected Thermodynamic and Transport Properties of Binary Electrolytes in Aqueous Solution, University of California, Lawrence Radiation Laboratory, 1968.

[81] A. A. Shinkle, A. E. S. Sleightholme, L. D. Griffith, L. T. Thompson, C. W. Monroe, Degradation mechanisms in the non-aqueous vanadium acetylacetonate redox flow battery, Journal of Power Sources 206 (2012) 490–496.

[82] A. A. Shinkle, A. E. S. Sleightholme, L. T. Thompson, C. W. Monroe, Solvents and supporting electrolytes for vanadium acetylacetonate flow batteries, Journal of Power Sources 238 (2014) 1299–1305.

[83] A. J. Bard, L. R. Faulkner, Electrochemical Methods: Fundamentals and Applications, 2nd ed., Wiley, 2001.

[84] J. Kim, H.-D. Lim, H. Gwonb, K. Kang, Sodium–oxygen batteries with alkyl-carbonate and ether based electrolytes, Physical Chemistry Chemical Physics 15 (2013) 3623.

[85] D. Das, S. K. Ray, D. K. Hazra, A study on volumetric and compressibility properties of some lithium salts in n,n-dimethylacetamide at 25°C, Indian Journal of Chemistry 41A (2002) 1812–1815.

[86] S. G. Stewart, Determination of Transport Properties and Optimization of Lithium-Ion Batteries, Ph.D. thesis, University of Canifornia, 2007.

[87] S. G. Stewart, J. Newman, The use of UV/vis absorption to measure diffusion coefficients in $LiPF_6$ electrolytic solutions, Journal of The Electrochemical Society 155 (2008) F13–F16.

[88] M. Knobel, D. K. Worcester, F. B. Briggs, The transference numbers of potassium hydroxide in aqueous solution, Journal of the American Chemical Society 45 (1923) 77–79.

[89] R. M. Fuoss, L. Onsager, Conductance of strong electrolytes at finite dilutions, Proceedings of the National Academy of Sciences 41 (1955) 274–283.

[90] M. Abramowitz, I. A. Stegun (Eds.), Handbook of Mathematical Functions withFormulas, Graphs, and Mathematical Tables, Tenth Printing, National Bureauof Standards, 1972.

[91] F. Cottrell, The cut off current in galvanic polarisation, considered as a diffusion problem, Zeitschrift fur Physikalische Chemie–Stochiometrie und Verwandtschaftslehre 42 (1903) 385–431.

[92] C. Monroe, J. Newman, Dendrite growth in lithium/polymer systems - a propagation model for liquid electrolytes under galvanostatic conditions, Journal of The Electrochemical Society 150 (2003) A1377–A1384.

[93] M. S. Ding, Electrolytic conductivity and glass transition temperature as functions of salt content, solvent composition, or temperature for $LiPF_6$ in propylene carbonate + diethyl carbonate, Journal of Chemical & Engineering Data 48 (2003) 519–528.

[94] L. Edman, M. M. Doeff, A. Ferry, J. Kerr, L. C. De Jonghe, Transport properties of the solid polymer electrolyte system $P(EO)_n$LiTFSI, The Journal of Physical Chemistry B 104 (2000) 3476–3480.

[95] I. Hodge, M. Ingram, A. West, Impedance and modulus spectroscopy of polycrystalline solid electrolytes, Journal of Electroanalytical Chemistry and Interfacial Electrochemistry 74 (1976) 125–143.

[96] S. Mikhailenko, M. Guiver, S. Kaliaguine, Measurements of PEM conductivity by impedance spectroscopy, Solid State Ionics 179 (2008) 619–624.

[97] P. M. Sipos, G. Hefter, P. M. May, Viscosities and densities of highly concentrated aqueous MOH solutions ($M^+ = Na^+$, K^+, Li^+, Cs^+, $(CH_3)_4N^+$) at 25.0 °C, Journal of Chemical & Engineering Data 45 (2000) 613–617.

[98] H. S. Harned, D. M. French, A conductance method for the determination of the diffusion coefficients of electrolytes, Annals of the New York Academy of Sciences 46 (1945) 267–281.

[99] J. Zhao, L. Wang, X. He, C. Wan, C. Jiang, Determination of lithium-ion transference numbers in $LiPF_6$-PC solutions based on electrochemical polarization and NMR measurements, Journal of The Electrochemical Society 155 (2008) A292–A296.

[100] J. Liu, C. W. Monroe, Solute-volume effects in electrolyte transport, Electrochimica Acta 135 (2014) 447–460.

[101] M. Ciosek, M. Marcinek, G. Żukowska, W. Wieczorek, Lithium transference number measurements and complex abilities in anion trapping triphenyloborane–poly(ethylene oxide) dimethyl ether–lithium trifluoromethanesulfonate composite electrolyte, Electrochimica Acta 54 (2009) 4487–4493.

[102] S. Zugmann, M. Fleischmann, M. Amereller, R. Gschwind, H. Wiemhöfer, G. H. J., Measurement of transference numbers for lithium ion electrolytes *via* four different methods, a comparative study, Electrochimica Acta 56 (2011) 3926–3933.

[103] A. Mehrotra, V. Srinivasan, Transport property measurements for $LiPF_6$ in EC:DEC (1:1), The 224th Electrochemical Society Meeting Abstract # 1152 (2013).

[104] T. Nishida, K. Nishikawa, Y. Fukunaka, Diffusivity measurement of $LiPF_6$, LiTFSI, $LiBF_4$ in PC, ECS Transactions 6 (2008) 1–14.

[105] S. Stewart, J. Newman, Measuring the salt activity coefficient in lithium-battery electrolytes, Journal of The Electrochemical Society 155 (2008) A458–A463.

[106] R. Cvetković, B. N. Popov, H. A. Laitinen, Electrochemical reduction of molybdate in the presence of zinc chloride in molten lithium chloridepotassium chloride eutectic, Journal of The Electrochemical Society 122 (1975) 1616–1619.

[107] B. N. Popov, H. A. Laitinen, Electrochemical reduction of chromate in the presence of nickel chloride in molten lithium chloridepotassium chloride eutectic, Journal of The Electrochemical Society 117 (1970) 482–484.

[108] B. N. Popov, H. A. Laitinen, Electrochemical reduction of molybdenum(VI) compounds in molten lithium chloridepotassium chloride eutectic, Journal of The Electrochemical Society 120 (1973) 1346–1350.

[109] J. Heywood, Internal Combustion Engine Fundamentals, 1st ed., McGraw-Hill Science/Engineering/Math, 1988.

[110] P. G. Bruce, S. A. Freunberger, L. J. Hardwick, J. M. Tarascon, Li-O_2 and Li-S batteries with high energy storage, Nature Materials 11 (2012) 19–29.

[111] B. M. Gallant, R. R. Mitchell, D. G. Kwabi, J. Zhou, L. Zuin, C. V. Thompson, Y. Shao-Horn, Chemical and morphological changes of Li-O_2 battery electrodes upon cycling, The Journal of Physical Chemistry C 116 (2012) 20800–20805.

[112] B. M. Gallant, D. G. Kwabi, R. R. Mitchell, J. Zhou, C. V. Thompson, Y. Shao-Horn, Influence of Li_2O_2 morphology on oxygen reduction and evolution kinetics in Li-O_2 batteries, Energy & Environmental Science 6 (2013) 2518–2528.

[113] B. Horstmann, T. Danner, W. G. Bessler, Precipitation in aqueous lithium-oxygen batteries: a model-based analysis, Energy & Environmental Science 6 (2013) 1299–1314.

[114] B. Horstmann, B. Gallant, R. Mitchell, W. G. Bessler, Y. Shao-Horn, M. Z. Bazant, Rate-dependent morphology of Li_2O_2 growth in Li-O_2 batteries, The Journal of Physical Chemistry Letters 4 (2013) 4217–4222.

[115] J. S. Hummelshøj, A. C. Luntz, J. K. Nørskov, Theoretical evidence for low kinetic overpotentials in Li-O_2 electrochemistry, The Journal of Chemical Physics 138 (2013).

[116] Y.-C. Lu, D. G. Kwabi, K. P. C. Yao, J. R. Harding, J. Zhou, L. Zuin, Y. Shao-Horn, The discharge rate capability of rechargeable Li-O_2 batteries, Energy & Environmental Science 4 (2011) 2999–3007.

[117] Y.-C. Lu, Y. Shao-Horn, Probing the reaction kinetics of the charge reactions of nonaqueous Li-O_2 batteries, The Journal of Physical Chemistry Letters 4 (2013) 93–99.

[118] A. C. Luntz, V. Viswanathan, J. Voss, J. B. Varley, J. K. Nørskov, R. Scheffler, A. Speidel, Tunneling and polaron charge transport through Li_2O_2 in Li-O_2 batteries, The Journal of Physical Chemistry Letters 4 (2013) 3494–3499.

[119] J. B. Varley, V. Viswanathan, J. K. Norskov, A. C. Luntz, Lithium and oxygen vacancies and their role in Li_2O_2 charge transport in Li-O_2 batteries, Energy Environental Science 7 (2014) 720–727.

[120] V. Viswanathan, K. S. Thygesen, J. S. Hummelshøj, J. K. Nørskov, G. Girishkumar, B. D. McCloskey, A. C. Luntz, Electrical conductivity in Li_2O_2 and its role in determining capacity limitations in non-aqueous Li-O_2 batteries, The Journal of Chemical Physics 135 (2011) 214704–214710.

[121] V. Viswanathan, J. K. Nørskov, A. Speidel, R. Scheffler, S. Gowda, A. C. Luntz, Li–O_2 kinetic overpotentials: Tafel plots from experiment and first-principles theory, The Journal of Physical Chemistry Letters 4 (2013) 556–560.

[122] Y. Wang, H. Zhou, A lithium-air fuel cell using copper to catalyze oxygen-reduction based on copper-corrosion mechanism, Chemical Communication 46 (2010) 6305–6307.

[123] K.-H. Xue, G. L. Plett, A convective transport theory for high rate discharge in lithium ion cells, Electrochimica Acta 87 (2013) 575 – 590.

[124] K. Yoo, S. Banerjee, P. Dutta, Modeling of volume change phenomena in a Li–air battery, Journal of Power Sources 258 (2014) 340 – 350.

[125] C. O. Laoire, S. Mukerjee, K. M. Abraham, E. J. Plichta, M. A. Hendrickson, Influence of nonaqueous solvents on the electrochemistry of oxygen in the rechargeable lithium-air battery, The Journal of Physical Chemistry C 114 (2010) 9178–9186.

[126] J. Read, Characterization of the lithium/oxygen organic electrolyte battery, Journal of The Electrochemical Society 149 (2002) A1190–A1195.

[127] J. Read, K. Mutolo, M. Ervin, W. Behl, J. Wolfenstine, A. Driedger, D. Foster, Oxygen transport properties of organic electrolytes and performance of lithium/oxygen battery, Journal of The Electrochemical Society 150 (2003) A1351–A1356.

[128] T. Ogasawara, A. Débart, M. Holzapfel, P. Novák, P. G. Bruce, Rechargeable Li_2O_2 electrode for lithium batteries, Journal of the American Chemical Society 128 (2006) 1390–1393.

[129] S. D. Beattie, D. M. Manolescu, S. L. Blair, High-capacity lithium-air cathodes, Journal of The Electrochemical Society 156 (2009) A44–A47.

[130] C. O. Laoire, S. Mukerjee, K. M. Abraham, E. J. Plichta, M. A. Hendrickson, Elucidating the mechanism of oxygen reduction for lithium-air battery applications, The Journal of Physical Chemistry C 113 (2009) 20127–20134.

[131] X.-h. Yang, P. He, Y.-y. Xia, Preparation of mesocellular carbon foam and its application for lithium/oxygen battery, Electrochemistry Communications 11 (2009) 1127 – 1130.

[132] J. S. Hummelshøj, J. Blomqvist, S. Datta, T. Vegge, J. Rossmeisl, K. S. Thygesen, A. C. Luntz, K. W. Jacobsen, J. K. Nørskov, Communications: Elementary oxygen electrode reactions in the aprotic Li-air battery, The Journal of Chemical Physics 132 (2010).

[133] S. A. Freunberger, Y. Chen, Z. Peng, J. M. Griffin, L. J. Hardwick, F. Bardé, P. Novák, P. G. Bruce, Reactions in the rechargeable lithium-O_2 battery with alkyl carbonate electrolytes, Journal of the American Chemical Society 133 (2011) 8040–8047.

[134] Y. Chen, S. A. Freunberger, Z. Peng, F. Bardé, P. G. Bruce, Li-O_2 battery with a dimethylformamide electrolyte, Journal of the American Chemical Society 134 (2012) 7952–7957.

[135] B. D. McCloskey, R. Scheffler, A. Speidel, G. Girishkumar, A. C. Luntz, On the mechanism of nonaqueous Li–O_2 electrochemistry on C and its kinetic overpotentials: Some implications for Li–air batteries, The Journal of Physical Chemistry C 116 (2012) 23897–23905.

[136] Z. Peng, S. A. Freunberger, Y. Chen, P. G. Bruce, A reversible and higher-rate Li-O_2 battery, Science 337 (2012) 563–566.

[137] T. Zhang, H. Zhou, A reversible long-life lithium-air battery in ambient air, Nature Communications 4 (2013) 1817.

[138] D. S. Kim, Y. J. Park, Effect of multi-catalysts on rechargeable Li-air batteries, Journal of Alloys and Compounds 591 (2014) 164 – 169.

[139] M. Armand, J.-M. Tarascon, Building better batteries, Nature 451 (2008) 652–657.

[140] P. G. Bruce, Energy storage beyond the horizon: Rechargeable lithium batteries, Solid State Ionics 179 (2008) 752 – 760.

[141] J. M. Tarascon, Key challenges in future Li-battery research, Philosophical Transactions of the Royal Society A: Mathematical, Physical and Engineering Sciences 368 (2010) 3227–3241.

[142] A. Kraytsberg, Y. Ein-Eli, Review on Li-air batteries–opportunities, limitations and perspective, Journal of Power Sources 196 (2011) 886 – 893.

[143] I. Kowalczk, J. Read, M. Salomon, Li-air batteries: A classic example of limitations owing to solubilities, Pure and Applied Chemistry 79 (2007) 851–860.

[144] Y.-C. Lu, B. M. Gallant, D. G. Kwabi, J. R. Harding, R. R. Mitchell, M. S. Whittingham, Y. Shao-Horn, Lithium-oxygen batteries: Bridging mechanistic understanding and battery performance, Energy & Environmental Science 6 (2013) 750–768.

[145] B. D. McCloskey, D. S. Bethune, R. M. Shelby, G. Girishkumar, A. C. Luntz, Solvents' critical role in nonaqueous lithium-oxygen battery electrochemistry, The Journal of Physical Chemistry Letters 2 (2011) 1161–1166.

[146] M. M. O. Thotiyl, S. A. Freunberger, Z. Peng, P. G. Bruce, The carbon electrode in nonaqueous Li–O_2 cells, Journal of the American Chemical Society 135 (2013) 494–500.

[147] M. M. O. Thotiyl, S. A. Freunberger, Z. Q. Peng, Y. H. Chen, Z. Liu, P. G. Bruce, A stable cathode for the aprotic Li-O_2 battery, Nature Materials 12 (2013) 1049–1055.

[148] H. Wang, K. Xie, L. Wang, Y. Han, All carbon nanotubes and freestanding air electrodes for rechargeable Li–air batteries, RSC Advances 3 (2013) 8236–8241.

[149] J. Xiao, W. Xu, D. Wang, J.-G. Zhang, Hybrid air-electrode for Li/air batteries, Journal of The Electrochemical Society 157 (2010) A294–A297.

[150] G. Q. Zhang, J. P. Zheng, R. Liang, C. Zhang, B. Wang, M. Hendrickson, E. J. Plichta, Lithium–air batteries using SWNT/CNF buckypapers as air electrodes, Journal of The Electrochemical Society 157 (2010) A953–A956.

[151] J. M. Garcia-Lastra, J. D. Bass, K. S. Thygesen, Communication: Strong excitonic and vibronic effects determine the optical properties of Li_2O_2, The Journal of Chemical Physics 135 (2011) 121101–121104.

[152] N. Imanishi, A. C. Luntz, P. G. Bruce, The Lithium Air Battery: Fundamentals, Springer, 2014.

[153] C. Ó. Laoire, S. Mukerjee, E. J. Plichta, M. A. Hendrickson, K. M. Abraham, Rechargeable lithium/TEGDME-$LiPF_6O_2$ battery, Journal of The Electrochemical Society 158 (2011) A302–A308.

[154] P. Albertus, G. Girishkumar, B. McCloskey, R. S. Sánchez-Carrera, B. Kozinsky, J. Christensen, A. C. Luntz, Identifying capacity limitations in the Li/oxygen battery using experiments and modeling, Journal of The Electrochemical Society 158 (2011) A343–A351.

[155] J. Read, Ether-based electrolytes for the lithium/oxygen organic electrolyte battery, Journal of The Electrochemical Society 153 (2006) A96–A100.

[156] S. S. Zhang, D. Foster, J. Read, Discharge characteristic of a non-aqueous electrolyte Li/O_2 battery, Journal of Power Sources 195 (2010) 1235–1240.

[157] S. S. Zhang, K. Xu, J. Read, A non-aqueous electrolyte for the operation of Li/air battery in ambient environment, Journal of Power Sources 196 (2011) 3906–3910.

[158] J. P. Neidhardt, D. N. Fronczek, T. Jahnke, T. Danner, B. Horstmann, W. G. Bessler, A flexible framework for modeling multiple solid, liquid and gaseous phases in batteries and fuel cells, Journal of The Electrochemical Society 159 (2012) A1528–A1542.

[159] L. D. Griffith, C. W. Monroe, Correlating Li/O_2 cell capacity and product morphology with correlating Li/O_2 cell capacity and product morphology with discharge current, to be submitted (2015).

[160] L. Li, X. Zhao, A. Manthiram, A dual-electrolyte rechargeable Li-air battery with phosphate buffer catholyte, Electrochemistry Communications 14 (2012) 78–81.

[161] Y.-C. Lu, H. A. Gasteiger, E. Crumlin, R. McGuire, Y. Shao-Horn, Electrocatalytic activity studies of select metal surfaces and implications in Li-air batteries, Journal of The Electrochemical Society 157 (2010) A1016–A1025.

[162] A. K. Thapa, K. Saimen, T. Ishihara, Pd/MnO_2 air electrode catalyst for rechargeable lithium/air battery, Electrochemical and Solid-State Letters 13 (2010) A165–A167.

[163] J.-G. Zhang, D. Wang, W. Xu, J. Xiao, R. Williford, Ambient operation of Li/air batteries, Journal of Power Sources 195 (2010) 4332–4337.

[164] X. Zhang, L. Hua, E. Yang, Z. An, J. Chen, X. Chen, X. Chao, J. Yu, M. Wu, X. Miao, A simple method of making a Li-air battery with longevity, International Journal of electrochemical Science 7 (2012) 10562–10569.

[165] S. Dong, X. Chen, S. Wang, L. Gu, L. Zhang, X. Wang, X. Zhou, Z. Liu, P. Han, Y. Duan, H. Xu, J. Yao, C. Zhang, K. Zhang, G. Cui, L. Chen, 1D coaxial platinum/titanium nitride nanotube arrays with enhanced electrocatalytic activity for the oxygen reduction reaction: Towards Li-air batteries, ChemSusChem 5 (2012) 1712–1715.

[166] T. T. Truong, Y. Liu, Y. Ren, L. Trahey, Y. Sun, Morphological and crystalline evolution of nanostructured MnO_2 and its application in lithium–air batteries, ACS Nano 6 (2012) 8067–8077.

[167] D. Wang, J. Xiao, W. Xu, J.-G. Zhang, High capacity pouch-type Li–air batteries, Journal of The Electrochemical Society 157 (2010) A760–A764.

[168] D. A. G. Bruggeman, Berechnung verschiedener physikalischer konstanten von heterogenen substanzen. I. dielektrizitätskonstanten und leitfähigkeiten der mischkörper aus isotropen substanzen, Annalen der Physik 416 (1935) 636–664.

[169] J. Lu, K. Amine, Recent research progress on non-aqueous lithium-air batteries from argonne national laboratory, Energies (2013) 6016–6044.

[170] D. Brouillette, G. Perron, J. E. Desnoyers, Apparent molar volume, heat capacity, and conductance of lithium bis(trifluoromethylsulfone)imide in glymes and other aprotic solvents, Journal of Solution Chemistry 27 (1998) 151–182.

[171] N. Deprez, D. S. McLachlan, The analysis of the electrical conductivity of graphite conductivity of graphite powders during compaction, Journal of Physics D: Applied PhysicsEmail alert RSS feed 21 (1988) 101–107.

[172] P. Andrei, J. P. Zheng, M. Hendrickson, E. J. Plichta, Modeling of Li-air batteries with dual electrolyte, Journal of The Electrochemical Society 159 (2012) A770–A780.

[173] C. Jung, T. Zhao, L. An, Modeling of lithium-oxygen batteries with the discharge product treated as a discontinuous deposit layer, Journal of Power Sources (2014).

[174] U. Sahapatsombut, H. Cheng, K. Scott, Modelling the micro–macro homogeneous cycling behaviour of a lithium–air battery, Journal of Power Sources 227 (2013) 243–253.

[175] M. D. Radin, D. J. Siegel, Charge transport in lithium peroxide: Relevance for rechargeable metal-air batteries, Energy Environental Science 6 (2013) 2370–2379.

[176] B. D. Adams, C. Radtke, R. Black, M. L. Trudeau, K. Zaghib, L. F. Nazar, Current density dependence of peroxide formation in the Li-O_2 battery and its effect on charge, Energy & Environmental Science 6 (2013) 1772–1778.

[177] X.-h. Yang, Y.-y. Xia, The effect of oxygen pressures on the electrochemical profile of lithium/oxygen battery, Journal of Solid State Electrochemistry 14 (2010) 109–114.

[178] C.-X. Zu, H. Li, Thermodynamic analysis on energy densities of batteries, Energy & Environmental Science 4 (2011) 2614–2624.

[179] C. Daniel, J. O. Besenhard, Handbook of Battery Materials, 2nd ed., Wiley-VCH, 2011.

[180] B. D. McCloskey, J. M. Garcia, A. C. Luntz, Chemical and electrochemical differences in nonaqueous Li–O_2 and Na–O_2 batteries, The Journal of Physical Chemistry Letters 5 (2014) 1230–1235.

[181] J. Liu, C. W. Monroe, Capacity-limiting mechanisms in Li/O_2 positive electrodes, Energy & Environmental Science (to be submitted).

[182] B. D. McCloskey, R. Scheffler, A. Speidel, D. S. Bethune, R. M. Shelby, A. C. Luntz, On the efficacy of electrocatalysis in nonaqueous Li-O_2 batteries, Journal of the American Chemical Society 133 (2011) 18038–18041.

[183] A. K. Thapa, T. Ishihara, Mesoporous -MnO_2/Pd catalyst air electrode for rechargeable lithium–air battery, Journal of Power Sources 196 (2011) 7016–7020.

[184] Q. Sun, Y. Yang, Z.-W. Fu, Electrochemical properties of room temperature sodium–air batteries with non-aqueous electrolyte, Electrochemistry Communications 16 (2012) 22–25.

[185] E. Peled, D. Golodnitsky, H. Mazor, M. Goor, S. Avshalomov, Parameter analysis of a practical lithium- and sodium-air electric vehicle battery, Journal of Power Sources 196 (2011) 6835–6840.

[186] P. Hartmann, C. L. Bender, J. Sann, A. K. Durr, M. Jansen, J. Janek, P. Adelhelm, A comprehensive study on the cell chemistry of the sodium superoxide (NaO_2) battery, Physical Chemistry Chemical Physics 15 (2013) 11661.

[187] P. Hartmann, D. Grübl, H. Sommer, J. Janek, W. G. Bessler, P. Adelhelm, Pressure dynamics in metal–oxygen (metal–air) batteries: A case study on sodium superoxide cells, The Journal of Physical Chemistry C 118 (2014) 1461–1471.

[188] S. Kang, Y. Mo, S. P. Ong, G. Ceder, Nanoscale stabilization of sodium oxides: Implications for Na–O_2 batteries, Nano Letters 14 (2014) 1016–1020.